Graduate Theses & Non-Theses                                    Student Scholarship

Spring 2017

# ADSORPTION OF SALICYLHYDROXAMIC ACID ON SELECTED RARE EARTH OXIDES AND CARBONATES

Greer Galt
*Montana Tech*

Follow this and additional works at: http://digitalcommons.mtech.edu/grad_rsch

 Part of the Metallurgy Commons, and the Other Engineering Science and Materials Commons

## Recommended Citation

# ADSORPTION OF SALICYLHYDROXAMIC ACID ON SELECTED RARE EARTH OXIDES AND CARBONATES

by

Greer Elaine Galt

A thesis submitted in partial fulfillment of the
requirements for the degree of

Master of Science in Metallurgical/Mineral Processing Engineering

Montana Tech of The University of Montana

2017

## Abstract

Adsorption behavior of the anionic collector salicylhydroxamic acid (SHA) on a selected group of rare earth oxides (REOs) and carbonates (RECs) was studied via experimental methods and modelling software. Synthetic oxide and carbonate powders of the rare earth elements cerium (Ce), praseodymium (Pr), europium (Eu), and terbium (Tb) were tested for this research. Studies were conducted at different pH levels to analyze the kinetics of collector adsorption onto the oxide and carbonate surfaces in attempts to optimize recovery parameters for commercial flotation processes using SHA. In addition, thermodynamic software StabCal was implemented to compare theoretical adsorption behavior of collectors SHA and octylhydroxamic acid (OHA) on these four rare earth oxides and carbonates. Theoretical points of zero charge were also estimated via StabCal and compared to experimental values to establish validity. Results for oxides indicate that both the amount and rate of SHA adsorption are highest for lighter REOs, decreasing as ionic diameter increases, a chelation phenomenon common with hydroxamates. However, results for the carbonates exhibit the opposite trend: strongest SHA adsorption was seen in the heavy RECs. This pattern correlates to the increasing stability of the carbonate such that ionic diameter of the REs becomes more amenable to chelation due to differences in bonding chemistry. Overall, adsorption kinetics appear dependent on pH, coordination chemistry, and cation size.

Keywords:

Flotation, Salicylhydroxamic Acid, Rare Earth Oxides, Rare Earth Carbonates, Adsorption

## Dedication

For my mother and father, whose tremendous sacrifices and unconditional support continue to serve as great life lessons to this day; for the family and friends who have seen in me the potential that I could not see in myself; and for Grant, my ultimate source for cracking chemistry conundrums and reminder to get lost in a nerdy board game every once in a while.

## Acknowledgements

# Table of Contents

## List of Tables

## List of Figures

# List of Equations

# List of Acronyms and Important Chemical Symbols

**Ce:** Cerium

**Dy:** Dysprosium

**Eu:** Europium

**H2O5:** N-3-dihydroxy-napthalene-2-carboxamide

**HCl:** Hydrochloric acid

**HREE(s):** Heavy rare earth element(s)

**IEP(s):** Isoelectric point(s)

**LREE(s):** Light rare earth element(s)

**La:** Lanthanum

**MW:** Molecular weight

**NaOH:** Sodium hydroxide

**Nd:** Neodymium

**OHA:** Octylhydroxamic Acid

**Pr:** Praseodymium

**PZC(s):** Point(s) of zero charge

**REE(s):** Rare earth element(s)

**REO(s):** Rare earth oxide(s)

**REC(s):** Rare earth carbonate(s)

**REM(s):** Rare earth minerals(s)

**SHA:** Salicylhydroxamic acid

**Tb:** Terbium

**Y:** Yttrium

# 1. Introduction

Rare earth elements (REEs) have recently garnered much attention and demand due to their unique geochemical properties which make them particularly useful in the applications of magnetics and electronics. REEs are classified into light and heavy categories according to their atomic weights. Despite their name, REEs are relatively abundant in the earth's crust, with cerium (Ce) ranking as the 25th most abundant element at 68 parts per million, about as much as copper (Cu). The term "rare" originates from the similar chemical properties REEs share, making them difficult to separate from one another. In addition, REEs are typically not found to be highly concentrated in most ore deposits, and therefore extraction and processing to achieve high REE recovery is more complex. Thus, the complications of rare earth metal extraction limit their major ore sources containing rare earth minerals (REMs) such as bastnaesite $((Ce,La)CO_3F)$, monazite $((Ce,La,Nd,Th)PO_4)$, and xenotime $((Y,Dy,Yb,Er,Gd)PO_4)$.

Rare earth deposits are most commonly extracted from ore bodies using froth flotation, a hydrometallurgical method that involves surface chemistry alteration of a desired mineral in order to extract it from unwanted material. This separation is performed in a flotation cell where a designated amount of ore is processed as a slurry and allowed to mix with reagents which are designed to make particles either hydrophobic (water-repellent) or hydrophilic (water loving). Air bubbles are dispersed through the slurry and eventually float to the surface to form an airy froth. Hydrophobic particles will collide with and attach to the air bubbles as they rise, leaving behind the hydrophilic material. The froth containing hydrophobic particles is typically labeled as the product concentrate, or con, and the remaining slurry represents the tailings, or gangue.

Flotation recovery depends heavily on a series of solution chemistry factors, which have been studied for over one hundred years in order to analyze and improve their effects on flotation

success rates. These factors include solution pH, ionic strength, frother concentration and type, and collector type and concentration. Collectors induce hydrophobicity for the minerals of interest by adsorbing to the mineral particles and adhering either physically or chemically as determined by surface chemistry. Further research is currently being conducted at Montana Tech on a select group of novel collectors, studying their surface chemistry and interaction with REEs in order to establish optimal flotation parameters for rare earth recovery.

The objective of this study was to analyze the kinetics and extent of adsorption of the novel collector salicylhydroxamic acid (SHA), or salicyl, on the surfaces of four REEs in their oxide and carbonate forms at various pH conditions. Results for oxides and carbonates were compared to one another to identify any trends, discrepancies, or similarities in behavior. Speciation diagrams were also constructed using thermodynamic software to aid in the comparisons. These diagrams essentially indicated the ideal pH range over which an oxide or carbonate of interest would float using SHA. In addition, the solubility plots incorporated crucial thermodynamic data such as the Gibbs' free energy of the collector which is highly useful in identifying the adsorption mechanism as chemisorption, physisorption, or surface precipitation. Speciation plots for SHA were compared with plots for the collector octylhydroxamic acid (OHA) to assess theoretical recovery. The diagrams for SHA also yielded theoretical points of zero charge for the surfaces of the studied oxides and carbonates that were compared to experimentally obtained points of zero charge using a Stabino instrument. Research for this investigation focused on the degree of collector adsorption on the surface of each rare-earth oxide and carbonate at alkaline pH levels.

## 2. Literature Review

### 2.1. Rare Earth Elements (REEs)

#### 2.1.1. Background

Rare earth elements (REEs) consist of the 15 lanthanides as well as scandium (Sc) and

yttrium (Y), and can be classified as light or heavy rare earths (LREEs and HREEs), according to

Gupta and Krishnamurthy (2005). The LREEs are comprised of lanthanum (La), cerium (Ce),

praseodymium (Pr), neodymium (Nd), promethium (Pm), samarium (Sm), and europium (Eu).

The remaining rare earths are considered HREEs and include gadolinium (Gd), terbium (Tb),

dysprosium (Dy), holmium (Ho), erbium (Er), thulium (Tm), ytterbium (Yb), and lutetium (Lu).

Yttrium is also considered a "heavy" since it behaves similarly to the heavy lanthanides. Figure 1

maps the abundance of REEs, precious metals, and other major industrial metals in the Earth's

crust as a function of atomic number (Haxel, Hedrick, & Orris, 2005).
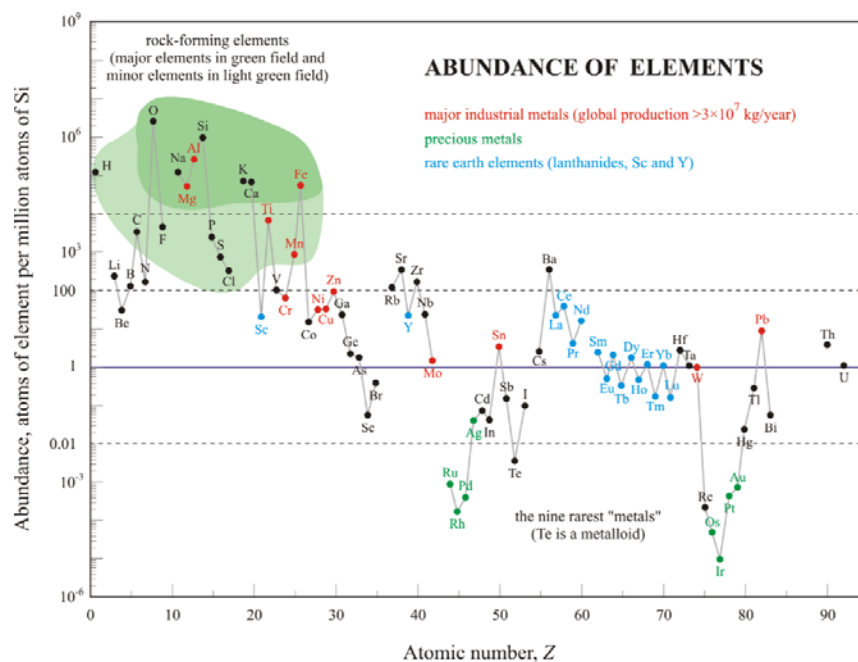


**Figure 1: Abundance of Elements in Earth's Upper Crust (REEs highlighted in blue)**

LREEs are typically more abundant in the Earth's crust, as conveyed in Figure 1, although none of the REEs are truly rare. The term "rare" is a slight misnomer and refers to the fact that rare-earths are scarcely found in concentrated, exploitable deposits, and also to the unique properties that they share which make them difficult to separate from one another and have tremendously increased demand for their industrial applications (Alonso, et al., 2012). Table I was taken from Binnemans, et al. (2013) and contains data on the relative percentages of REEs in such applications as magnetics, cell phones, rechargeable batteries, lasers, phosphor coatings and medical imaging.

**Table I: REE Percentages by Application**

| Application | La | Ce | Pr | Nd | Sm | Eu | Gd | Tb | Dy | Y | Other |
|---|---|---|---|---|---|---|---|---|---|---|---|
| Magnets | | | 23.4 | 69.4 | | | 2 | 0.2 | 5 | | |
| Battery alloys | 50 | 33.4 | 3.3 | 10 | 3.3 | | | | | | |
| Metallurgy | 26 | 52 | 5.5 | 16.5 | | | | | | | |
| Auto catalysts | 5 | 90 | 2 | 3 | | | | | | | |
| FCC | 90 | 10 | | | | | | | | | |
| Polishing powders | 31.5 | 65 | 3.5 | | | | | | | | |
| Glass additives | 24 | 66 | 1 | 3 | | | | | 2 | | 4 |
| Phosphors | 8.5 | 11 | | | | 4.9 | 1.8 | 4.6 | | 69.2 | |
| Ceramics | 17 | 12 | 6 | 12 | | | | | | 53 | |
| Others | 19 | 39 | 4 | 15 | 2 | | 1 | | | 19 | |

Similar chemical and physical properties among the REEs increase their complexity and the complications of separating REEs from one another. Most REEs readily form the +3 ion in aqueous systems, although Ce, Eu, Tb, and Yb also occur in a +2 or +4 state which may be attributed to the ionization potentials and electronic structures of these lanthanides (Anderson, 2015). In their trivalent states, the lanthanides all share similar electronegativity values (1.12-1.22) and similar atomic weights (139-175 g/mol). In addition, the REEs all react with nitrogen, hydrogen, and carbon, forming mononitrides, hydrides, and dicarbides respectively. REEs also have affinities for sulfur, selenium, and phosphorus and result in exothermic reactions at high temperatures (Gupta & Krishnamurthy, 2005).

Perhaps one of the most significant properties of the REEs is a phenomenon known as the "lanthanide contraction" (Figure 2). Ionic radii typically increase with atomic number from left to right across the periodic table as the elements gain more electrons. Conversely, REEs decrease in size and increase in atomic weight as a result of insufficient shielding of the atomic nucleus due to the directional shape of REE $4f$ orbitals. Thus, additional electrons are drawn towards the nucleus as nuclear charge increases causing the entire $4f$ shell to contract and atomic size to decrease (Gupta & Krishnamurthy, 2005). Without this phenomenon, separating REEs from one another would become extremely complicated.
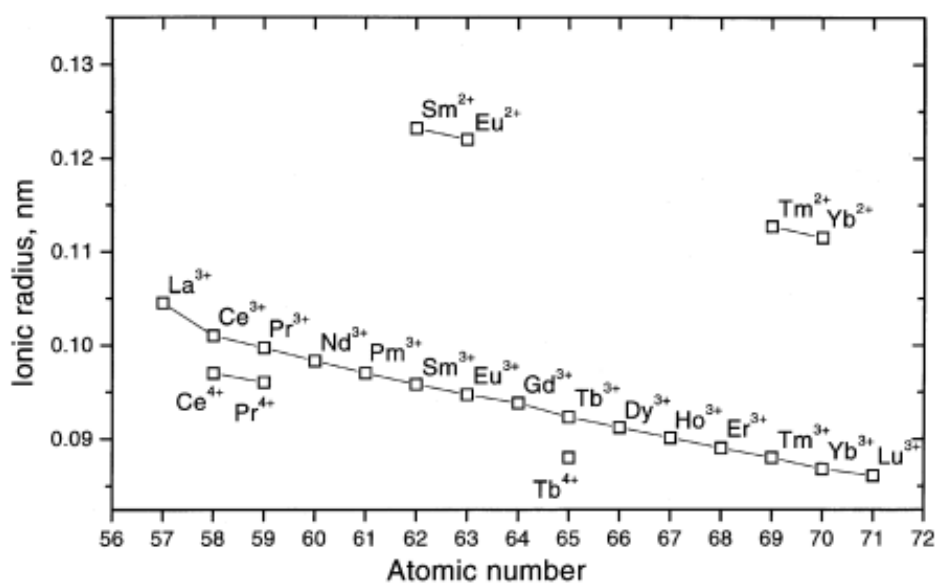


**Figure 2: Lanthanide Contraction (Gupta & Krishnamurthy, 2005)**

The lanthanide contraction contributes to many of the chemical properties related to REEs. For example, basicity measures the affinity of a species for an electron and anion, and determines salt solubility as well as the stability of complex ions. Cations with the lower attraction for electrons are considered basic, e.g. $La^{3+}$ and those with higher affinities are considered less basic, e.g. $Lu^{3+}$ (Anderson, 2015). Similarly, ionization potential should decrease

with increasing atomic number but remains fairly constant due to the lanthanide contraction. Likewise, metallic density predominantly increases with atomic number (Thiel, 2003; Jensen & Mackintosh, 1991).

Not all properties, however, follow this trend including but not limited to electrical resistivity and magnetic susceptibility. Such properties tend to exhibit highest values in the middle of the lanthanide series, typically Gd and Tb, and lowest on the ends with La and Lu (Güntherodt, Hauser, & Künzi, 1974; Liu, 1960). This phenomenon is related to how the eight $4f$ and one $5d$ orbitals fill such that maximum values are not reached until electron pairing occurs. In this regard, it is easy to understand why both Gd and Dy are used in making non-ferrous magnets as well as for medical magnetic resonance imaging (MRI) as contrast agents (Caravan, Ellison, McMurry, & Lauffer, 1999; Ericsson, Bach-Gansmo, Niklasson, & Hemmingsson, 1995).

Ores with rare earth metals present usually contain minerals with multiple REEs. The minerals bastnaesite, monazite, and xenotime are considered the primary sources of rare earth metals (Pavez, Brandao, & Peres, 1996). Bastnaesite is a REE-fluorocarbonate and monazite is a phosphate, both of which contain mostly lighter rare earths, while HREEs are more commonly associated with xenotime, an yttrium phosphate mineral. Rare earth oxides comprise roughly 70% of rare earth material in monazite, predominantly $Ce_2O_3$ and $La_2O_3$, as well as Nd, Pr, and Sm (Kim et al., 2012).

### 2.1.2. REE Significance

Currently, REE production is supplied almost exclusively by China due primarily to lower environmental standards and labor costs (Grasso, 2013). As of 2013, China continues to produce more than 90% of all REEs, presenting a challenge for increasing world demand.

Indeed, the European Commission has labeled REEs as the most critical raw materials group with the highest supply risk, since the world has grown increasingly dependent on China for its REE supply (Binnemans, et al., 2013). REEs are critical components in modern products and alternative fuel sources which have increased in popularity. According to a study by Alonso et al. (2012), magnets could grow to represent 50% of the rare-earth market, and consequently, demand for neodymium and dysprosium in particular is expected to increase over the next 25 years by 700% and 2600%, respectively.

In order to relieve the heavy dependence on China for REE imports, U.S. companies are investigating potential REE domestic reserves including, but not limited to, the Bear Lodge deposit that is currently under development by Rare Earth Resources Ltd in northeast Wyoming, the Diamond Hill and Lemhi Pass properties maintained by U.S. Rare Earths in central Idaho, and the Mountain Pass deposit owned by Molycorp in southern California (Long, Van Gosen, Foley, & Cordier, 2010). Molycorp had resumed operations at the Mountain Pass mine in late 2012 but filed for bankruptcy in 2015 and suspended rare earth production; however, the mine is currently being marketed for sale (Jamasmie, 2015).

In addition to examining alternative primary sources for REE extraction, recyling technologies for processing secondary resoures such as REE magnets, batteries, and phosphors are also under development (Binnemans, et al., 2013). Other investigations suggest REE production may be achieved through vapor phase extraction, ion exchange with resins and polyamine composites, leaching and solution recovery through solvent extraction (Habashi, 2005), and flotation with novel collectors, which is the focus of this research.

## 2.2. Flotation

### 2.2.1. Overview

Flotation is a physico-chemical, mineral processing technique designed to extract

valuable commodities from their ores and separate them from unwanted material by utilizing the

differences in surface chemical properties. In flotation, ore is processed as a slurry normally in

an agitated cell where generated air bubbles attach to hydrophobic minerals and rise to the pulp

surface to create a froth phase. To be effective, numerous parameters must be controlled,

depending on the desired material being floated and its differences in properties compared to the

gangue material. The critical aspect of flotation is establishing the selective hydrophobicity of

the valuable mineral, i.e. its tendency to repel water. With the exception of a few minerals such

as graphite, talc and sulfur, most are naturally hydrophilic, and reagents must be subsequently

administered to enhance or induce hydrophobicity of only the desired mineral surfaces. These

particles will then attach to the generated air bubbles and be collected as concentrate, while the

gangue material that remains in the slurry is discarded as tailings. Successful recovery by

flotation depends largely on particle attachment to air bubbles and entrainment in the water in the

froth phase of the circuit (Wills, 2006). An illustration of the fundamentals of froth flotation is

provided in Figure 3.
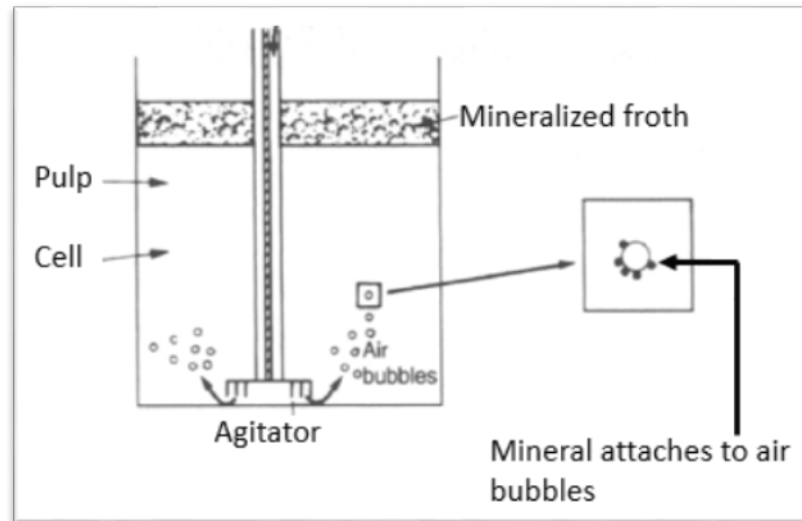
**Figure 3: General Froth Flotation Setup (Wills, 2006)**

## 2.2.2. Influential Factors

### 2.2.2.1. Solution pH

The pH of a solution measures the hydrogen ion ($H^+$) activity which can influence the surface charge of a mineral. Nearly all minerals exhibit a charge and consequently possess a point of zero charge (PZC), or isoelectric point (IEP), the pH at which the mineral surface accumulates no charge. In general, at low pH below this point the surface charge is positive due to excess $H^+$ and at high pH above this point, it is negative due to excess $OH^-$. Figure 4 depicts points of zero charge for the oxides of cerium, samarium, and erbium as measured with an ultrasonic vibration potential (UVP) technique (Hattori & Masakuni, 2004). PZCs were estimated from the graph to be 6.7, 8.3, and 8.8 for cerium, samarium, and erbium, respectively.
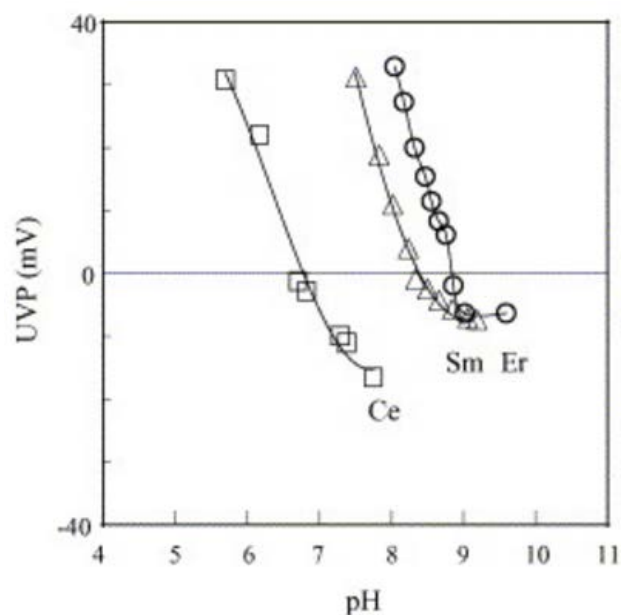
**Figure 4: PZC Plots for Oxides of Cerium, Samarium, and Erbium**

Assuming adsorption and surface chemistry aspects are due solely to physical attraction, knowing the PZC of a given mineral is critical in order to establish a solution pH and produce a surface charge that is opposite that of the collector. Opposing charges help to maximize collector adsorption to the mineral surface and cause it to become hydrophobic and float. The PZC can be estimated by the zeta potential which is the potential at the shear plane of particles in motion in a stationary solution. A stagnant and diffuse layer of solution exists between the mineral surface and shear plane, whereas uniform concentrations (i.e. bulk water) exist outside of it. The PZC can also be estimated using streaming potential which is designed to measure the excitation of particles via a streaming fluid that moves through a packed bed of particles such that it induces a differential velocity between an anionic interface and liquid medium (Stabino®., 2013). Both methods yield measurements that are then used to calculate zeta potential.

### 2.2.2.2. Flotation Reagents

Various reagents may be added to a slurry to promote the selectivity of the flotation process, including collectors, frothers, depressants, activators, and modifiers. Collectors are heteropolar surfactants that adsorb at valuable mineral surfaces to render them hydrophobic. This reagent is later discussed in more detail. Frothers are designed to stimulate as well as stabilize bubble activity at the surface of the cell to enhance the selectivity of the overall process. Depressants are typically used to prevent collector adsorption at gangue mineral surfaces so that they remain hydrophilic and therefore do not float. In contrast, activators are used to change a mineral surface to enhance collector adsorption and thereby render it hydrophobic. By comparison, modifiers can act as both a depressant for gangue material and an activator for valuable minerals. In general, modifiers are used to control the solution pH and thus surface charge.

As previously stated, collectors are added to induce hydrophobicity at given mineral surfaces through their adsorption. Collectors are heteropolar molecules consisting of an inorganic and reactive polar head group and an inert, organic, nonpolar tail group. The polar head may be positively or negatively charged, allowing it to be selectively attracted to a surface of opposite charge. Upon adsorption, its reactivity will determine whether a physical or chemical bond forms. As shown in Figure 5, the organic tail, which exhibits hydrophobic properties and may be either short-chained or long-chained, protrudes from the surface into the solution, and subsequently induces its hydrophobicity (Wills, 2006).
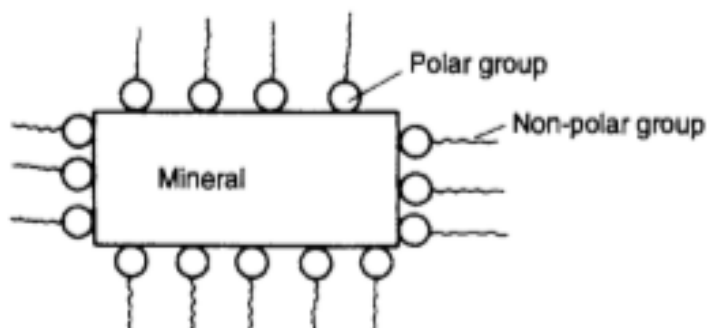
**Figure 5: Collector Adsorption (Wills, 2006)**

Selectivity of the overall flotation process is influenced by collector chemistry, mineral surface chemistry, and solution chemistry. Collectors were the only flotation reagents used in this study to examine its fundamental interactions with rare earth oxides and carbonates.

### 2.2.3. Collector Adsorption

Collectors may adsorb onto a mineral surface by means of four different mechanisms: physisorption, chemisorption, surface precipitation, and colloid adsorption. Physisorption consists of a weak interaction between the adsorbate and the adsorbent surface, generated by coulombic and van der Waals forces with the surface structure remaining intact and unperturbed. In this regard, physisorption predominates when the collector is oppositely charged from the mineral surface. By comparison, chemisorption occurs when a chemical bond forms between the adsorbed collector and the surface. The chemical bond may be covalent or ionic but typically alters the structure of the adsorbent surface. This mechanism is highly desired as it denotes irreversibility, resulting in higher flotation recoveries. Both physisorption and chemisorption can result from ion exchange at the surface but neither can exceed monolayer coverage. Surface precipitation occurs when a mineral possesses some degree of solubility, causing the collector to precipitate at the surface with metal species that are dissolving at the surface. Despite the

formation of a new chemical bond, multilayer adsorption is also a development via surface precipitation. Finally, collector interaction can occur via colloid adsorption. In this case, solutions tend to be a brine due to high solubility of the mineral, forcing the collector to form a colloid in order to dissolve. Upon adsorption, the colloid resembles a micelle which is also generally considered multilayer adsorption.

### 2.2.4. Adsorption Thermodynamics

The Gibbs free energy equation is often implemented to characterize the occurrence of monolayer adsorption. Gibbs free energies between 0 and -5 kcal/mol are indicative of physisorption behavior. Physisorption reactions tend to be exothermic and are therefore enthalpically driven, whereas negative free energies of at least -10 kcal/mol are reflective of chemisorption reactions but usually entropically driven. In this case, chemisorption can be considered collector ordering at the surface, but entropy must be governed by the displacement of water in order to be sufficiently positive. Thus, as surface water desorbs, it transitions from a structured state at a hydrophilic surface to form bulk water away from the now hydrophobic mineral surface.

In order to evaluate these adsorption thermodynamics, such monolayer adsorption is typically modeled with either the Langmuir Isotherm or common variations including Freundlich, Frumpkin, and Tempkin Isotherms. These isotherm models are constructed with controls on parameters such as temperature, pressure, and/or concentration. Although normally established at equilibrium, the models can also be monitored with time to examine adsorption kinetics. However, it should be noted that each model was developed based on certain assumptions that can limit their applications. For example, Langmuir behavior assumes constant

free energy for every adsorption site and that neighboring adsorbed molecules do not interact.

Likewise, Freundlich isotherms are based on low surface coverage.

### 2.2.5. Rare Earth Mineral (REM) Flotation

Research on suitable collectors for rare earth flotation has established hydroxamates as

the most common collectors used for rare-earth extraction. In particular, octyl hydroxamate is

shown to be more effective than oleate, a fatty acid (FA) collector (Pradip & Fuerstenau, 1983,

1991). These investigations have determined how the two collectors adsorb at various mineral

surfaces and that this understanding was essentially employed in optimizing recovery. Specific

studies commonly focused on two REMs: monazite ($(Ce,La,Nd,Th)PO_4$) and bastnaesite

($(Ce,La)CO_3F$). For example, Pavez et al. (1996) investigated the floatability of monazite and

bastnaesite samples in the presence of sodium oleate as well as potassium octyl-hydroxamate. A

90% recovery was achieved at a pH of 3 in the presence of oleate for monazite, whereas

hydroxamate yielded about 70% at pH 5. Conversely, bastnaesite recovery was slightly higher

with hydroxamate (over 90% at pH 10) than with oleate (almost 90% at pH 9).

However, with current REE ores decreasing in grade as well as liberation size, flotation

with OHA and FA collectors is becoming increasingly difficult due to low recoveries of roughly

60% or less (Pavez, Brandao, & Peres, 1996, and Pradip & Fuerstenau, 1991). Current strategies

to improve recoveries have therefore centered on developing novel collectors by changing, for

instance, the head group functionality and size, the organic tail length and type, the number of

tails, etc. which includes but is not limited to salicylhydroxamic acid (SHA), N-3-dihydroxy-

napthalene-2-carboxamide (H2O5), and an oleate/hydroxamate derivative (sarcosinate). For

example, a study by Xia, Hart, Chelgani, and Douglas (2014) examined the effects of three

hydroxamates (i.e., salicyl, benzoyl, and H2O5) on rare-earth recovery through a series of micro

flotation experiments. Dual collector systems were also implemented to compare to the single collector results. The tested ore was chiefly comprised of the oxides Ce, La, Nd, Nb, Zr, and Y. The authors reported that highest LREE recoveries were achieved with salicyl hydroxamate followed closely by H2O5, yielding recoveries of up to 60%. However, benzoyl hydroxamate was seen to favor the HREEs whereas the other collectors both performed poorly. Furthermore, all recoveries increased considerably for tests performed at elevated temperatures.

### 2.2.5.1. Salicylhydroxamic Acid (SHA)

Salicylhydroxamic acid (SHA) is an anionic collector that belongs to the group of hydroxamic acids (HAs), organic compounds that are used as a variety of drugs (Yamin, Ponce, Estrada, & Vert, 1996). SHA has a chemical formula of $C_7H_7NO_3$ and a valence of -1. The molecular structure of SHA is shown in Figure 6, created using Spartan Student STO-3G computational chemistry software. Its structure consists of a double-bonded oxygen and two open hydroxyl groups, with coordinating oxygen and nitrogen atoms bound to carbon atoms attached to a benzene ring. The hydroxamate head group is indicated by the molecular distance of 2.42 Å between the centered and rightmost oxygen atoms.
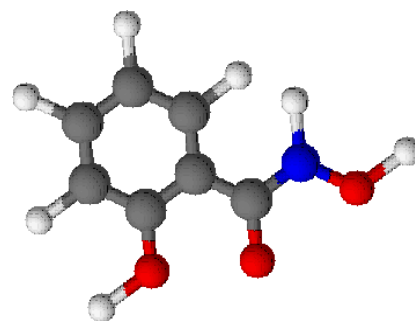


**Figure 6: Molecular Structure of SHA. Red atoms represent oxygen, blue represents nitrogen, gray atoms represent carbon, and white atoms represent hydrogen.**

Nicholas, LaDouceur, Das, and Young (2016) and Young, Downey, and Gleason (2017) experimented with elevated temperatures to assess temperature effects on adsorption kinetics; however, these studies demonstrated minimal to no improvement in SHA adsorption with increasing temperature. This lack of change in kinetics for SHA can be attributed to the cyclic configuration of its nonpolar tail. Because benzene acts as the organic tail of SHA, it does not possess a straight or branched chain organic tail as seen with most modern collectors since the bonds are locked in a cyclic chain. Consequently, SHA cannot undergo gauche-trans conformational changes that straight chains can due to rotational isomerism about the carbon-carbon bonds. Such "melting" behavior is prohibited in cyclic chains, suggesting that SHA would perform similarly at both elevated and room temperature. Furthermore, the cyclic chain behaves as a fin and cannot bend or rotate like a tail, but only oscillate. Because these unique features could potentially eliminate the usage of OHA and FA collectors at elevated temperatures and lead to substantial energy savings for flotation, SHA was selected for primary investigation in this study.

# 3. Experimental Design

Pure oxide and carbonate powders of the rare earths cerium, praseodymium, europium, and terbium were studied and analyzed in regards to the adsorption kinetics of SHA at their surfaces. SHA and powders of rare earth compounds were obtained from Alfa Aesar and consisted of purity levels 99.9% and 99% respectively. Several techniques and software programs were employed to establish the adsorption behavior occurring at each oxide and carbonate surface.

## 3.1. Equilibrium Studies

### 3.1.1. Background

Equilibrium studies were carried out at pH levels 9, 10, and 11, to measure and compare maximum adsorption of SHA on the mineral surface. The time needed to reach equilibrium can depend on factors such as surface charge of the collector, temperature, and surface area of the mineral. Equilibrium tests measured the amount of collector in solution as a function of time and yielded a final, equilibrium concentration that suggested how much adsorption or surface precipitation had occurred. Equilibrium concentrations were then used, along with the surface area calculations obtained from a Quantachrome BET analyzer, to calculate the adsorption density as a function of collector concentration in solution. Use of an ultraviolet-visible spectrophotometer (UV-Vis) was employed to measure the absorbance of collector and rare-earth in solution (Figure 7).
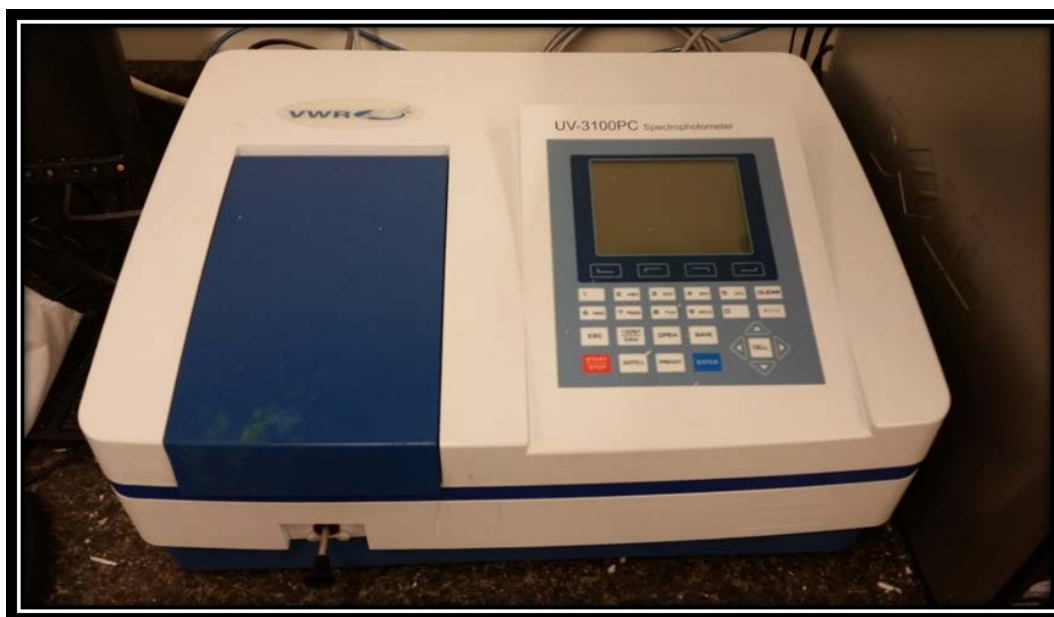
**Figure 7: VWR UV/Vis Spectrophotometer for Absorbance Measurements of SHA in REMs**

### 3.1.2. Setup

Equilibrium studies were performed at 20°C using SHA with both oxide and carbonate forms of cerium, praseodymium, europium, and terbium. Tests were carried out pH levels 9, 10, and 11 as is done in commercial flotation processes. Tests operated with a solution volume of 200 mL, 2 g of REO or REC, and a desired initial collector concentration of $5x10^{-4}$ molarity (M). Using the initial collector concentration, the solution volume, and the molecular weight of SHA (153.14 g/mol), the mass of collector to add could be determined:

**Equation 1**

$$5x10^{-4}M * 0.2L * \frac{153.14g}{mol} = 0.0153g \; salicyl$$

After weighing out 0.0153 g of SHA and 2 g REE, 200 mL of deionized water was poured into a 200-mL beaker. Deionized water was used to decrease risk of cross-contamination with other chemicals that may be present in potable water. The solution was manually adjusted to the desired pH using crushed sodium hydroxide (NaOH) tablets. Hydrochloric acid (HCl) was administered on a one molar basis in the event that the pH became too alkaline. SHA was then added to solution and allowed to mix for at least twenty minutes to achieve a homogeneous mixture. The pH was then readjusted since SHA is a mild acid and typically reduced the pH to around 6 or 7.

A 5-mL sample of the alkaline solution was pulled using a disposable 10-ml syringe and prepared for measuring the solution's initial concentration. A 5-micron filter was attached to the syringe to filter the solution as it was distributed into a smaller beaker. This sample was mixed with 10 mL of ferric perchlorate solution to react and form a product which consisted of a purple hue, the intensity of which was directly proportional to the concentration of SHA in solution. Ideally, as more collector adsorbed onto an REE surface, the concentration of collector in solution would decrease and the purple hue would subsequently lighten. The color change induced by ferric perchlorate can be seen in Figure 8.
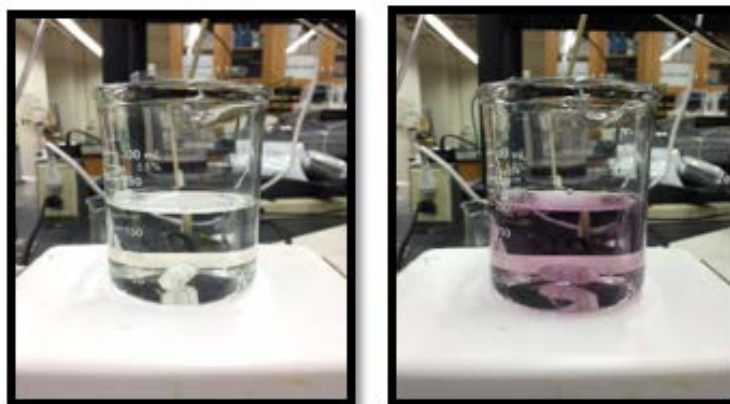


**Figure 8: SHA Solution Before Adding Ferric Perchlorate (left) and After (right)**

Ferric perchlorate was produced in the lab and comprised of 455 mL ethanol, 35 mL perchloric acid, and 10 mL iron perchlorate. Mixing these components took place in an ice bath to neutralize any exothermic reactions occurring. The amount of ferric perchlorate to add to collector solution conforms to a ratio that was used in a study by Natarajan and Fuerstenau (1983) involving OHA and ferric perchlorate.

A portion of the purple solution was then poured into a quartz cuvette to be placed inside the VWR UV/VIS instrument to measure absorbance of the product. The absorbance reading was then incorporated into a variation of the Beer's Law equation, along with the molar absorptivity of SHA, to calculate initial collector concentration, as shown in Equation 2:

**Equation 2**

$$x = \frac{y - 4x10^{-5}}{453.52}$$

where x is concentration in moles/liter, y is absorbance, and 453.52 is the molar absorptivity of SHA. After recording the initial concentration, two grams of REO or REC were mixed in with the original 200-mL solution and a 5-mL sample was summarily extracted and filtered to observe any immediate change in collector concentration with the addition of REE. This process was repeated typically on the order of every half hour until the collector concentration stabilized, with the total number of sample pulls dependent on the kinetics between the collector and rare earth of interest. Overall, tests could stabilize in as little as one hour or run as long as six hours.

## 3.2. StabCal Solubility Curves

Thermodynamic software StabCal (Stability Calculations), developed by Dr. Hsin Huang (2016) at Montana Tech, was utilized to theoretically estimate the optimal pH ranges for floating selected REOs and RECs using SHA. Additionally, StabCal was used to obtain theoretical PZCs for oxide and carbonate forms of Ce, Pr, Eu, and Tb. Solubility curves were developed for these

rare-earths both with and without collector to observe the effects of SHA on the REO and REC systems. Comparison of oxide solubility curves to their respective carbonates and identifying where solid states overlapped could help indicate whether carbonation of oxides was occurring as the collector adsorbs onto the mineral surface. Pertinent thermodynamic data was extracted from the software's LLNL database to construct the necessary plots since the information from this database pertains specially to aqueous systems for REEs. Stability constants for the trivalent REE cations with SHA were taken from Liu et al. (1989) and incorporated into the software to calculate the free energies for the following reactions:

$$R^{3+} + SHA^- \rightarrow R(SHA)^{2+}$$

$$R^{3+} + 2SHA^- \rightarrow R(SHA)_2^+$$

$$R^{3+} + 3SHA^- \rightarrow R(SHA)_3$$
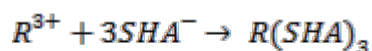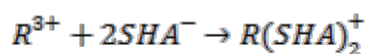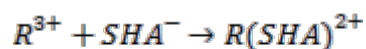
where R and SHA represent the rare-earth of interest and collector, respectively. Free energy values were then calculated in StabCal based on the van't Hoff reaction isotherm:

**Equation 3**

$$\Delta G_R^\circ = -RT \ln K$$

where $\Delta G_R^\circ$ is the standard free energy of reaction, R is the gas constant at 1.987 cal/mol-K, T is temperature at 298.15 Kelvin, and K is the equilibrium constant for the given reaction.

Computed free energy values for each reaction are listed in Appendix E, along with their respective stability constants. These constants represented a measure of the strength of the bond between the rare-earth and SHA reagents and thus provided the means to calculate concentrations of the SHA complexes in solution. Constants for europium were not provided and

had to be manually determined by plotting known K values for the other rare earth ions against their inverted ionic radii (Shannon, 1976) as shown in Figure 9. Subsequently, entering the known radius value for Eu into the resulting equation yielded an equilibrium constant for Eu. This method was applied based on data from Kawabe (1992) and Kulprathipanja (1974) who related atomic number and stability constants to ionic radii of REEs. Table II presents inverted REE ionic radii (Shannon, 1976) and the corresponding $K_1$, $\beta_2$, and $\beta_3$ (Liu, et al., 1989). Constants for Eu that were calculated using the constructed plot in Figure 9 are highlighted in the table.
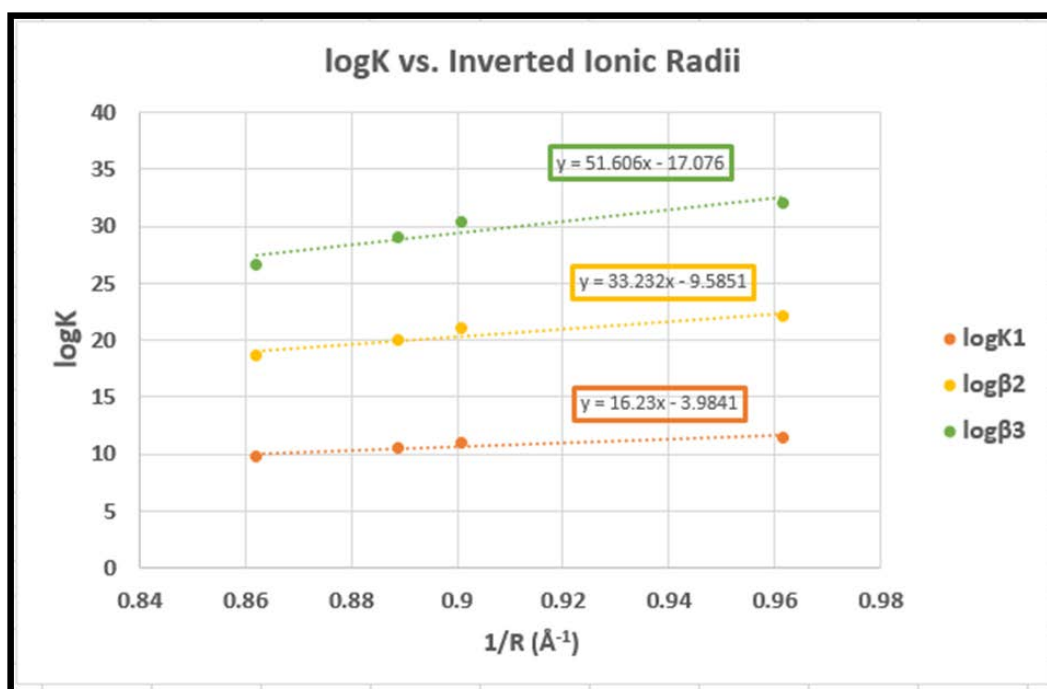


**Figure 9: logK Values Graphed Against 1/R for La, Pr, Nd, and Tb**

**Table II: Inverted Ionic Radii and Stability Constants of Selected Rare Earth Ions with SHA**

| Complexing Ion | 1/R (Å$^{-1}$) | logK$_1$ | logβ$_2$ | logβ$_3$ |
|---|---|---|---|---|
| H$^+$ | | 10.95 | | |
| La$^{3+}$ | 0.862069 | 9.79 | 18.62 | 26.66 |
| Ce$^{3+}$ | 0.874891 | 10.14 | 19.23 | 27.69 |
| Pr$^{3+}$ | 0.888889 | 10.48 | 19.98 | 29.03 |
| Nd$^{3+}$ | 0.900901 | 10.95 | 21.05 | 30.37 |
| Eu$^{3+}$ | 0.934579 | 11.18 | 21.47 | 31.15 |
| Tb$^{3+}$ | 0.961538 | 11.49 | 22.09 | 32.11 |

Solubility plots were then developed by first selecting a database in the software from which to import relevant thermodynamic values and defining a set of parameters for the system, including the number of components (excluding oxygen or hydrogen), as well as the valence and concentration of each component (Figure 10). For any oxide with SHA, the two components are the rare earth of interest and SHA. SHA is represented as "Ob" in the StabCal software. Mass input for the rare earth was entered at 0.001 mol/L, while the SHA concentration was adjusted for multiple runs, depending on whether noticeable changes could be detected. The total number of imported species from the LLNL database are also recorded in the worksheet. This procedure was repeated for the carbonates, with carbon as an additional component to the system and a constant mass input of 0.0015 to account for the 3:2 ratio of carbonate to REE. Finally, the procedures were repeated to consider OHA, abbreviated as "Oa" in StabCal.

**Figure 10: StabCal Worksheet for Pr Oxide with SHA Listing Fundamental Plot Parameters**

Diagrams without collector that modeled only the oxides and carbonates were used to determine a theoretical PZC. An initial pH value was selected based on where the positively and negatively charged species on the plot intersected. A mass balance was then constructed by approximating concentrations of the charged species present on each plot. The $H^+$ and $OH^-$ ions, whose values were determined by the selected pH, were also included in the calculations.

It should be noted that all plots and estimations were based on solution speciation, since values for a surface precipitate for the select oxides and carbonates could not be procured; however, unsuccessful titration experiments have been conducted to determine them and are a subject of ongoing research efforts.

### 3.3. Experimental Points of Zero Charge

#### 3.3.1. Background

Points of zero charge (PZCs) were experimentally determined using the Stabino to compare to theoretical estimations. The Stabino is an instrument that utilizes the streaming potential method to measure particle surface charge. The apparatus was equipped with an oscillating piston and PTFE cylinder chamber into which particles were dispersed, and two electrodes that received the signal from the piston. Adherence to the chamber wall immobilized the particles and permitted mobile excess ions to flow by means of the oscillating piston. Constant movement induced by the piston created a streaming current at the electrodes which could be used to determine zeta potential. In addition, two tubes were positioned above the chamber to administer the titrants that connected to different reservoirs.

#### 3.3.2. Setup

For this study, REO and REC samples were individually measured out using the following equation:

**Equation 4**

$$REO, REC = \left(0.0005\,\frac{mol}{L}\right) * 0.1L * MW$$

where REO, REC is the amount of oxide or carbonate in grams, 0.0005 is the desired concentration in mol/L, 0.1 is the volume of solution in liters, and MW is the molecular weight of the REO or REC in g/mol. The sample was then added to a beaker with 100 mls of DI water, and the solution was lowered to a pH of around 3 using 1.0M HCl. After pH adjustment, 8 mL of the sample was distributed into the white cylinder as shown in Figure 11. Tests that operated

with 0.1M NaOH as a titrant were designed to start at approximately pH 3 and end at pH 10.

Tests that employed 0.1M HCl as a titrant started at pH 12 and ended at pH 3. Both the zeta

potential and pH values were imported into and graphed in Excel. All oxides and carbonates

were tested excluding cerium oxide, whose PZC had already been previously determined and

verified by other studies (Nicholas et al., 2016; Hattori & Masakuni, 2004). Cerium oxide was

also not tested since the StabCal plots used data for trivalent cerium and were unable to model

Ce with a tetravalent charge for valid comparison.
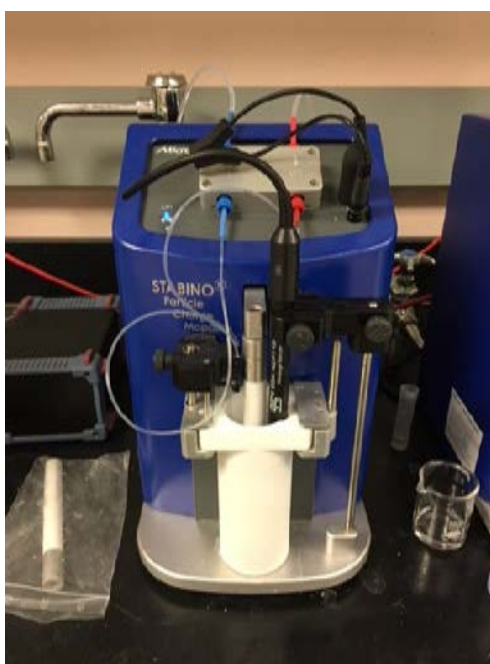


**Figure 11: Stabino Titration Analyzer**

## 3.1. Adsorption Density Studies

Kinetic studies with adsorption density were also conducted to elucidate an adsorption

mechanism between SHA and the REM surface. Adsorption density was calculated by

implementing the following equation:

Equation 5

$$\Gamma = \frac{(C_i - C_f) * V}{A}$$

where $\Gamma$ denotes adsorption density in moles/cm$^2$, $C_i$ and $C_f$ respectively denote initial and final concentrations in mol/liter, V denotes volume of solution in liters, and A denotes surface area in cm$^2$/g. Surface areas for REOs and RECs of interest were obtained using a Quantachrome BET Analyzer and are provided in Table III. Measured concentrations were subtracted from the initial concentration value of $5 \times 10^{-4}$ M SHA and multiplied by the original 200-mL volume. Adsorption densities were then graphed to model the appearance of SHA onto the REM surface as a function of time (see Appendix B).

**Table III: BET Surface Areas for Tested REOs and RECs**

| REE | Oxide Surface Area (m$^2$/g) | Carbonate Surface Area (m$^2$/g) |
|---|---|---|
| Cerium | 12.00 | 12.88 |
| Praseodymium | 1.40 | 3.56 |
| Europium | 4.31 | 9.13 |
| Terbium | 1.09 | 2.06 |

Adsorption isotherms were also attempted in order to calculate thermodynamic values that could indicate the occurrence of physisorption or chemisorption. A set of nine tests were performed each at 20°C and approximately 60°C. For both temperatures at pH 10, each test commenced at a different initial SHA concentration, with the first test starting at $1 \times 10^{-4}$ M and the last test starting at $9 \times 10^{-4}$ M. For both temperatures at pH 11, the first test began at $2 \times 10^{-4}$ M and the ninth test began at $1 \times 10^{-3}$ M. Samples were pulled approximately one day after starting the tests to measure final concentrations using the same procedure detailed for the equilibrium studies. Adsorption densities were then calculated and graphed against final concentrations in

order to produce isotherms based on the Langmuir model. Subsequently, the isotherms could establish the occurrence of monolayer or multilayer adsorption, and therefore the validity of thermodynamic calculations. Given the molarity of water and equilibrium constant K, obtained via linear regression, the free energy of adsorption for the system could be determined using a variation of the Stern-Langmuir Equation:

**Equation 6**

$$\Delta G_{ads} = -RTln\left(\frac{K}{0.018}\right)$$

The two free energies and temperature values were then substituted into the Clausius-Clapeyron Equation (Equation 7) to calculate enthalpy and subsequently the entropy of adsorption:

**Equation 7**

$$\Delta H_{ads} = \frac{\left(\frac{\Delta G_{T1}}{T_1}\right) - \left(\frac{\Delta G_{T2}}{T_2}\right)}{\left(\frac{1}{T_1}\right) - \left(\frac{1}{T_2}\right)}$$

**Equation 8**

$$\Delta S_{ads} = \frac{\Delta H_{ads} - \Delta G_{avg}}{T_{avg}}$$

Adsorption isotherms at pHs 10 and 11 were performed only on terbium oxide, based on conclusions gleaned from the results which are later discussed.

# 4. Results and Discussion

A series of experiments was performed to quantify the adsorption mechanism between the anionic collector SHA and the oxide and carbonate forms of four REEs: cerium (Ce), praseodymium (Pr), europium (Eu), and terbium (Tb). Collector disappearance from solution was measured, and the appearance of SHA onto the surface of each rare earth was calculated to analyze adsorption kinetics. Experimental data were compared to speciation diagrams which were constructed using StabCal thermodynamic software in order to more accurately depict the interaction occurring at the mineral surface. Equilibrium tests were also conducted in previous studies (Nicholas et al., 2016; Young et al., 2017) on the oxides and carbonates of lanthanum (La), neodymium (Nd), dysprosium (Dy), and yttrium (Y). Results from these studies are provided in Appendix A for comparative and archiving purposes.

## 4.1. Equilibrium Studies

### 4.1.1. Rare Earth Oxides

Equilibrium tests were performed at pH levels 9, 10, and 11 at 20°C to determine collector concentration in solution with each of the four oxides. Figure 12 and Figure 13 depict the adsorption kinetics of SHA in Ce and Pr oxide, respectively. Figure 12 shows that, for Ce, SHA almost completely disappears from solution at pHs 10 and 11, and within three hours at pH 9. Additionally, the graph indicates that strongest and quickest adsorption occurs at pH 10. For Pr oxide (Figure 13), adsorption is noticeably strongest and occurs most quickly at pH 9, whereas pHs 10 and 11 exhibit almost identical adsorption trends.
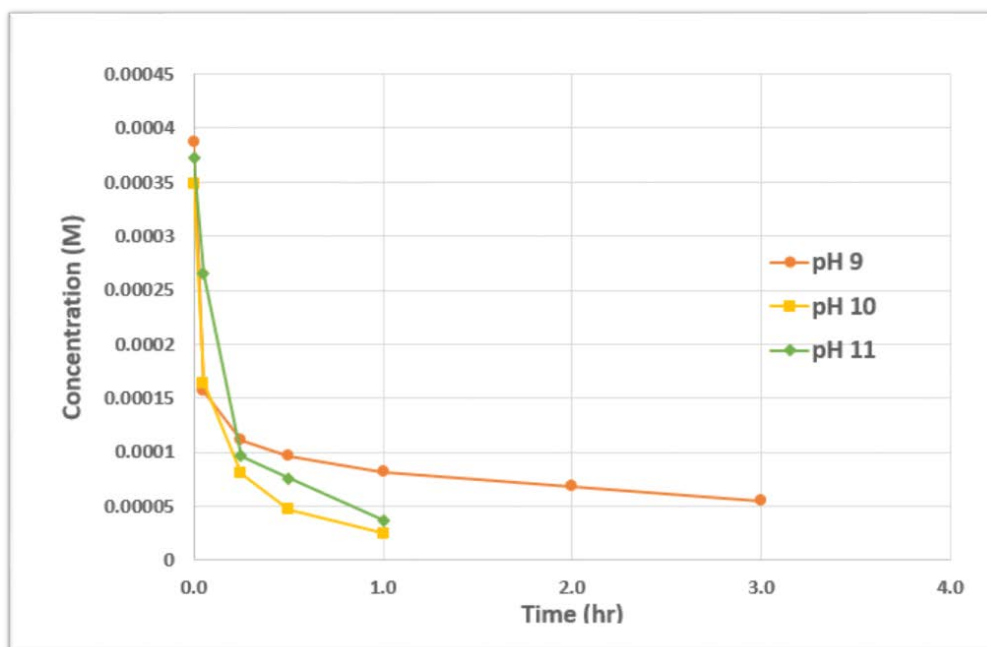
**Figure 12: Equilibrium Concentration of SHA in Ce Oxide at 20°C**
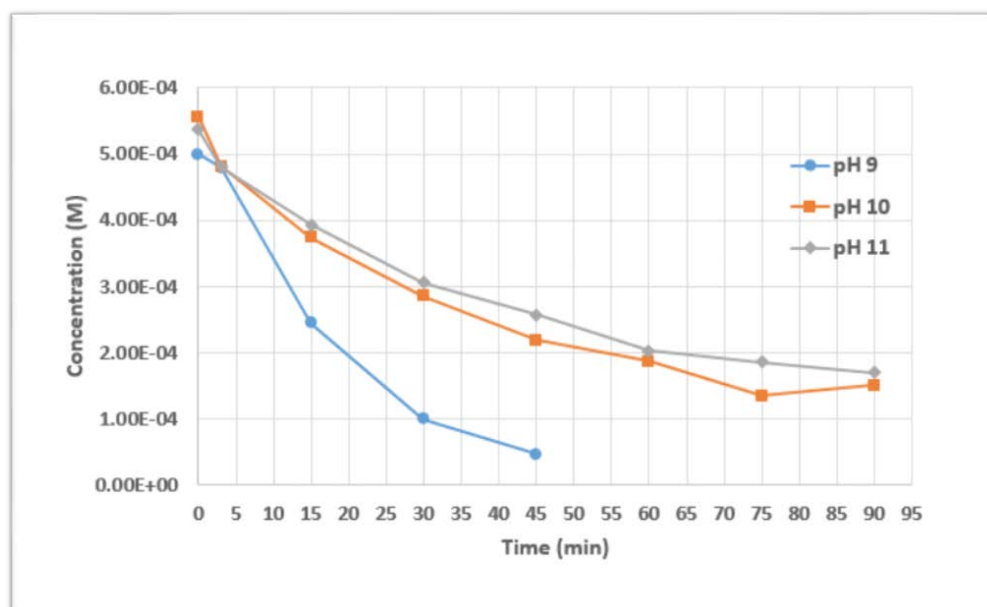


**Figure 13: Equilibrium Concentration of SHA in Pr Oxide at 20°C**

Figure 14 and Figure 15 display the results of SHA adsorption onto Eu and Tb oxide

respectively at room temperature. Eu oxide exhibits noticeably weaker adsorption at all pH levels

than for those of Ce and Pr. The oxide appears to stabilize an hour after its addition to the

solution, and subsequently the system never reaches zero even after six hours. Despite poor

adsorption overall, the most adsorption appears to occur at pH 9 throughout the test. Weakest

adsorption is observed for Tb oxide at all pH levels. Adsorption at pH 9 for Tb is poorer than that

for Eu oxide but still represents the level at which most adsorption occurs, along with pH 10.
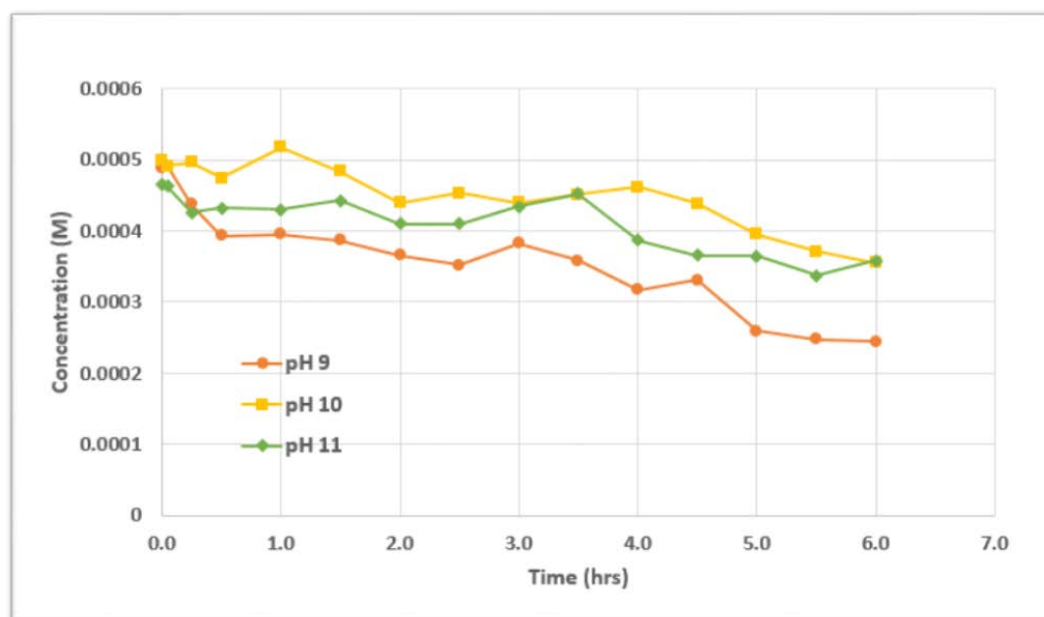


**Figure 14: Equilibrium Concentration of SHA in Eu Oxide at 20°C**
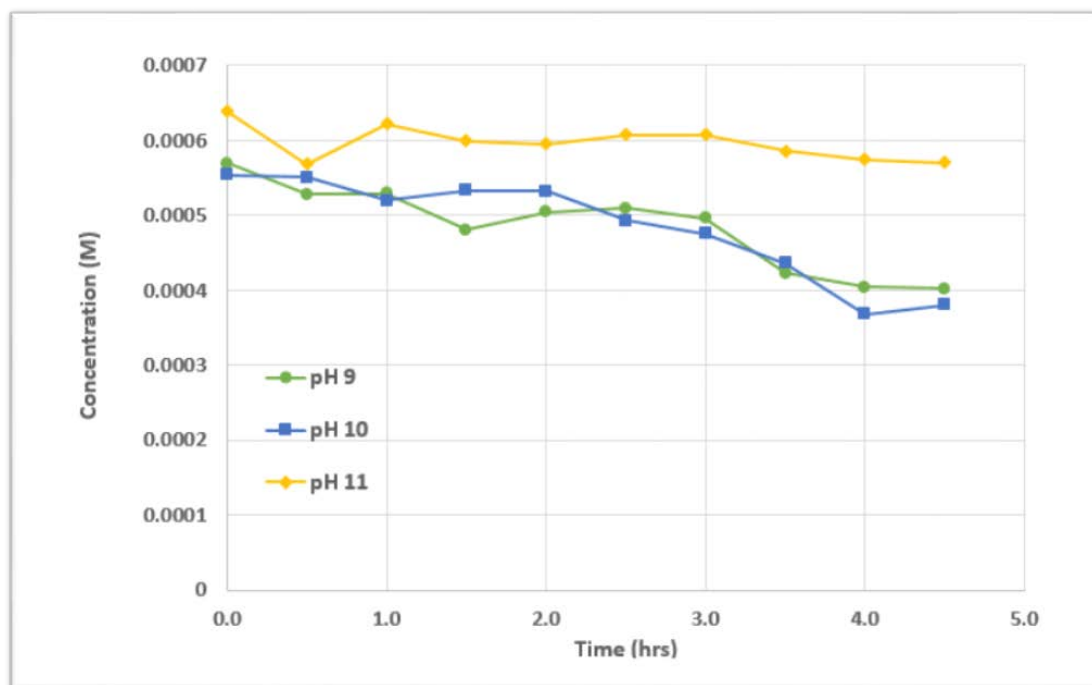
**Figure 15: Equilibrium Concentration of SHA in Tb Oxide at 20°C**

Figures 12-15 suggest that adsorption decreases in REOs with smaller ionic radii. Cerium oxide achieved the fasted equilibration and exhibited the highest level of adsorption. Praseodymium, the next lightest element in the selected group of REEs, also achieved a considerable amount of SHA adsorption at all three pHs. Adsorption appears strongest at pH 10 for Ce and at pH 9 for Pr. However, much less adsorption occurred for the heavier elements Eu and Tb. Salicyl adsorbed most strongly onto these oxides at pH 9, but still much more poorly than for Ce and Pr at the same pH. For all four oxides, the least amount of adsorption can be seen with pH 11. These data are consistent with results from Nicholas et al. (2016) which revealed a similar trend with the oxide forms of lanthanum and yttrium. Lanthanum achieved equilibrium for pHs 9 and 10 within six hours, whereas yttrium never reached equilibrium at any of the tested pH levels.

Three key aspects should be noted from the above results. First, the order of SHA adsorption for oxides is moderately pH-dependent but clearly decreases kinetically as follows: Ce > Pr > La > Nd > Y > Eu > Dy > Tb, which concurs with decreasing REE ionic radii. Second, several instances can be seen where SHA concentrations initially decrease in solution but later increase which suggests occurrence of SHA desorption: Y at pH 9, Eu at pH 11 and pH 10; Dy at pHs 9, 10, and 11; and Tb at pH 11. This behavior appeared only when SHA adsorption was weak and is attributed to the competition of SHA for the REO surface with carbonate ($CO_3^{2-}$ or $HCO_3^-$) since experiments were performed in open air. Third, RECs were investigated because of these observations with REOs. Desorption tended to occur at higher pH, and subsequent thermodynamic modeling depicts a shared equilibrium between REOs and RECs near these pH levels.

### 4.1.2. Rare Earth Carbonates

Equilibrium tests were repeated for the four rare earth carbonates (Ce, Pr, Eu, and Tb) at pHs 9, 10, and 11 to compare SHA adsorption to results for the oxides. Figure 16 and Figure 17 show collector adsorption onto Ce and Pr carbonate as a function of time. Ce carbonate appears to stabilize less than an hour after introducing it to the system, indicating very poor adsorption even after six hours. Adsorption for Pr carbonate is slightly better in that SHA adsorbs more strongly onto the surface in much less time. Adsorption of SHA onto the carbonate surfaces of Eu and Tb are displayed in Figure 18 and Figure 19. The level of adsorption in Pr and Eu carbonate appears about the same at pHs 9 and 10; however, SHA disappears almost completely in Tb carbonate within an hour at pHs 9 and 11, imitating Ce oxide behavior.
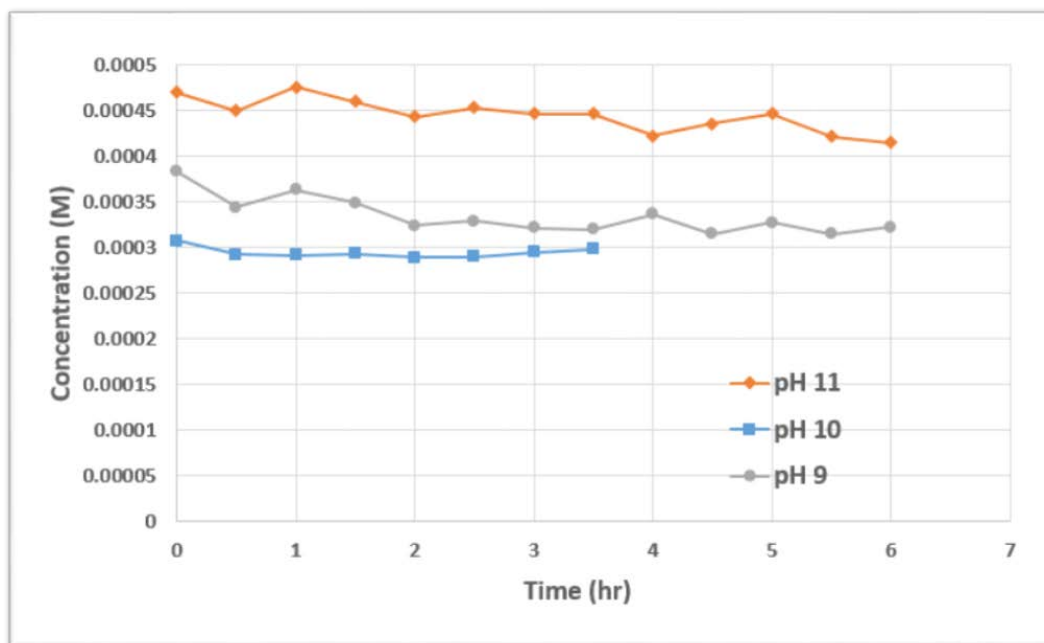
**Figure 16: Equilibrium Concentration of SHA in Ce Carbonate at 20°C**
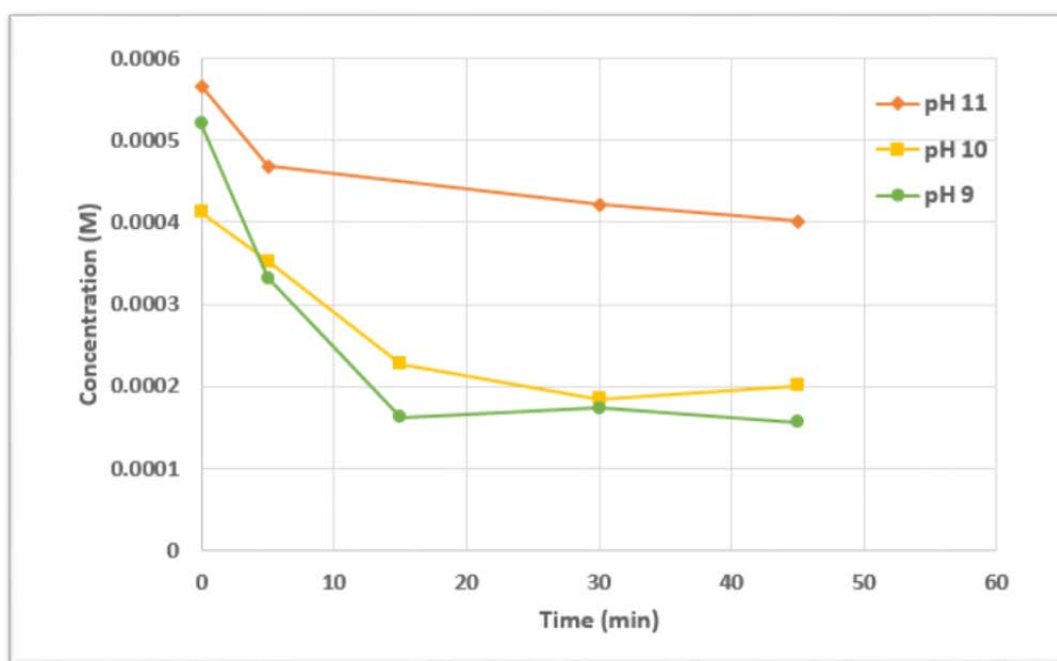


**Figure 17: Equilibrium concentration of SHA in Pr carbonate at 20°C**
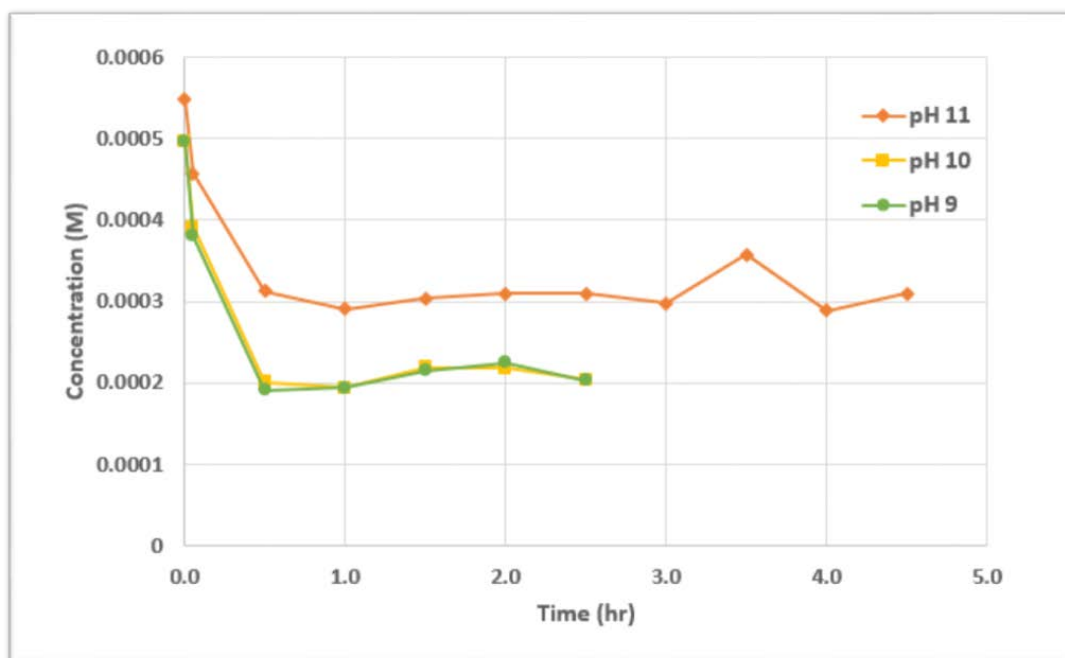
**Figure 18: Equilibrium Concentration of SHA in Eu Carbonate at 20°C**
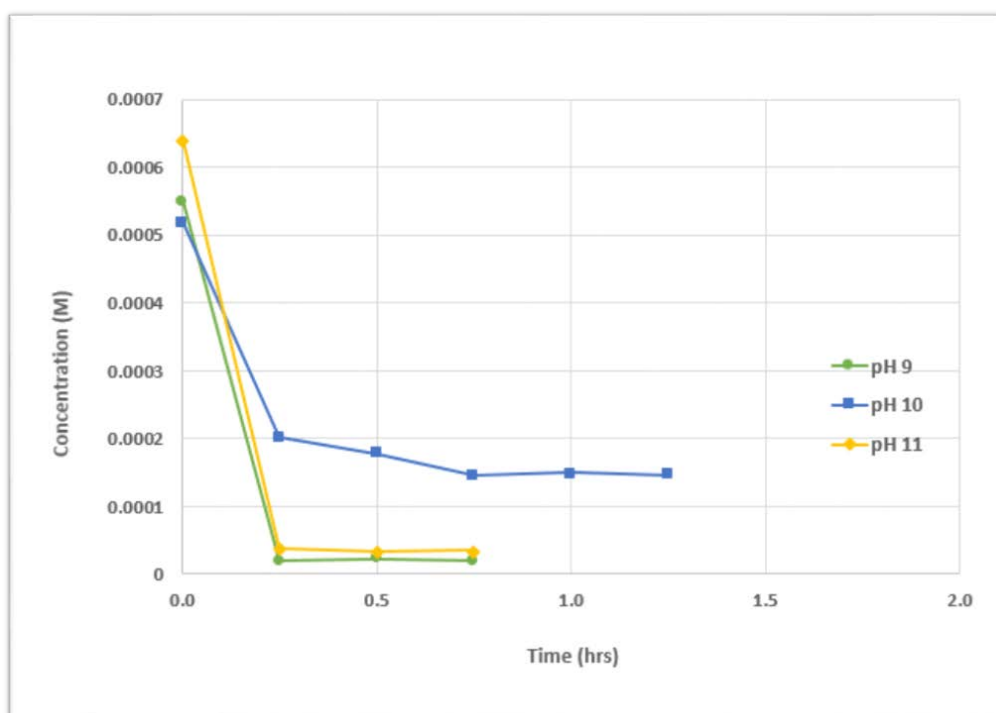


**Figure 19: Equilibrium Concentration of SHA in Tb Carbonate at 20°C**

When compared to results obtained for other previously studied RECs (see Appendix A), the order observed for the REOs is nearly reversed: Ce < La < Pr < Nd < Eu < Dy < Tb < Y. Complexation of REEs with carbonate may cause their ionic radii to increase which would favor the HRECs for SHA adsorption but not the LRECs. Consequently, perhaps the addition of carbonate as soda ash ($Na_2CO_3$) in the flotation slurry could aid in floating HREEs by preferentially forming HRECs. The LREOs would not be affected and thus would retain their high SHA adsorption and ability to float.

Figures 16-19 indicate an adsorption trend opposite from that of the oxides. Poorest SHA adsorption can be seen for cerium carbonate, the lightest rare earth, in Figure 16, which shows very little collector adsorbing onto the surface. Strongest and fastest adsorption kinetics occurred for terbium carbonate at pHs 9 and 11 within an hour of adding collector. Europium carbonate adsorbed less than terbium and almost the same as praseodymium. Adsorption kinetics are strongest at pH 10 for Ce, at pHs 9 for Pr, and at pHs 9 and 10 for Eu. However, for Eu at pH 11, SHA desorption may have occurred such that its surface may have converted from carbonate to oxide/hydroxide (see Figure 30 which is later discussed).

The trend for REOs that relates cationic size to that of the collector head group (as shown in Figure 6) and the 2.42Å spacing between the two coordinating oxygen atoms is a common property in hydroxamates known as chelation (Zhao, et al., 2013). To demonstrate, ionic diameters of selected rare earth oxides (Shannon, 1976) are displayed in Table IV along with the aforementioned spacing. REOs with ionic diameters (i.e. LREEs) close to the SHA head group size exhibit much stronger and faster adsorption in the equilibrium studies, whereas REOs with much smaller ionic diameters (HREEs) exhibit poor adsorption kinetics.

**Table IV: Effective Ionic Oxide Diameters of Trivalent Eight-Coordinate REE Cations**

| REE | Atomic No. | Diameter (Å) |
|---|---|---|
| SHA | -- | 2.42 |
| $La^{3+}$ | 57 | 2.32 |
| $Ce^{3+}$ | 58 | 2.29 |
| $Pr^{3+}$ | 59 | 2.25 |
| $Nd^{3+}$ | 60 | 2.22 |
| $Eu^{3+}$ | 63 | 2.14 |
| $Tb^{3+}$ | 65 | 2.08 |
| $Dy^{3+}$ | 66 | 2.06 |
| $Y^{3+}$ | 39 | 2.04 |

Furthermore, when considering RECs, ionic diameters are suspected to increase due to an increase in coordination number such that when LREEs coordinate with carbonate, they become too large to chelate. Conversely, diameters for the HREEs grow larger but chelate more effectively. Table V from Shannon (1976) provides ionic diameters for twelve-coordinate REE cations, illustrating that increasing diameter culminates in the LREEs becoming too large for chelation and the HREEs achieving a size sufficient for strong adsorption. This phenomenon can be attributed to differences in REE basicity in that the LREEs possess a lower affinity for electrons than do the HREEs, a property analogous to electronegativity as well as coordination chemistry. For this reason, Table IV was restricted to trivalent, eight-coordinate REE cations.

**Table V: Effective Ionic Oxide Diameters of Trivalent Twelve-Coordinate REE Cations**

| REE | Atomic No. | Diameter (Å) |
|---|---|---|
| SHA | -- | 2.42 |
| $La^{3+}$ | 57 | 2.72 |
| $Ce^{3+}$ | 58 | 2.68 |
| $Pr^{3+}$ | 59 | 2.64 |
| $Nd^{3+}$ | 60 | 2.62 |
| $Eu^{3+}$ | 63 | 2.56 |
| $Tb^{3+}$ | 65 | 2.50 |
| $Dy^{3+}$ | 66 | 2.48 |

## 4.2. StabCal Speciation Diagrams

Solubility plots were generated for the four rare earth oxides and carbonates using the thermodynamic program StabCal to analyze the theoretical interaction of REMs in solution in the presence and absence of both SHA and OHA. Diagrams without collector were also constructed to estimate PZCs. Hydroxides were modelled in lieu of oxides under the assumption that oxides convert to hydroxides in aqueous systems. Because OHA is commonly used in REM flotation, plots were also produced with and without octyl hydroxamate to compare its effects to those of SHA. StabCal was previously used to create similar speciation diagrams for REOs and RECs of La, Nd, Dy, and Y with and without SHA and OHA and are listed in Appendices C and D for comparative and archival purposes.

### 4.2.1. Rare Earth Oxides without SHA

Rare earth oxides were modeled without collector to establish a baseline for comparing to models with SHA and OHA collectors, as well as to determine points of minimum solubility and points of zero charge. Figures 20-23 show the diagrams for the four trivalent REOs with concentrations of 0.001M for each element. Results indicate that minimum points of solubility for $Ce(OH)_3$, $Pr(OH)_3$, $Eu(OH)_3$, and $Tb(OH)_3$ occur at pHs 11, 10, 9, and 9, respectively. PZCs for the four REOs are expected to fall close to these values (REF Parks, 1986 or Huang et al. 2010) and were respectively estimated at approximately pHs 8.75, 8.75, 8.25, and 7.75. Values from the graphs were calculated by finding the pH where the sum of the products of concentration and valence for all cations (including $H^+$) equals that for all anions including $OH^-$. The fact that these estimates fall about 1.25 pH units below minimum solubility suggests that this method for PZC estimation is inaccurate which may be due to the trivalent charge, whereas Parks

and Huang illustrated validity of the technique for divalent elements. Similar conclusions are

offered for the diagrams for La(OH)₃, Nd(OH)₃, Dy(OH)₃, Y(OH)₃ shown in Appendix C.
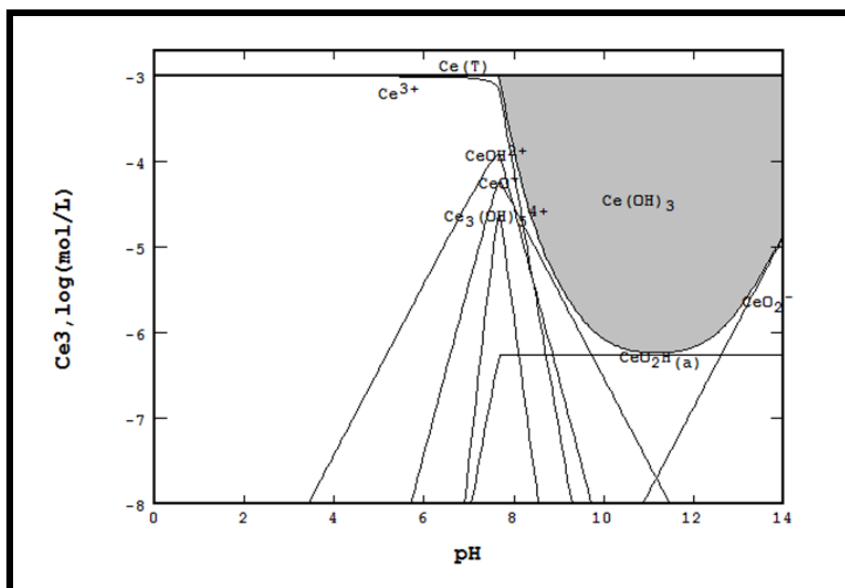


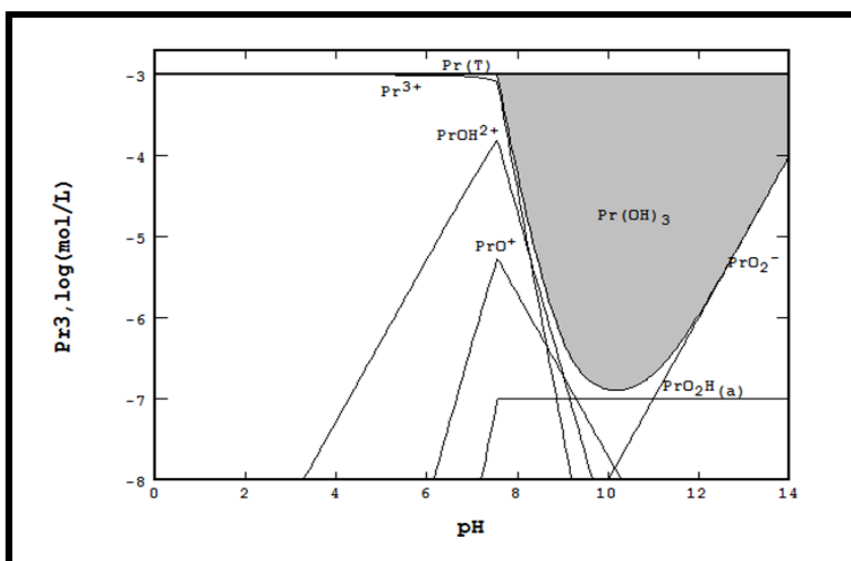**Figure 20: Solubility Plot for Ce Hydroxide without Collector**



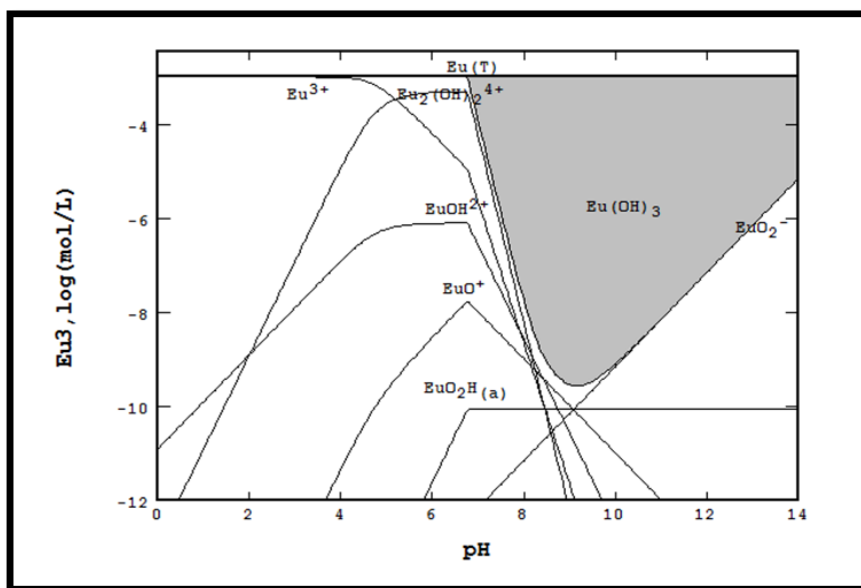**Figure 21: Solubility Plot for Pr Hydroxide without Collector**

**Figure 22: Solubility Plot for Eu Hydroxide without Collector**



**Figure 23: Solubility Plot for Tb Hydroxide without Collector**

### 4.2.2. Rare Earth Carbonates without SHA

Rare earth carbonates were also modeled without collector to establish a baseline for comparing models with SHA and OHA collectors, as well as to determine points of minimum solubility and PZCs. Figures 24-27 show the diagrams for the four trivalent RECs with concentrations of 0.001M for each element as well as 0.0015M for carbonate. Comparing RECs to REOs in Figures 20-23 revealed that RECs are more stable with stability ranges extending to lower pHs. Speciation diagrams for the carbonate systems exhibit up to three minimum points in the solubility curves with one below pH 10 due to presence of solely REC, another slightly above pH 11 due to only REO, and a third point above pH 10 due to a binary combination of REO and REC. Identifying these points established that RECs are truly only stable up to approximately pH 10 depending on the REE, a fact that helped explain why SHA adsorption on RECs was opposite that of REOs.

Results show that points of minimum solubility for $Ce_2(CO_3)_3$, $Pr_2(CO_3)_3$, $Eu_2(CO_3)_3$, and $Tb_2(CO_3)_3$ occur at pHs 11.5, 10, 12, and 10.5 respectively. PZCs for the four RECs are also expected to be close to these theoretical values (Huang, Twidwell, & Young, 2005) and were respectively estimated at approximately pHs 8.75, 8.75, 7.25, and 7.75 by finding the pH where the sum of the products of concentration and valence for all cations (including $H^+$) equals that for all anions (including $OH^-$). In this case, the PZC estimates either match well or are nearly 3-4 pH units below the minimum solubility, thereby suggesting that this technique is also an invalid approach for PZC estimation due not only to the trivalent charge but also to carbonate essentially complexing with the REEs under neutral conditions. Diagrams for $La_2(CO_3)_3$, $Nd_2(CO_3)_3$, and $Dy_2(CO_3)_3$ yield similar conclusions shown in Appendix C (Figures 85, 92, and 100).

**Figure 24: Solubility Plot for Ce Carbonate without Collector**



**Figure 25: Solubility Plot for Pr Carbonate without Collector**

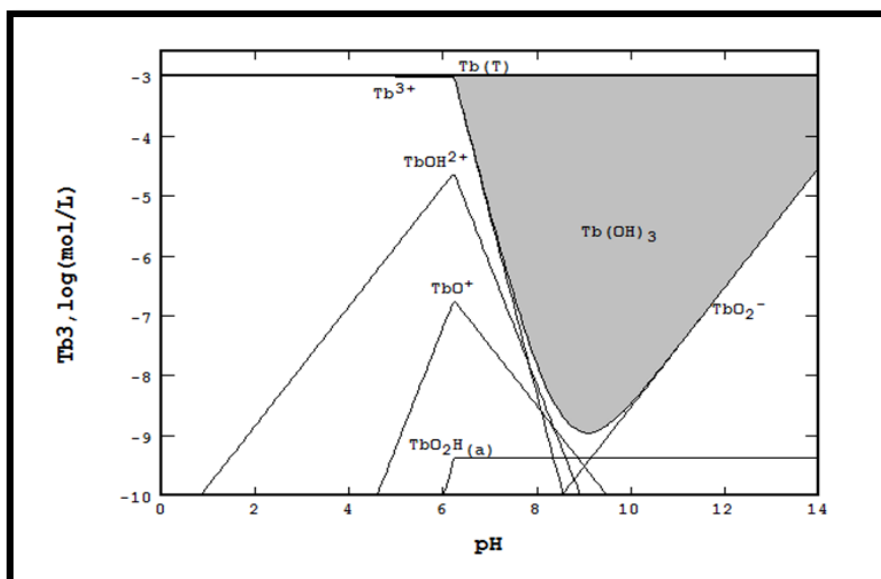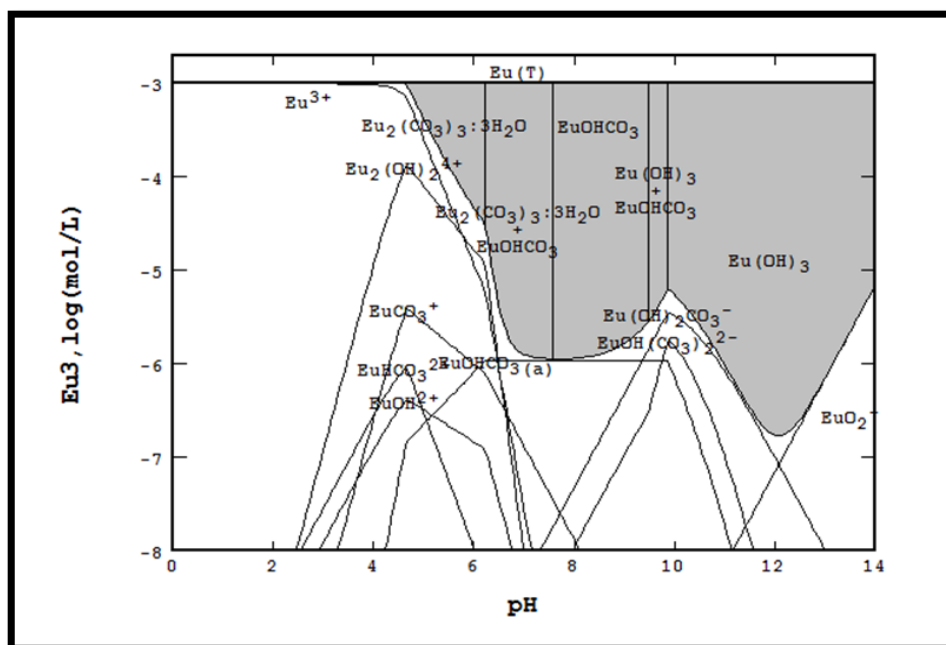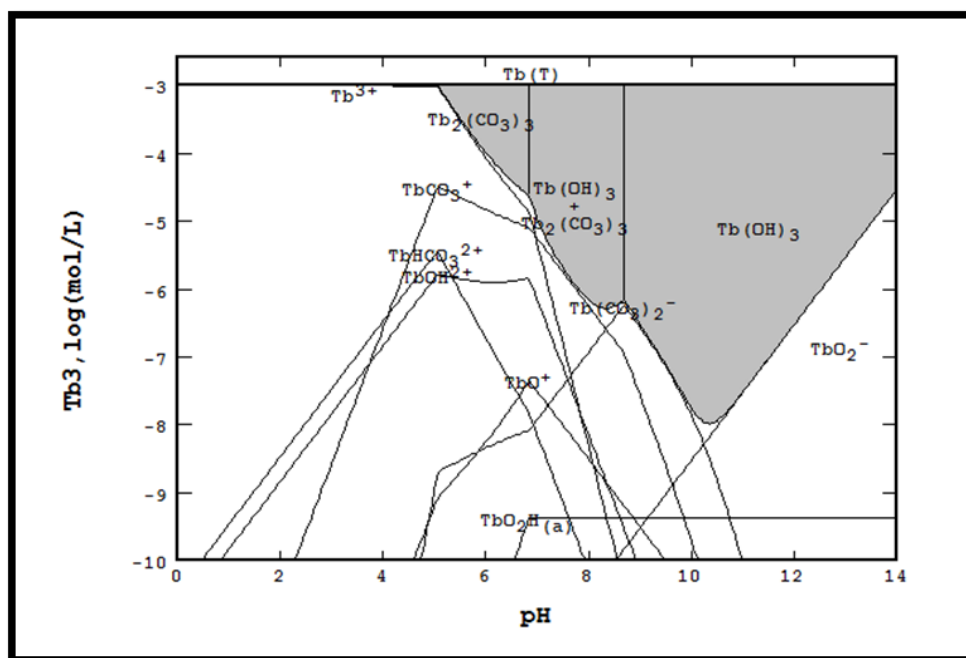**Figure 26: Solubility Plot for Eu Carbonate without Collector**



**Figure 27: Solubility Plot for Tb Carbonate without Collector**

A comparison of calculated PZCs both REOs and RECs using StabCal (Table VI)

suggests that PZCs decrease with decreasing ionic diameter. Several PZCs for RECs were

similar to those determined for REOs. For example, PZCs for the REOs and RECs of Tb and Pr

were the same at pH 7.75 and 8.75, respectively. Unfortunately, no continuous patterns were

detected in that similar PZCs occurred only for LREEs and not HREEs as anticipated.

Regardless, the obtained PZC results validate the postulation that carbonation of REM surfaces

and/or REE solution species with, for example, $Na_2CO_3$, could aid in REM flotation.

Table VI: StabCal PZC Results for Selected REOs and RECs

| REE | Oxide PZC | Carbonate PZC |
|---|---|---|
| Cerium | 8.75 | 8.75 |
| Praseodymium | 8.75 | 8.75 |
| Europium | 8.25 | 7.25 |
| Terbium | 7.75 | 7.75 |

### 4.2.3. Rare Earth Oxides with SHA and OHA

Solubility diagrams of the four selected REOs were constructed in the presence of SHA

or OHA at concentrations varying from $1 \times 10^{-7}$ to $1 \times 10^{-3}$ M. StabCal incorporated the same

thermodynamic data for each REO system and for each collector (see Appendix E) to perform

the calculations. Results were compared to those calculated in the absence of SHA and OHA as

previously presented in Section 4.2.1. Although thermodynamic data could not be successfully

obtained for precipitates of $RE(SHA)_3$ and $RE(OHA)_3$, the pH conditions where differences are

observed should indicate where collector adsorption occurs and thus the optimal pH conditions

for flotation.

Figure 28 shows the solubility diagrams for $Ce(OH)_3$ with $1 \times 10^{-5}$ M SHA (pictured left)

and $1 \times 10^{-5}$M OHA (right). Comparing these plots to $Ce(OH)_3$ in the absence of collector (see

Figure 20) depicts $Ce(OH)_3$ being "leached" with SHA from pH 8 to pH 13 but is barely

distinguishable for OHA near pH 8. Figure 29 manifests similar behavior at $1 \times 10^{-4}$ M SHA and

OHA where SHA again "leaches" the REO from pH 8 to pH 14, and OHA continues to barely interact (i.e., pHs 8 to 9). In fact, Figure 30 demonstrates that $1 \times 10^{-3}$ M only interacts with $Ce(OH)_3$ from pHs 8 to 10 and evidently requires significantly higher concentrations to produce the same results as SHA at $1 \times 10^{-5}$ M. These differences suggest SHA is more effective than OHA due to wider pH ranges at lower concentrations.



**Figure 28: Solubility Curves for Ce Hydroxide with 1E-5M SHA (left) and OHA (right)**



**Figure 29: Solubility Curves for Ce Hydroxide with 1E-4M SHA (left) and OHA (right)**

**Figure 30: Solubility Curve for Ce Hydroxide with 0.001M OHA**

Solubility plots for the remaining REOs are similar to those just discussed for Ce oxide in the presence of collector. For example, diagrams for Pr oxide are provided in Figures 31-34. Comparing $1x10^{-5}$ M to Figure 21 without collector shows SHA interacting between pHs 8-12 whereas OHA barely reacts at pH 8. Similarly, SHA reacts with Eu oxide reacts from pHs 7-13 while OHA hardly interacts at pH 8 (compare Figures 35-38 and 22). Likewise, Tb oxide interacts with SHA between pHs 7-13 and barely with SHA at pH 8 (compare Figures 39-42 and 23). Speciation diagrams for La, Nd, Dy, and Y oxides demonstrate similar behavior (see Appendices C and D). Collector performance illustrated in these plots suggests that SHA adsorbs more strongly than OHA due to its wider pH range at lower concentrations.
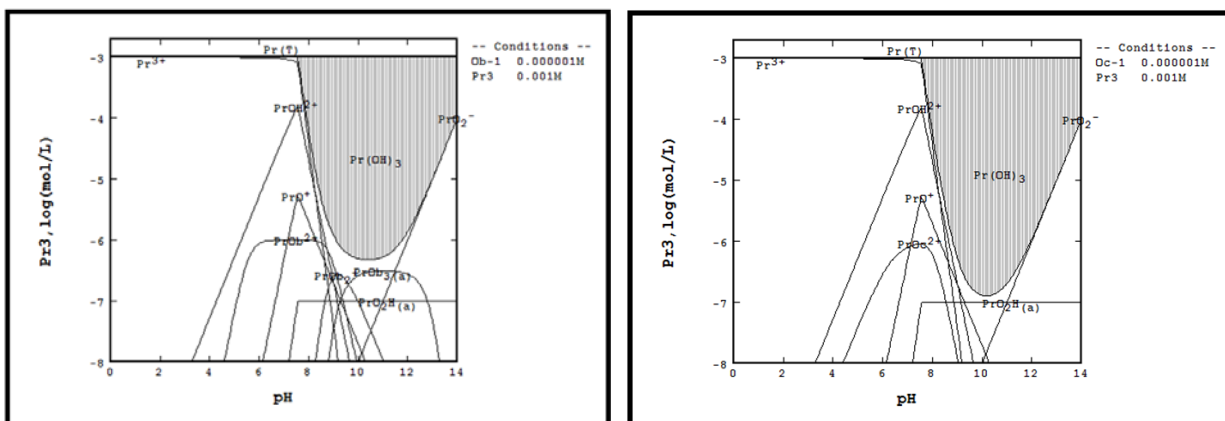
**Figure 31: Speciation Diagrams for Pr Hydroxide with 1E-6M SHA (left) and OHA (right)**
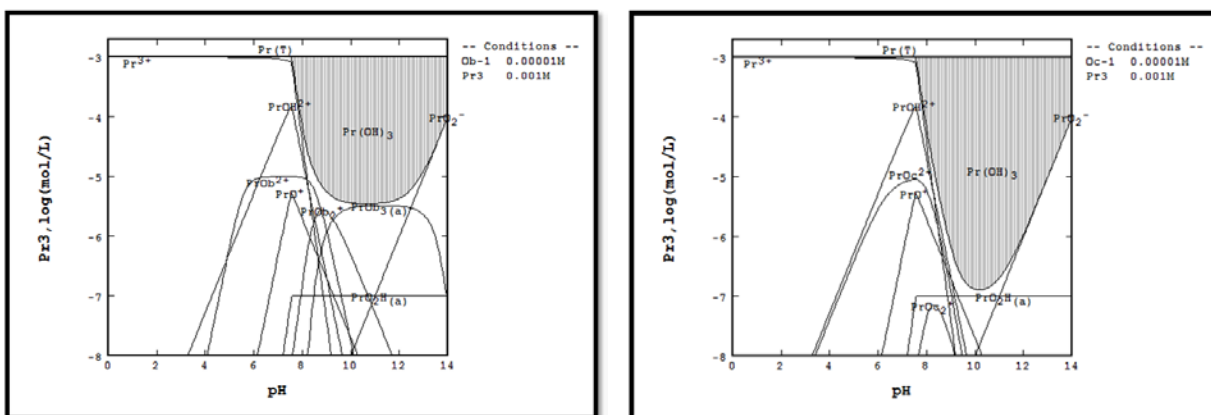


**Figure 32: Speciation Diagrams for Pr Hydroxide with 1E-5M SHA (left) and OHA (right)**
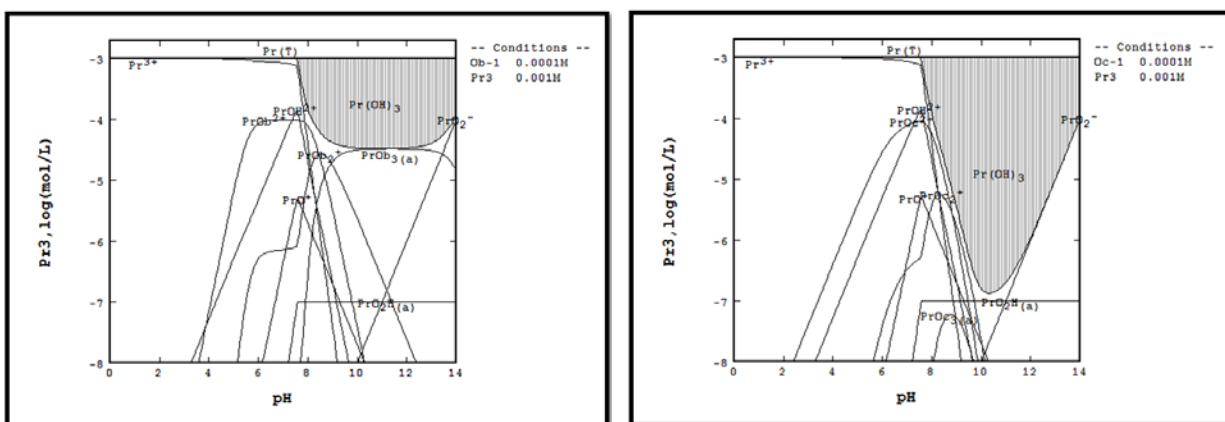


**Figure 33: Speciation Diagrams for Pr Hydroxide with 1E-4M SHA (left) and OHA (right)**

**Figure 34: Speciation Diagram for Pr Hydroxide with 0.001M OHA**



**Figure 35: Solubility Curves for Eu Hydroxide with 1E-6M SHA (left) and OHA (right)**

**Figure 36: Solubility Curves for Eu Hydroxide with 1E-5M SHA (left) and OHA (right)**



**Figure 37: Solubility Curves for Eu Hydroxide with 1E-4M SHA (left) and OHA (right)**
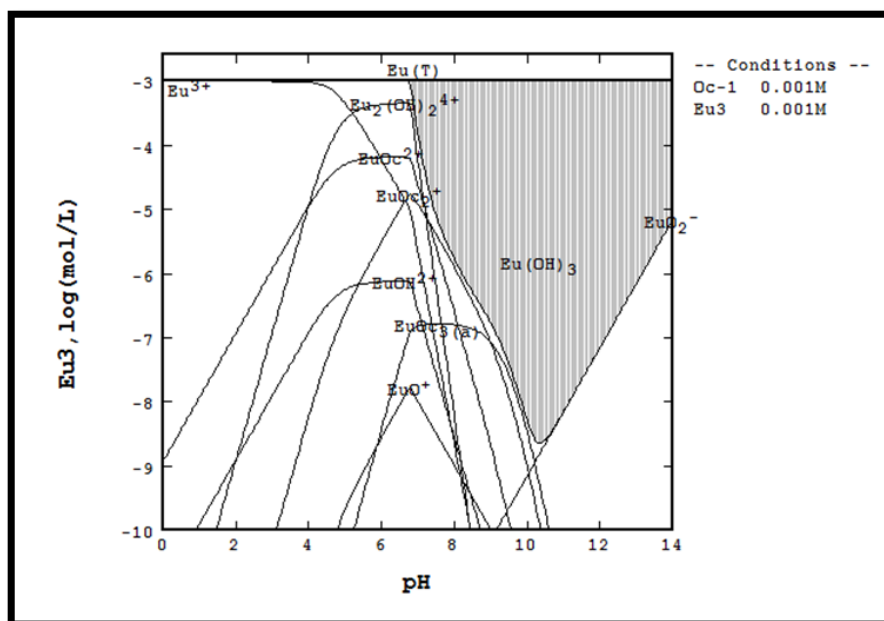
**Figure 38: Solubility Curve for Eu Hydroxide with 0.001M OHA**
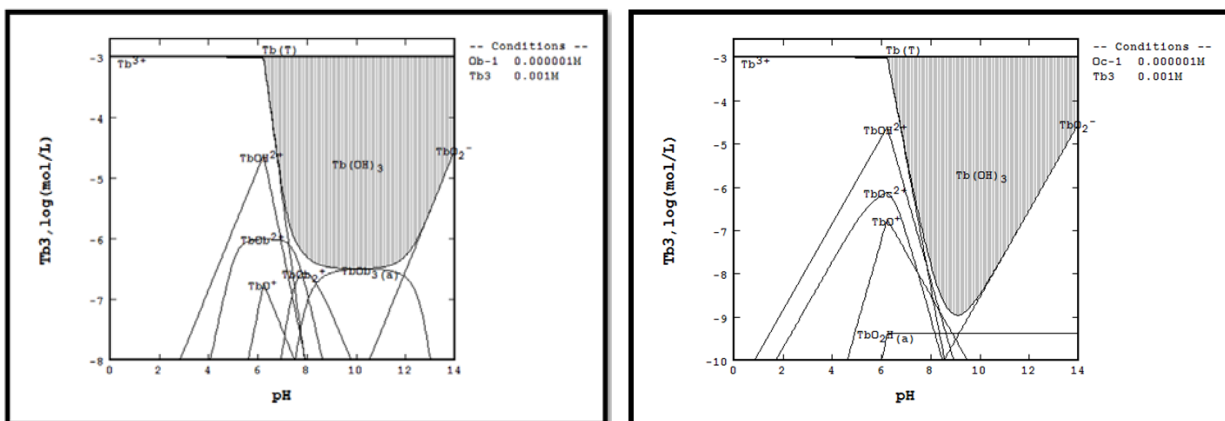


**Figure 39: Solubility Curves for Tb Hydroxide with 1E-6M SHA (left) and OHA (right)**
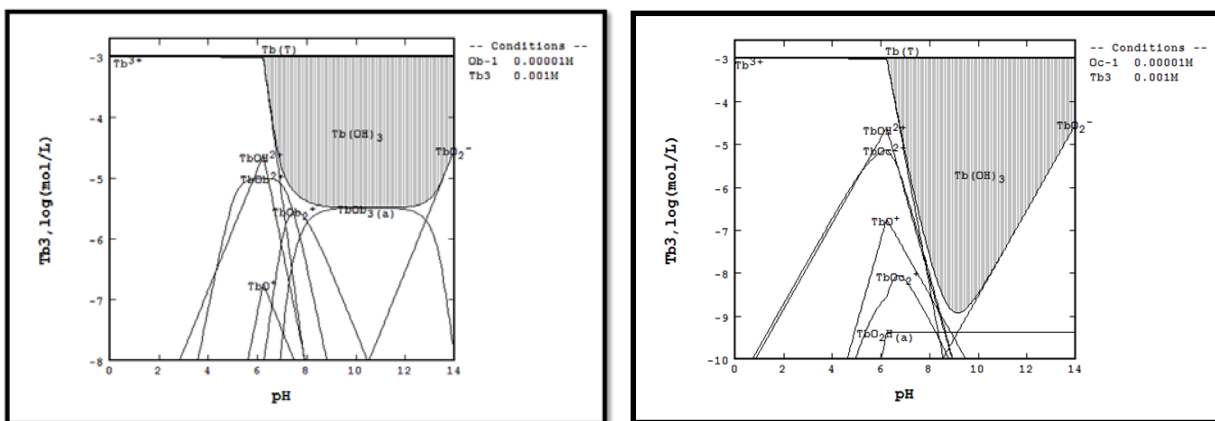
Figure 40: Solubility Curves for Tb Hydroxide with 1E-5M SHA (left) and OHA (right)
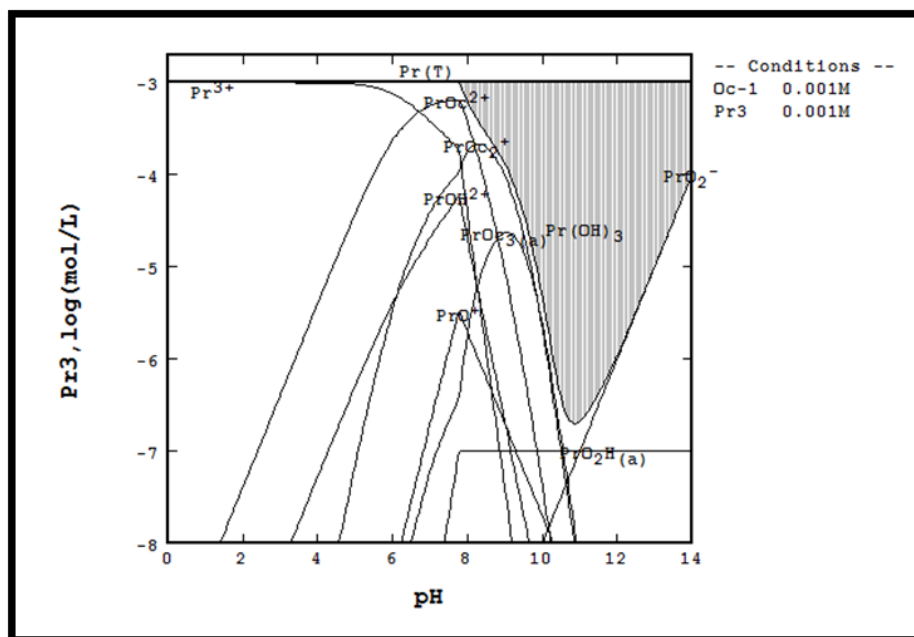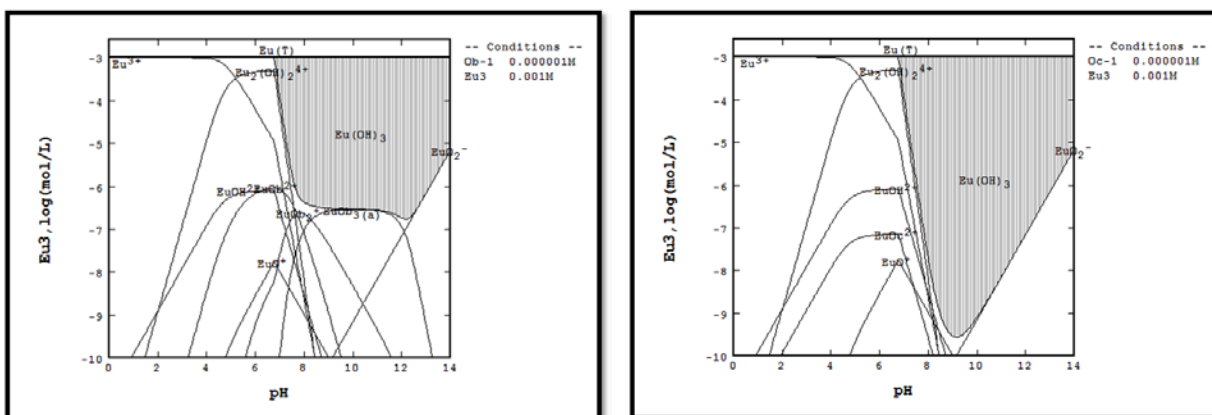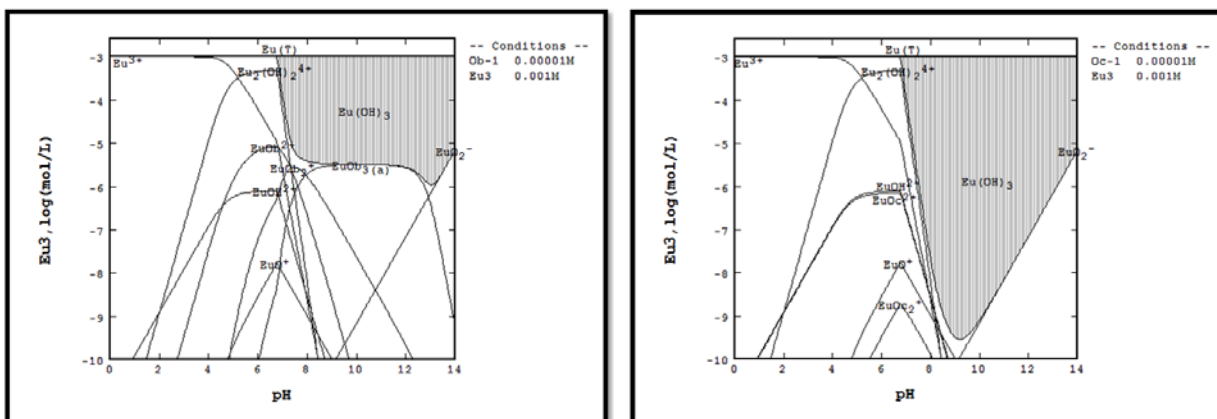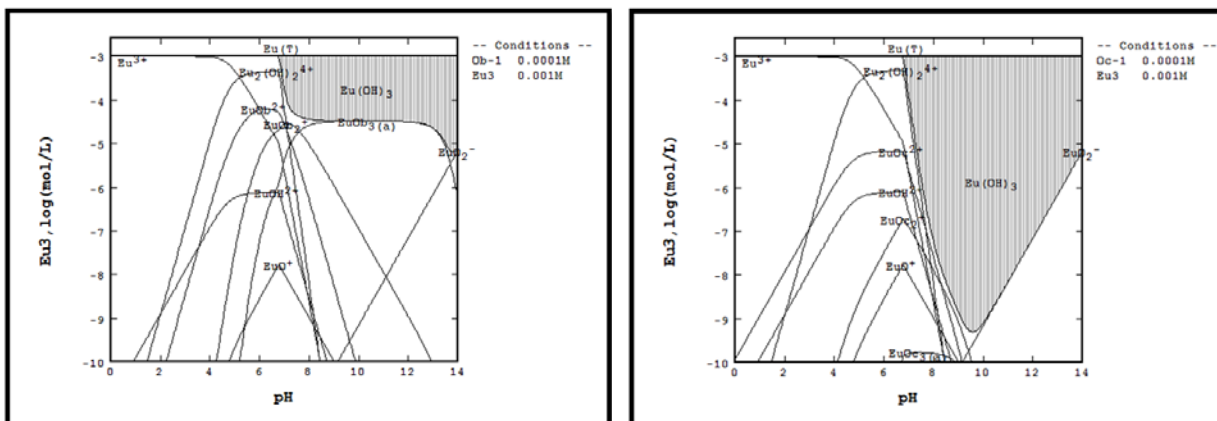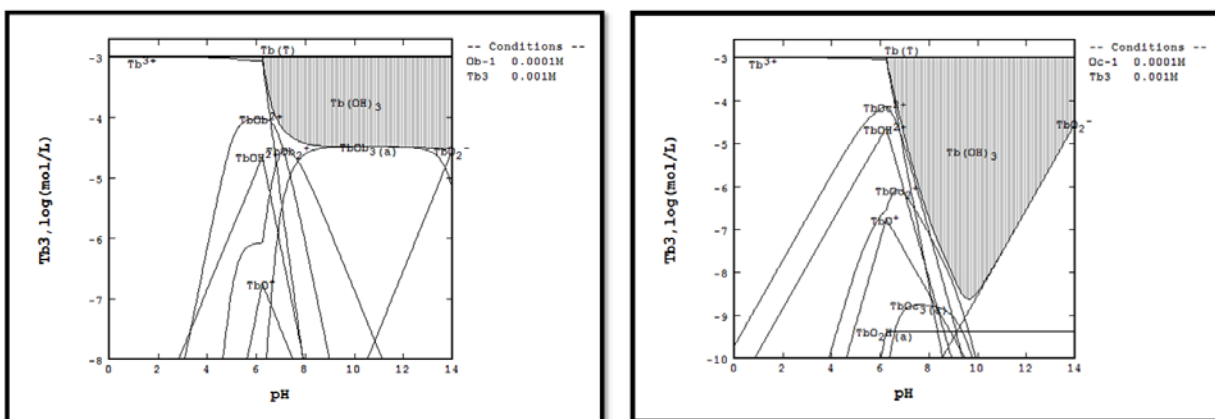
Figure 41: Solubility Curves for Tb Hydroxide with 1E-4M SHA (left) and OHA (right)

**Figure 42: Solubility Curve for Tb Hydroxide with 0.001M OHA**

### 4.2.4. Rare Earth Carbonates with SHA and OHA

Solubility plots were generated for RECs of the selected REEs Ce, Pr, Eu, and Tb in the presence of SHA or OHA at concentrations varying from $1 \times 10^{-7}$ to $1 \times 10^{-3}$ M, as well as $1 \times 10^{-2}$ M in a few cases. StabCal utilized the same thermodynamic data for each REC system and collector as used previously (Appendix E). Results are compared to those computed in the absence of collector as presented in Section 4.2.2. Variations among the diagrams are expected to indicate pH conditions where collector adsorption occurs, i.e. the pH ranges for flotation.

Figures 43-46 compare SHA and OHA solubility diagrams for the $Ce_2(CO_3)_3$ system. Comparing these graphs to $Ce_2(CO_3)_3$ in the absence of collector (see Figure 24) shows SHA "leaching" the REC between pHs 9 and 12 at $1 \times 10^{-6}$ M, pHs 7 and 13 at $1 \times 10^{-5}$ M, and pHs 6 and 14 at $1 \times 10^{-4}$ M. In contrast, OHA interacts at these same concentrations within smaller ranges of pHs 8 to 9, pHs 7 to 9, and pHs 7 to 10, respectively. The pH range slightly expands to pHs 6 to

10 when OHA concentration increases to $1 \times 10^{-3}$ M. These pH ranges for OHA are wider than OHA interactions with Ce(OH)$_3$ because OHA performance appears more selective to Ce$_2$(CO$_3$)$_3$ than Ce(OH)$_3$. By comparison, SHA appears equally effective for both Ce$_2$(CO$_3$)$_3$ and Ce(OH)$_3$.
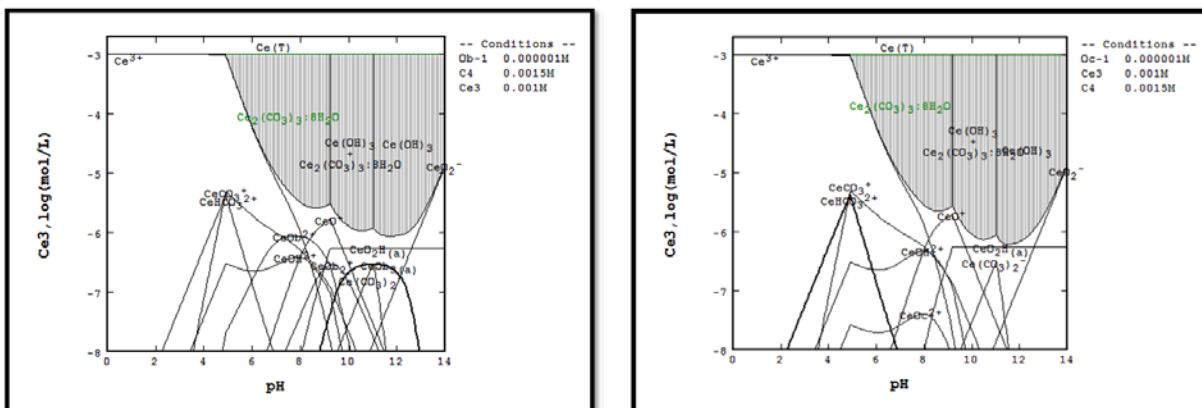


**Figure 43: Speciation Diagrams for Ce Carbonate with 1E-6M SHA (left) and OHA (right)**
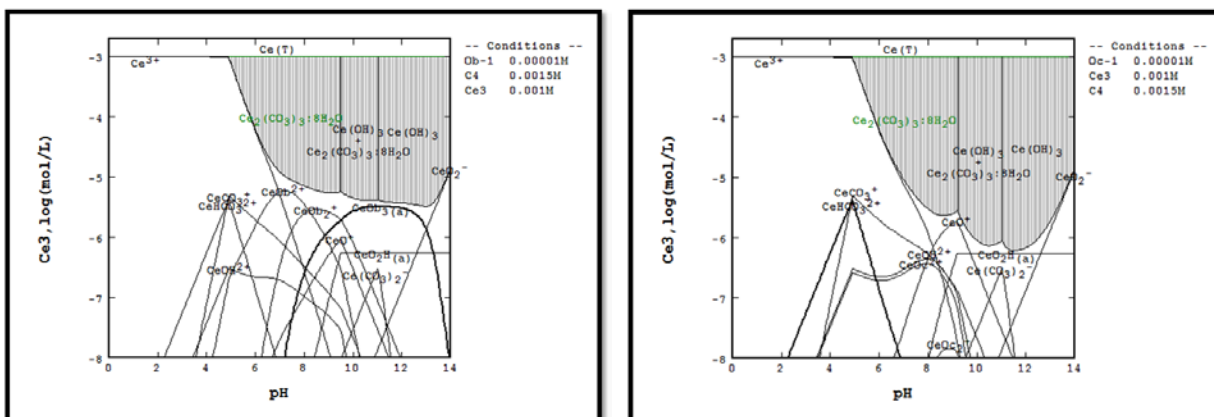


**Figure 44: Speciation Diagrams for Ce Carbonate with 1E-5M SHA (left) and OHA (right)**
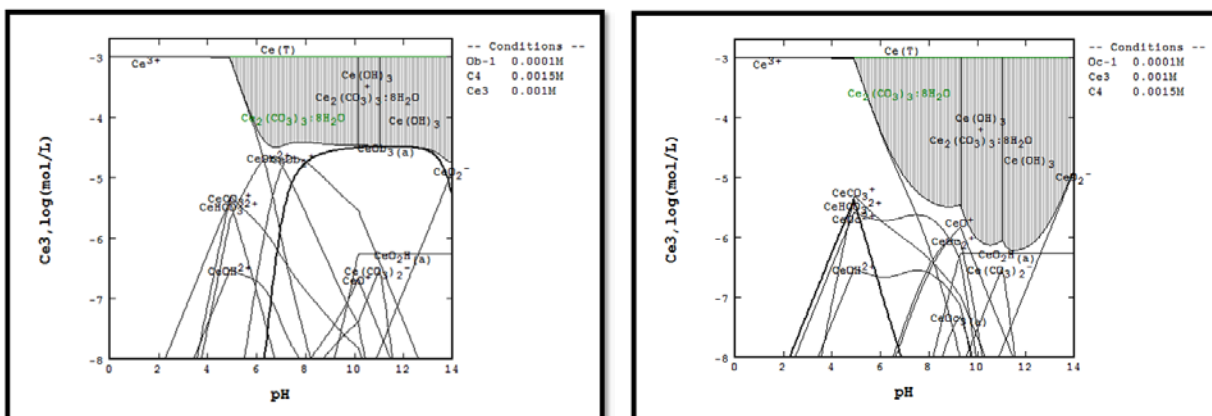
**Figure 45: Speciation diagrams for Ce carbonate with 1E-4M SHA (left) and OHA (right)**
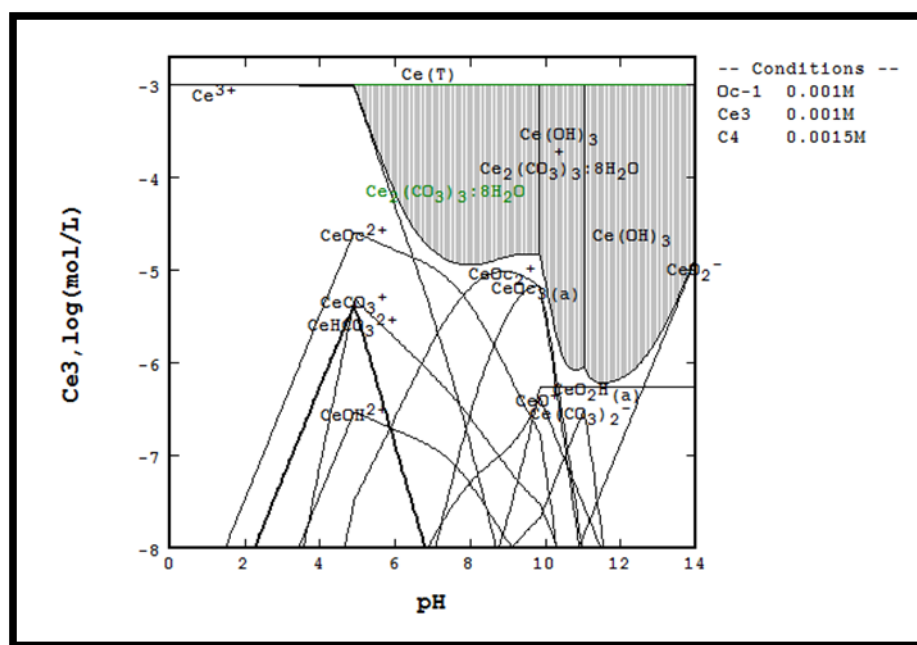


**Figure 46: Speciation Diagram for Ce Carbonate with 0.001M OHA**

As with REOs, SHA requires minimal concentrations in order to react at similar pHs as OHA. SHA adsorption for $Ce_2(CO_3)_3$ occurs in nearly the same pH range as for $Ce(OH)_3$ but extends to lower pH units, which can be due to the fact that the REC is also stable at lower pHs and therefore occurs naturally. In addition, SHA adsorption at lower pH values can be associated

with the selectivity of OHA its preference for $Ce_2(CO_3)_3$ over $Ce(OH)_3$. OHA appears more effective under moderately alkaline conditions whereas SHA reacts under all alkaline solutions. However, the most significant feature is perhaps observed with SHA. For this collector, $Ce^{3+}$ complexes to form two predominant species: $Ce(SHA)_{3(aq)}$ and $Ce(SHA)^{2+}$ with maximum concentrations near pH 11 and pH 7, respectively. $Ce(SHA)_2^+$ also develops but typically at lower concentrations, maximizing at approximately pH 9 subservient to other species. LaDouceur and Young (2015) has been examining REM flotation with SHA using Bear Lodge Property ore as a function of pH. Results reported a maximum recovery of 68% at pH 7.5 and are in congruence with the figures presented.

The other three RECs manifest behavior identical to that of Ce carbonate in the presence of SHA or OHA. For example, diagrams for Pr carbonate are presented in Figures 47-50. Comparing $1x10^{-5}$ M to Figure 25 in the absence of collector shows SHA interacting between pHs 6 and 13 whereas OHA barely reacts at pH 8. Eu carbonate also interacts with SHA in the same pH range of 6-13 while hardly reacting with OHA at pH 8 (Figures 51-55, Figure 26). Likewise, Tb carbonate reacts between pHs 6-13 but does not interact with OHA until pH 8 (Figures 56-60, Figure 27). OHA appears more selective to $Ce_2(CO_3)_3$ than $Ce(OH)_3$, resulting in wider pH ranges for the carbonate than for the oxide. SHA behaves differently in that it interacts at nearly identical pH levels for both $Ce_2(CO_3)_3$ and $Ce(OH)_3$, and thus does not exhibit selectivity to either rare earth compound. Solubility diagrams for La, Nd, and Dy carbonates illustrate similar behavior (Appendices C and D).

**Figure 47: Solubility Curves for Pr Carbonate with 1E-6M SHA (left) and OHA (right)**



**Figure 48: Solubility Curves for Pr Carbonate with 1E-5M SHA (left) and OHA (right)**



**Figure 49: Solubility Curves for Pr Carbonate with 1E-4M SHA (left) and OHA (right)**
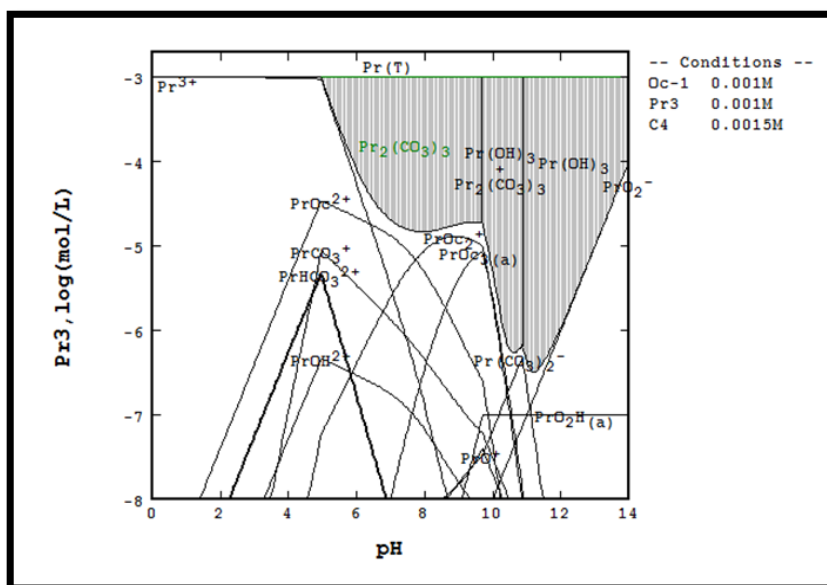
**Figure 50: Solubility Curve for Pr Carbonate with 0.001M OHA**
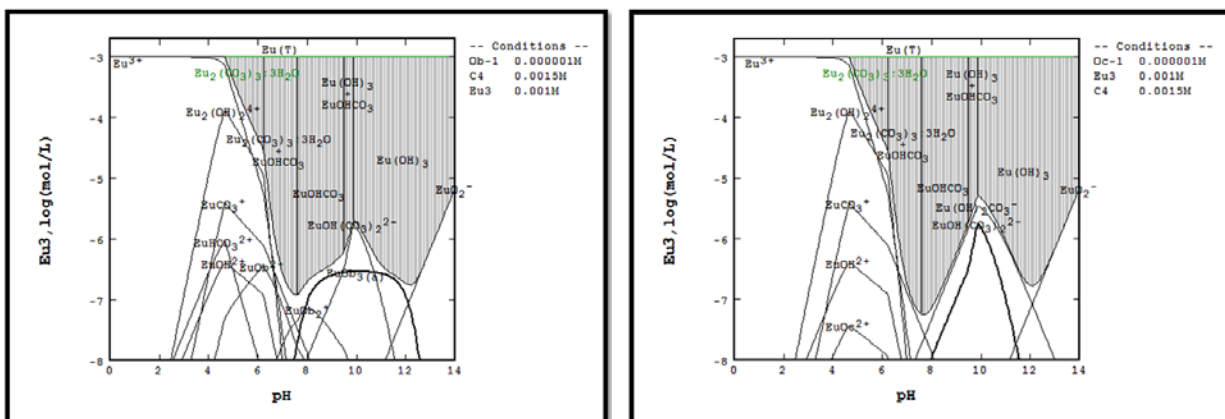


**Figure 51: Speciation Diagrams for Eu Carbonate with 1E-6M SHA (left) and OHA (right)**

**Figure 52: Speciation Diagrams for Eu Carbonate with 1E-5M SHA (left) and OHA (right)**



**Figure 53: Speciation Diagrams for Eu Carbonate with 1E-4M SHA (left) and OHA (right)**

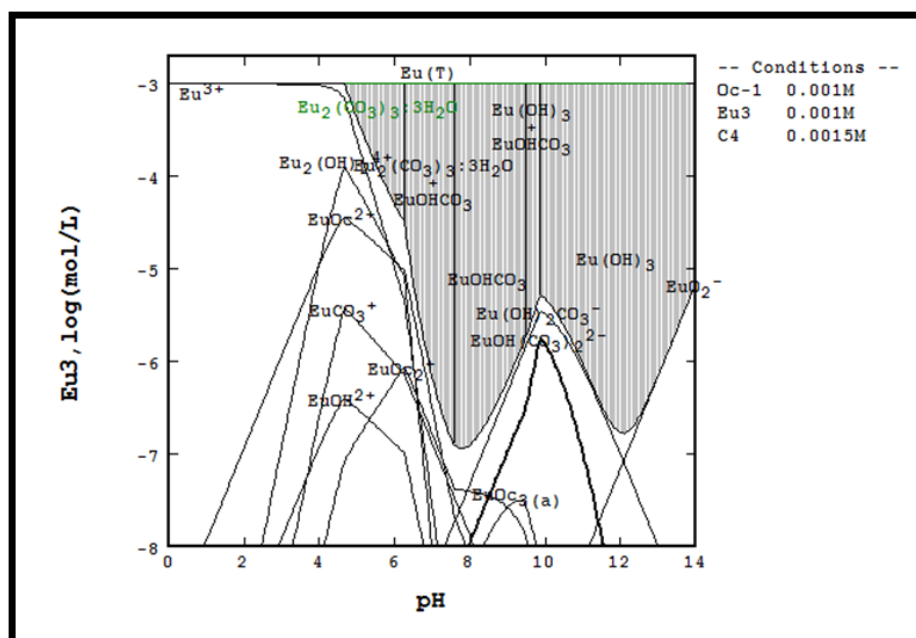**Figure 54: Speciation Diagram for Eu Carbonate with 0.001M OHA**
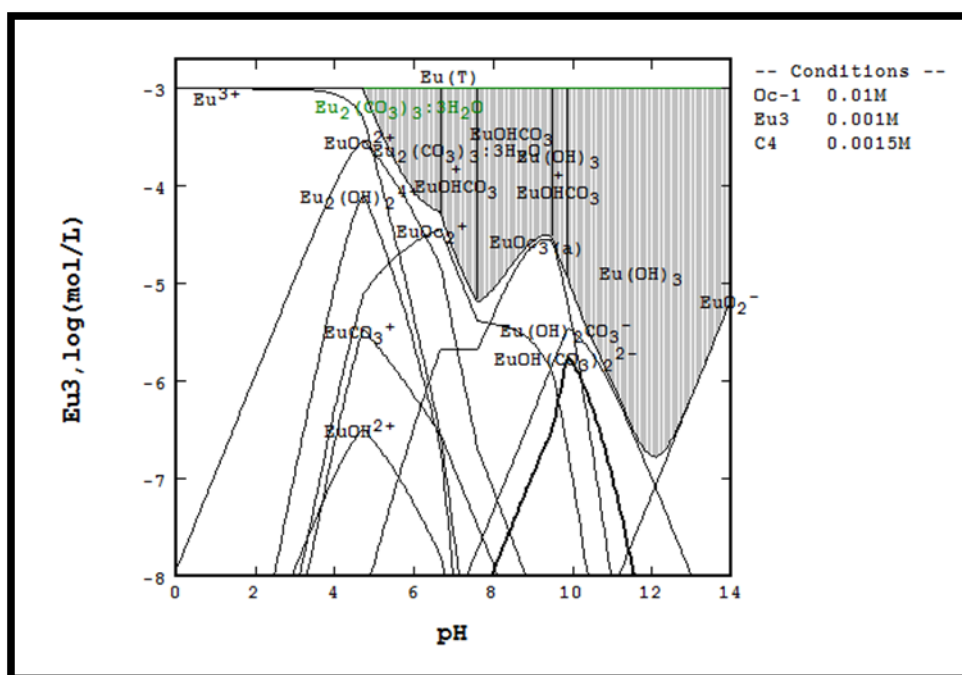


**Figure 55: Speciation Diagram for Eu carbonate with 0.01M OHA**
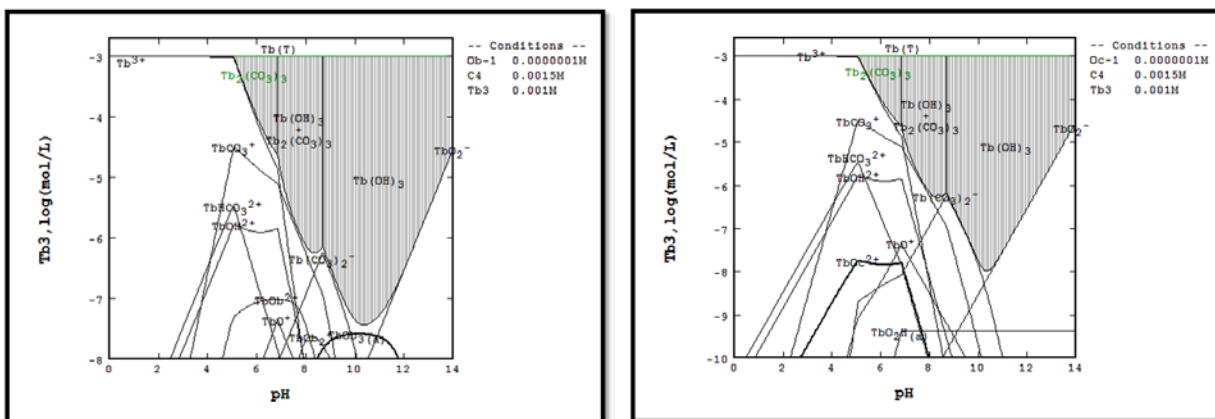
**Figure 56: Solubility Curve for Tb Carbonate with 1E-7M SHA (left) and OHA (right)**
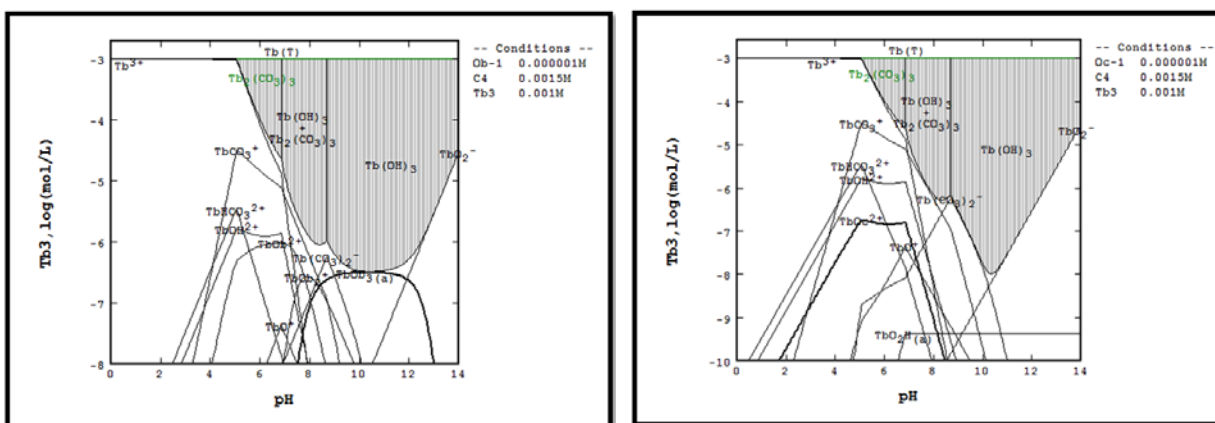


**Figure 57: Solubility Curve for Tb Carbonate with 1E-6M SHA (left) and OHA (right)**
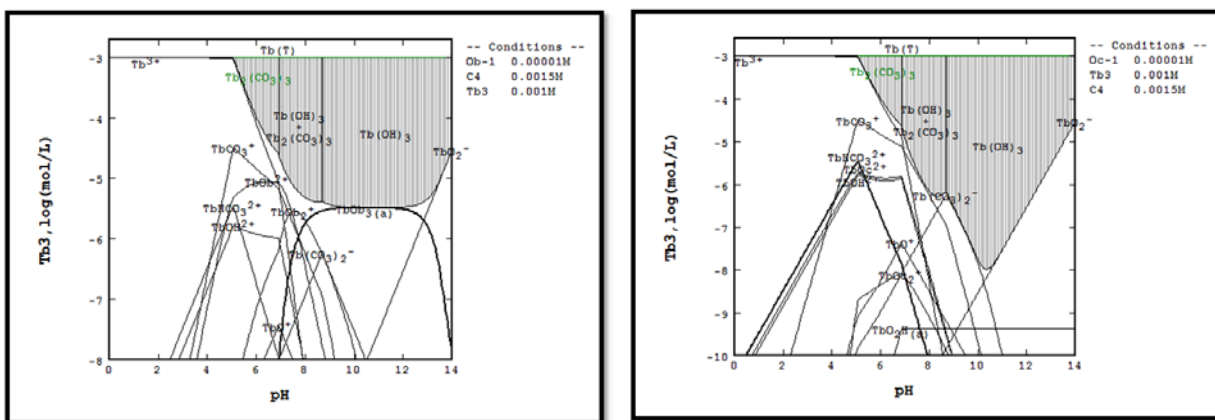


**Figure 58: Solubility curve for Tb Carbonate with 1E-5M SHA (left) and OHA (right)**
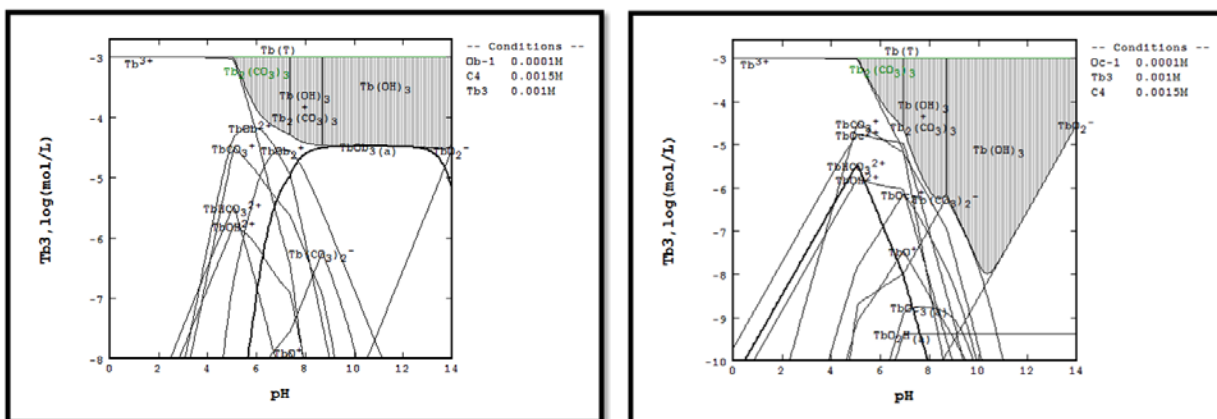
**Figure 59: Solubility Curve for Tb Carbonate with 1E-4M SHA (left) and OHA (right)**
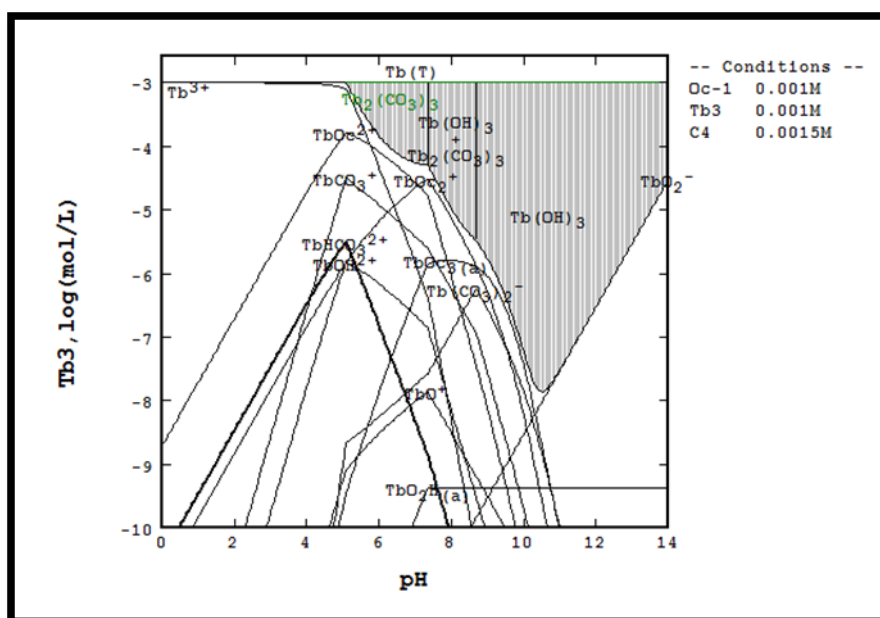


**Figure 60: Solubility Curve for Tb Carbonate with 0.001M OHA**

Solubility diagrams with SHA and OHA show that SHA adsorbs more strongly onto RECs than OHA due to its wider pH range at low concentrations. The pH ranges for SHA adsorption onto RECs are nearly identical to the ranges with REOs but extends to lower pH values due to greater stability of RECs themselves. However, SHA demonstrates a series of critical behaviors. First, the collector complexes with $RE^{3+}$ to form two predominant species:

$RE(SHA)_{3(aq)}$ and $RE(SHA)^{2+}$ which tend to yield maximum concentrations near pH 11 and pH 7, respectively. These observations are consistent with results from LaDouceur and Young (2015) which established maximum REE recovery using SHA at pH 7.5. $RE(SHA)_2^+$ is not considered predominant since it typically complexes at lower concentrations than the other species and maximizes at approximately pH 9. These findings suggest either chemisorption or physisorption induces flotation of a species similar to $RE(SHA)^{2+}$ at pH 7 (i.e. low pH), or surface precipitation at pH 11 (i.e. high pH) as $RE(SHA)_{3(ppt)}$ which is similar to $RE(SHA)_{3(aq)}$.

## 4.3.   PZC Measurements

Points of zero charge, or isoelectric points (IEPs), for the selected REOs and RECs were experimentally determined using the Stabino Titration Analyzer. Streaming potentials were first measured then converted to zeta potentials ($\zeta$) which represent solution potentials at the shear plane. Surface charge is assumed to follow zeta potential such that they are equivalent when zeta potential is zero, thereby yielding the PZC. Values were obtained by either starting at high pH and titrating with HCl, or at low pH and titrating with NaOH, since results were found to be independent of scan direction. Rare earth compounds were individually tested without collector in order to compare results to estimates calculated using StabCal software by summing charges for all ions and determining the pH where the sum was zero (i.e. the PZC). Zeta potential measurements are provided in Figures 61-64.
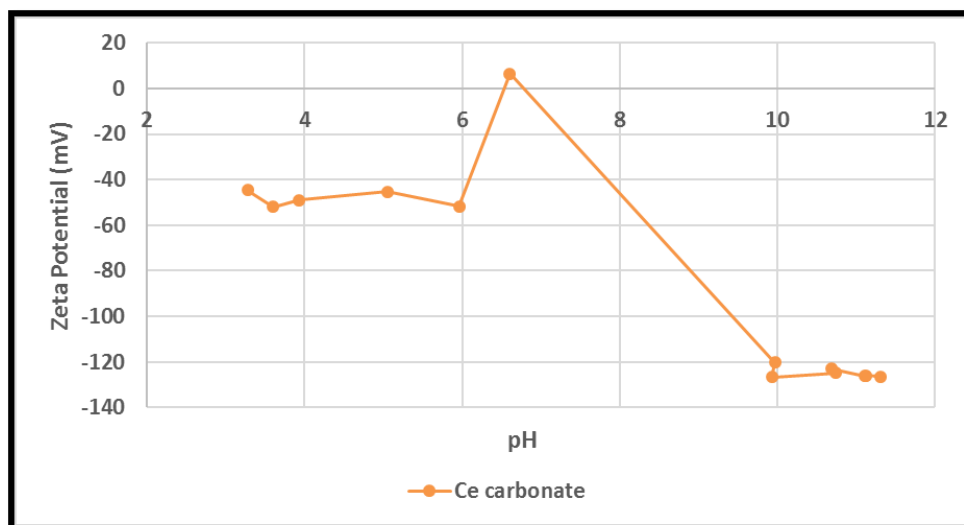
**Figure 61: Zeta Potential for Ce Carbonate Titrated with 0.1M HCl**



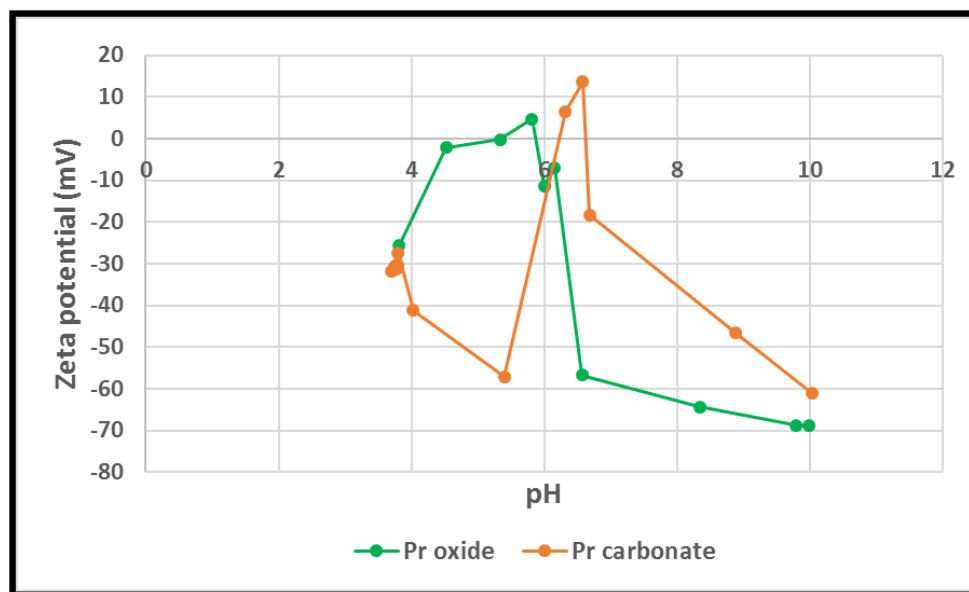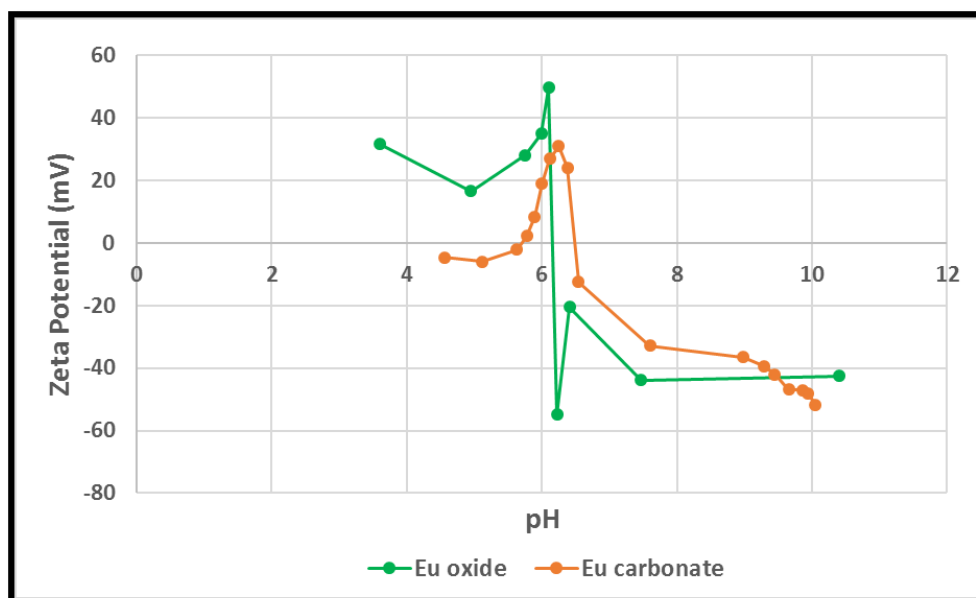**Figure 62: Zeta Potentials for Pr Oxide and Pr Carbonate Titrated with 0.1M NaOH**

**Figure 63: Zeta Potentials for Eu Oxide and Eu Carbonate Titrated with 0.1M NaOH**
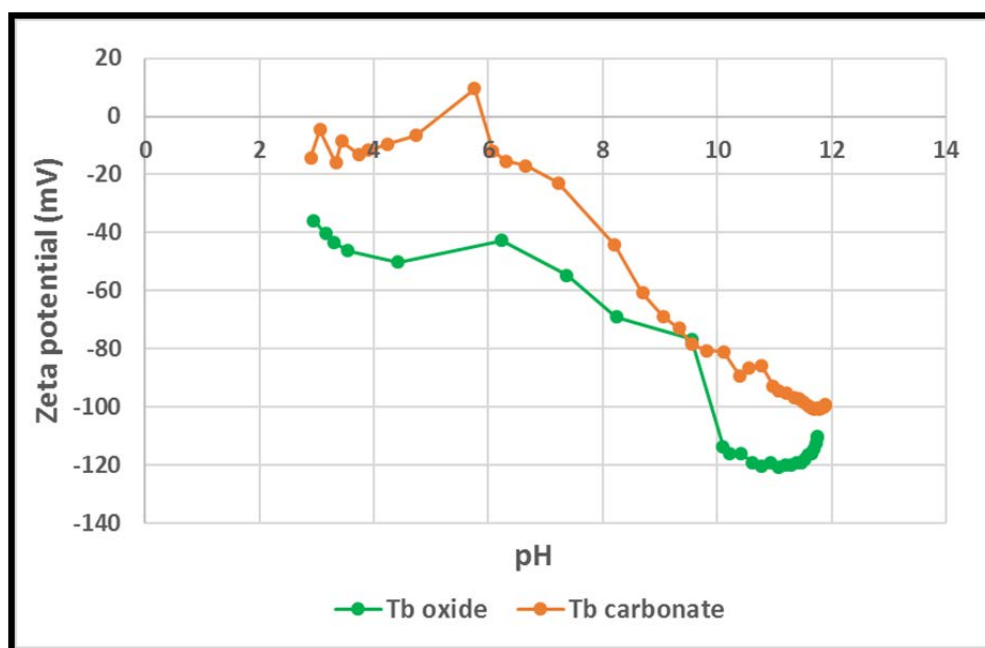


**Figure 64: Zeta Potentials for Tb Oxide and Tb Carbonate Titrated with 0.1M HCl**

Results from the Stabino instrument indicate predominantly negative zeta potentials for

the REOs and RECs of Ce, Pr, Eu, and Tb over a pH range of 12 to 3, thus denoting negative

surface charges. Most REMs exhibit charge reversal when pH decreases to approximately 6.5.

Although Ce oxide was not tested in the present work, recent experiments (Young, Downey, &

Gleason, 2017) estimated its PZC at pH 6.7 which is in excellent agreement with data from

Hattori and Masakuni (2004). Oxides of Pr and Eu yielded PZCs at pH 5.8 and 6.2, respectively.

Despite multiple runs for Tb oxide, surface charge remained negative from roughly pH 12 to pH

3 and a PZC was not established (Figure 64). By comparison, PZCs were determined for all four

RECs with Ce carbonate at pH 6.7, Pr carbonate at pH 6.6, Eu carbonate at pH 6.5, and Tb

carbonate at pH 5.9. Factors that could attribute to negative surface charge include but are not

necessarily limited to: (1) poor adsorption of $H^+$ ions to the surface, (2) preferred adsorption of

$OH^-$ ions due to formation of hydroxide complexes, and (3) presence of divalent atoms as either

oxide ($O^{2-}$) or carbonate ($CO_3^{2-}$). Table VII provides a comparison of PZC data from the graphs.

**Table VII: Stabino PZC Results for Selected REOs and RECs**

| REE | Oxide PZC | Carbonate PZC |
|---|---|---|
| Cerium | 6.7* | 6.7 |
| Praseodymium | 5.8 | 6.6 |
| Europium | 6.2 | 6.5 |
| Terbium | Always negative | 5.9 |

*From Young et al. (2017)

Negatively charged surfaces were established for all REMs under the pH conditions

examined in this study (i.e. pHs 7 to 11). Negative surface charge negates the possibility of a

physisorption mechanism occuring at the REM surface. Consequently, SHA must chemisorb at

low SHA concentrations. At higher concentrations, multilayer adsorption is present and

associated with surface precipitation. Thermodynamic modelling implies that chemisorption will

predominate at lower values near pH 7, and that surface precipitation will occur. Zhang and

Honaker (2017) reported similar findings for OHA adsorption on monazite.

### 4.3.1. Comparisons

Experimental PZCs for the four REOs and RECs are compared in Table VIII to the

estimated values determined using StabCal modelling. Overall, results from the two methods

reveal little to no similarities. StabCal calculations are 3 to 4 pH units higher than experimental

measurements for Ce and Pr, and 1 to 2 pH units higher for Eu and Tb. The factors previously

listed to account for negative surface charge can also account for lack of congruence which, in

this case, is most likely attributed to presence of divalent anions. These anions would have

influenced the ionic strength of the solution and consequently affected zeta potential. However,

REE coordination chemistry may also play a role since it is pH dependent, inhibiting the process

of attaining valid thermodynamic data and consequently resulting in inaccurate StabCal

solubility curves.

**Table VIII: Estimated and Experimental PZC Results for Selected REOs and RECs**

| REE | Calculated (StabCal) | | Experimental (Stabino) | |
|-----|---------------------|---------------------|---------------------|---------------------|
| | $PZC_{oxide}$ | $PZC_{carbonate}$ | $PZC_{oxide}$ | $PZC_{carbonate}$ |
| Ce | 8.75 | 8.75 | 6.7* | 6.7 |
| Pr | 8.75 | 8.75 | 5.8 | 6.6 |
| Eu | 8.25 | 7.25 | 6.2 | 6.5 |
| Tb | 7.75 | 7.75 | Always Negative | 5.9 |

*From Young et al. (2017)

## 4.4. Adsorption Density Studies

Adsorption density studies were performed in attempts to identify the type of adsorption

mechanism between SHA and the REM surface. Adsorption density plots were first constructed

to model the appearance of SHA onto the mineral as a function of time. Results presented in

Appendix B demonstrate strong SHA adsorption on the oxides of Ce and Pr and the carbonates

of Eu and Tb, but poor adsorption on the carbonates of Ce and Pr and oxides of Eu and Tb.

Tables in Appendix B also report adsorption density values that exceed the monolayer adsorption of approximately $3 \times 10^{-10}$ mol/cm$^2$ as predicted for SHA in ongoing research efforts. Therefore, adsorption is attributed to surface precipitation of RE(SHA)$_3$; however, surface precipitation could merely be masking other mechanisms and not necessarily excluding the occurrence of physisorption or chemisorption. In the case of Ce$_2$(CO$_3$)$_3$, SHA adsorption appeared at or below the limiting value for all times measured for pH 10. In addition, SHA may have absorbed poorly onto the oxide surfaces of Eu and Tb, but adsorption steadily improved to nearly the same values as their respective carbonates for pHs 9 and 10. Such behavior implies that SHA adsorption competed with CO$_3^{2-}$ and the oxide surface converted to a carbonate surface, as concluded by Nicholas et al. (2016). It also corroborates the solubility diagrams for the carbonates of Eu and Tb where carbonate phases are shown to be stable below pH 10 (see Figures 26 and 27).

In light of these results, SHA adsorption isotherms were attempted on Tb$_2$O$_3$ at pHs 10 and 11 in order to calculate adsorption thermodynamics that could indicate physisorption or chemisorption, if monolayer coverage was present (Appendix B). The Langmuir equation was implemented to yield thermodynamic results for the pH systems listed in Table IX.

**Table IX: Adsorption Thermodynamics for SHA in Tb Oxide at pHs 10 and 11**

|  | pH 10 | pH 11 |
|---|---|---|
| $\Delta G_{T1}$ (cal/mol) | -6825.1 | -5861.7 |
| $\Delta G_{T2}$ (cal/mol) | -8382.2 | -5468.6 |
| $\Delta G_{avg}$ (cal/mol) | -7603.6 | -5665.1 |
| $\Delta H_{ads}$ (cal/mol) | 2887.2 | -8541.3 |
| $\Delta S_{ads}$ (cal/mol-K) | 32.3 | -9.1 |

Graphs in Appendix B convey an increase in adsorption density with increasing temperature at both pH levels. In addition, $\Delta H_{ads}$ for pH 11 and $\Delta S_{ads}$ for pH 10 suggest enthalpically and entropically driven reactions, respectively. However, as previously discussed, physisorption is

generally associated with free energy values between 0 and -5 kcal/mol and sufficiently negative enthalpy values. Chemisorption processes are commonly identified with free energies more negative than -10 kcal/mol and sufficiently positive entropy values. Based on these characteristics, the data listed in Table IX is inconclusive, since the average free energies for both systems fall between -5 and -10 kcal/mol. Although thermodynamics did not establish an adsorption mechanism, experimental PZC results indicated the surface charge for $Tb_2O_3$ was always negative, suggesting that physisorption for $Tb_2O_3$ is negligible when considering the Langmuir equation, if monolayer adsorption is present.

## 5. Conclusions

Adsorption of the novel collector salicylhydroxamic acid was studied in detail on the surfaces of a select group of rare earth oxides and carbonates: Ce, Pr, Eu, and Tb. Results indicate that SHA adsorption at the REE surfaces is a function of pH, cationic size, bonding chemistry, and whether the rare earth is an oxide or carbonate.

According to results from the equilibrium studies, adsorption favored lower pH levels for all tested REOs and RECs but also depended on the REM of interest. Ce oxide manifested the strongest and fastest adsorption, but SHA adsorbed most quickly onto Pr oxide and Tb carbonate out of the trivalent REEs. Overall, oxide forms of the LREEs exhibited both stronger and faster SHA adsorption at room temperature, whereas much slower and weaker adsorption was observed for the HREOs. Conversely, SHA adsorbed most onto the HRECs, and least with the LRECs. In other words, SHA adsorption onto oxides decreases as REE ionic diameter decreases, whereas adsorption onto carbonates decreases as ionic diameter increases.

Differences noted between oxide and carbonate performances with SHA are likely due to a relation between cationic size and the size of the SHA chelate. Coordination number is suspected to increase when REEs coordinate with carbonate, thereby causing an increase in ionic diameters. As a result, the LREEs become too large to chelate with SHA, whereas the HREEs also increase in size but chelate more effectively. Therefore, stronger chelation results in stronger adsorption, which can be seen in the HRECs but not the LRECs. Furthermore, the LREOs exhibit fastest adsorption since their diameters are also close in size to the SHA chelate, as opposed to the HREOs whose sizes are substantially smaller. Additionally, LREEs possess a greater tendency to give up electrons than the HREEs, a feature associated with REE basicity, which would subsequently cause SHA to more readily adsorb onto the LREO surface.

Comparison of SHA and OHA using StabCal software revealed that SHA and OHA interact differently with REMs. Solubility diagrams illustrated that SHA is stable over a wider pH range at lower concentrations than that of OHA; however, the diagrams also indicate that OHA is more selective than SHA and tends to react at higher collector concentrations. Optimal pH conditions for flotation of REOs and RECs using OHA range between pHs 8 and 10, and occur at roughly pHs 7 and 11 for SHA according to the points of maximum concentrations of the predominant SHA complexes. These conditions are consistent with recent micro flotation studies on bastnaesite using SHA; highest recovery was reported at pH 7.5, and highest recovery in the alkaline range was reported at pH 11. Plots for RECs also showed a slightly wider pH range with SHA than the diagrams for REOs, due to the fact that RECs themselves exhibit greater stability than REOs.

Theoretical PZC estimates obtained using StabCal were then compared with experimental PZC results from the Stabino. Zeta potential measurements ranged from roughly pH 6 to pH 7, and PZCs in StabCal ranged from pH 7.25 to pH 8.75. Surface charges for all REMs were predominantly negative with very few positive signals on each run, and no PZC was detected for Tb oxide. Thus, the possibility of a physisorption mechanism is negligible given that SHA is an anionic collector. Experimental PZCs for the remaining oxides excluding Ce could be plotted on the very top left border of the solids curves depicted in the StabCal diagrams to demonstrate that they never approached minimum solubility. Similarly, experimental values for the carbonates did not plot near the point of minimum solubility but could always be plotted in the carbonate phase depicted on the StabCal diagrams and did not plot in either of the other solid regions.

Adsorption density studies revealed that adsorption densities of nearly all REOs and RECs at all pH levels exceeded the limit of monolayer adsorption, with the exception of

$Ce_2(CO_3)_3$ at pH 10. Adsorption was thus attributed to surface precipitation, although the occurrence of physisorption or chemisorption is not necessarily negligible. Results from adsorption isotherms attempted on $Tb_2O_3$ were proven to be inconclusive, since the calculated adsorption thermodynamics at both elevated and room temperatures yielded free energies of adsorption between -5 and -10 kcal/mol. However, physisorption for SHA and Tb oxide is unlikely, given that PZC results indicated a negative surface charge for Tb oxide under all pH conditions.

# 6. Recommendations and Future Work

Both XRD and Raman analyses could be performed on the REOs and RECs in this study, as well as further zeta potential research on for the REEs mentioned in Appendices A, C and D. Zeta potential results could provide a more comprehensive understanding of the rare earth PZCs and thus further insight on the interaction between SHA and REEs. Additionally, Raman spectroscopy could be performed on the samples of adsorbed SHA onto REE to detect possible surface carbonation and reaffirm surface precipitation at higher pH levels. Eliminating open air in future test work should be considered by performing studies under closed atmospheres to assess whether adsorption changes for rare-earths that adsorbed poorly with SHA. Similar studies are currently being conducted on the phosphate forms of the rare earths analyzed in this study to compare adsorption performance, since rare earth phosphates are typically prevalent in the monazite and bastnaesite ores.

Effects of rare earth coordination chemistry on adsorption should also be further investigated to confirm its role in the adsorption behavior discussed in this study. Furthermore, other novel collectors including H2O5 and sarcosinate should also be examined by procuring information on their molecular structures and analyzing their interactions with rare earth oxides, carbonates, and phosphates. Molecular models allow for closer examination of the sites within the structure and the spacing. Thus, modelling the chemical bonds and measuring head group sizes and spacing of these collectors may help specify the particular REEs to which they should adsorb more effectively. REEs with ionic diameters close in size to the chelate suggests stronger adsorption will occur. Equilibrium and adsorption density studies should then be performed to confirm or refute such modelling postulations.

# References

1. Alonso, E., Sherman, A. M., Wallington, T. J., Everson, M. P., Field, F. R., Roth, R., & Kirchain, R. E. (2012). Evaluating Rare Earth Availability: A Case with Revolutionary Demand from Clean Technologies. *Environmental Science and Technology*, 3406-3414.

2. Anderson, C. D. (2015). *Improved understanding of rare earth surface chemistry and its application to froth flotation.* Golden, CO: Colorado School of Mines.

3. Binnemans, K., Jones, P. T., Blanpain, B., Van Gerven, T., Yang, Y., Walton, A., & Buchert, M. (2013). Recycling of rare earths: a critical review. *Journal of Cleaner Production*, 1-22.

4. Caravan, P., Ellison, J. J., McMurry, T. J., & Lauffer, R. B. (1999). Gadolinium(III) Chelates as MRI Contrast Agents: Structure, Dynamics, and Applications. *Chemical Reviews*, 2293-2352.

5. Ericsson, A., Bach-Gansmo, T., Niklasson, F., & Hemmingsson, A. (1995). Combination of Gadolinium and Dysprosium Chelates as a Cellular Integrity Marker in MR Imaging. *Acta Radiologica*, 41-46.

6. Grasso, V. B. (2013). Rare Earth Elements in National Defense: Background, Oversight Issues, and Options for Congress. Washington, D.C.: Congressional Research Service.

7. Güntherodt, H., Hauser, E., & Künzi, H. (1974). The electrical resistivity of rare earth metals at high temperatures and in the liquid state. *Physics Letters*, 313-314.

8. Gupta, C., & Krishnamurthy, N. (2005). *Extractive Metallurgy of Rare Earths.* Boca Raton, FL: CRC Press.

9. Habashi, F. (2005). A short history of hydrometallurgy. *Hydrometallurgy*, 15-22.

10. Hattori, M., & Masakuni, O. (2004). Ultrasonic vibration potential and point of zero charge of some rare earth oxides in water. *Journal of Alloys and Compounds*, 408-412.

11. Haxel, G. B., Hedrick, J. B., & Orris, G. J. (2005, May 17). *Rare Earth Elements - Critical Resources for High Technology*. Retrieved from U.S. Geological Survey : https://pubs.usgs.gov/fs/2002/fs087-02

12. Herrera-Urbina, R., Pradip, & Fuerstenau, D. (2013). Electrophoretic mobility and computations of solid-aqueous solution equilibria for the bastnaesite-H2O system. *Minerals & Metallurgical Processing*, 18-23.

13. Huang, H. H., Twidwell, L. G., & Young, C. A. (2005). *Point of Zero Charge (PZC) and Double Layer Adsorption - An Equilibrium Calculation Approach.* Butte, MT.

14. Jamasmie, C. (2015, August 26). *Molycorp shuts down Mountain Pass rare earth plant.* Retrieved from MINING.com: http://www.mining.com/molycorp-shuts-down-mountain-pass-rare-earth-plant/

15. Jensen, J., & Mackintosh, A. R. (1991). *Rare Earth Magnetism: Structures and Excitations.* Oxford: Clarendon Press.

16. Kawabe, I. (1992, August 31). Lanthanide tetrad effect in the Ln3+ ionic radii and refined spin-pairing energy theory. *Geochemical Journal, 26*, 309-335.

17. Kim, K., & Osseo-Asare. (2012). Aqeous stability of thorium and rare earth metals in monazite hydrometallurgy: Eh–pH diagrams for the systems Th–, Ce–, La–, Nd– (PO4)–(SO4)–H2O at 25 °C. *Hydrometallurgy*, 67-78.

18. Kulprathipanja, S. (1974, July). *Some Properties of Some Rare-Earth and Transition Metal Dihydroxycarboxylates.* Dissertation, Iowa State University of Science and Technology, Department of Chemistry, Ames.

19. LaDouceur, R., & Young, C. (2015). Modeling and Optimization of Rare Earth Flotation. *SME Annual Conference and Expo.* Denver, CO, USA.

20. Liu, G., Wu, H., Liu, J., Shi, X., & Liu, G. (1989). Stability constants of compound of rare earth with hydroxamic acid. *Journal of Inorganic Chemistry*.

21. Liu, S. H. (1960). *Magnetic properties of rare earth metals.* Iowa State University, Department of Physics. Ann Arbor: University Microfilms, Inc.

22. Long, K. R., Van Gosen, B. S., Foley, N. K., & Cordier, D. (2010). *The principal rare earth elements deposits of the United States—A summary of domestic deposits and a global perspective.* Retrieved from U.S. Geological Survey Scientific Investigations Report 2010-5220: https://pubs.usgs.gov/sir/2010/5220/

23. Natarajan, R., & Fuerstenau, D. W. (1983). Adsorption and flotation behavior of manganese dioxide in the presence of octyl hydroxamate. *International Journal of Mineral Processing*, 139-153.

24. Nicholas, W., LaDouceur, R., Das, A., & Young, C. (2016). Adsorption of salicylhydroxamic acid on the oxides of selected rare earth elements. *Proc. SME Annual Conference and Expo*, (pp. Pre-print No. 16-167). Phoenix, AZ, USA.

25. Parks, G. A. (1965). The isoeletric points of solid oxides, solid hydroxides, and aqueous hydroxo complex systems. *Chemical Reviews*, 177-198.

26. Pavez, O., Brandao, P., & Peres, A. (1996). Adsorption of oleate and octyl-hydroxamate on to rare-earths minerals. *Minerals Engineering*, 357-366.

27. Pradip, & Fuerstenau, D. W. (1983). The adsorption of hydroxamate on semi-soluble minerals, part I: adsorption on barite, calcite, and bastnaesite. *Colloids Surfaces*, 103-119.

28. Pradip, & Fuerstenau, D. W. (1991). The role of inorganic and organic reagents in the flotation separation of rare-earth ores. *International Journal of Mineral Processing*, 1-22.

29. Shannon, R. (1976). Revised effective ionic radii and systematic studies of interatomic distances in halides and chalcogenides. 751-767.

30. *Stabino®.* (2013). Meerbusch, Germany: Particle Metrix GmbH.

31. Thiel, C. W. (2003). *Energies of rare-earth ion states relative to host bands in optical materials from electron photoemission spectroscopy.* Dissertation, Montana State University, Department of Physics, Bozeman.

32. Wills, B. A. (2006). *Wills' Mineral Processing Technology.* Oxford, UK: Elsevier Ltd.

33. Xia, L., Hart, B., Chelgani, S., & Douglas, K. (2014). Hydroxamate collectors for rare earth minerals flotation. *Conference of Metallurgists Proceedings.* Vancouver, Canada: Canadian Institute of Mining, Metallurgy and Petroleum.

34. Yamin, L. J., Ponce, C. A., Estrada, M. R., & Vert, F. T. (1996). Protonation and deprotonation of hydroxamic acids. An MO ib initio study. *Journal of Molecular Structure*, 109-117.

35. Young, C., Downey, J., & Gleason, B. (2017, January). Task 004 - Recovery of Rare Earth Elements with Advanced Processing Technologies. Aberdeen, MD, USA.

36. Zhang, W., & Honaker, R. (2017). *Adsorption of Octanohydroxamic Acid on Monazite Surfaces.* University of Kentucky, Department of Mining Engineering, Lexington.

37. Zhao, G., Zhong, H., Qiu, X., Wang, S., Gao, Y., Dai, Z., . . . Liu, G. (2013). The DFT study of cyclohexyl hydroxamic acid as a collector in scheelite flotation. *Minerals Engineering*, 54-60.

## APPENDIX A: REE Equilibrium Studies

### Lanthanum (La)
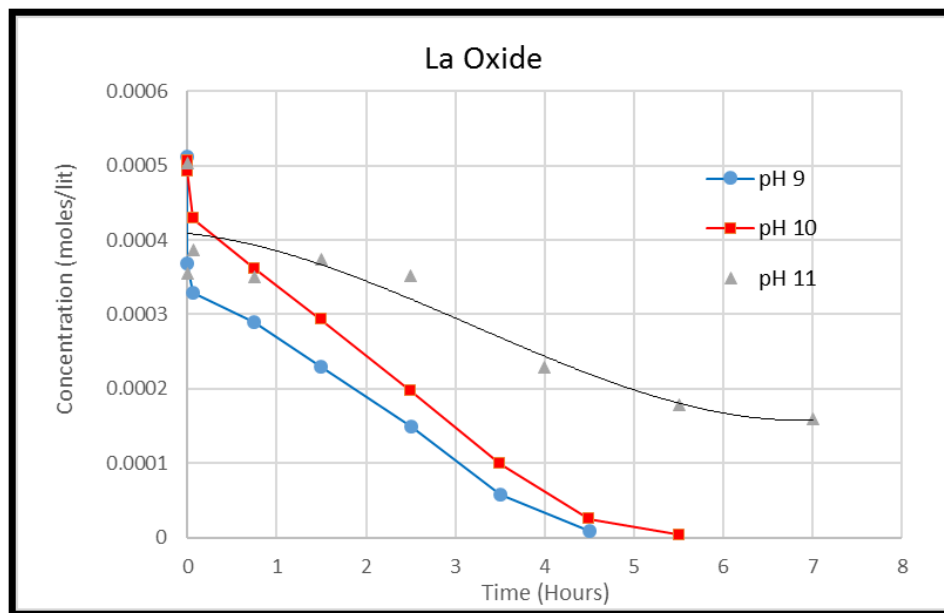


**Figure 65: Equilibrium Concentrations of SHA in La Oxide for pHs 9,10, and 11 at 20°C**
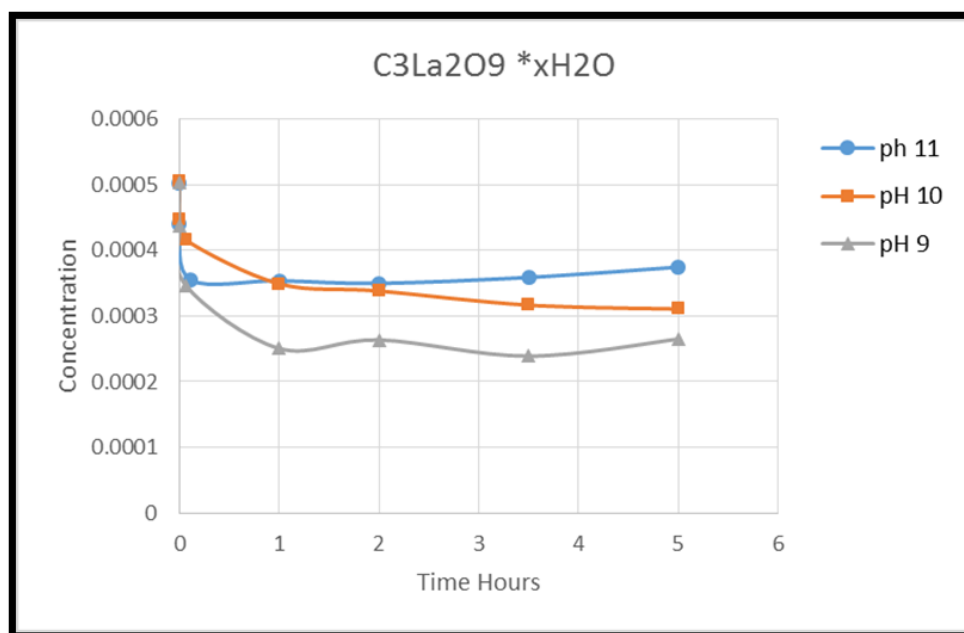


**Figure 66: Equilibrium Concentrations of SHA in La Carbonate for pHs 9, 10, and 11 at 20°C**

## Neodymium (Nd)
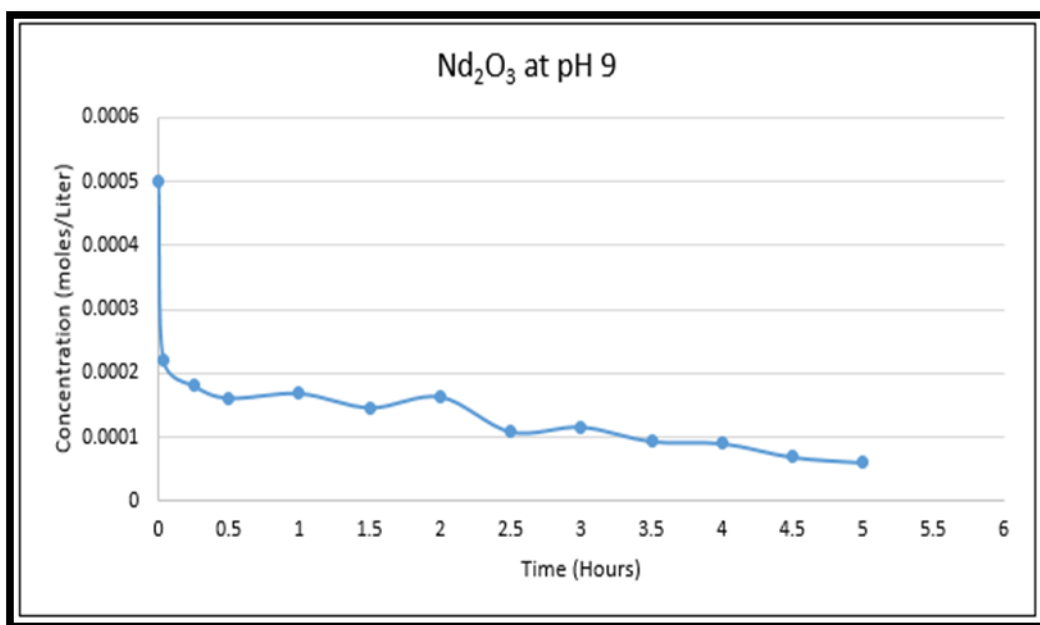


**Figure 67: Equilibrium Concentration of SHA in Nd Oxide for pH 9 at 20°C**
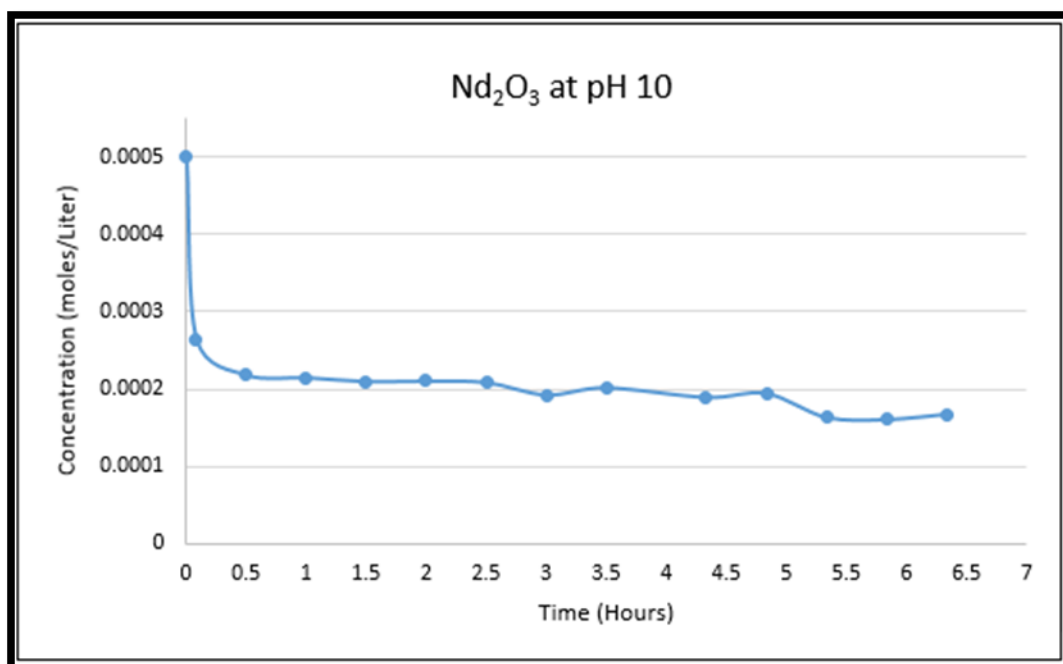


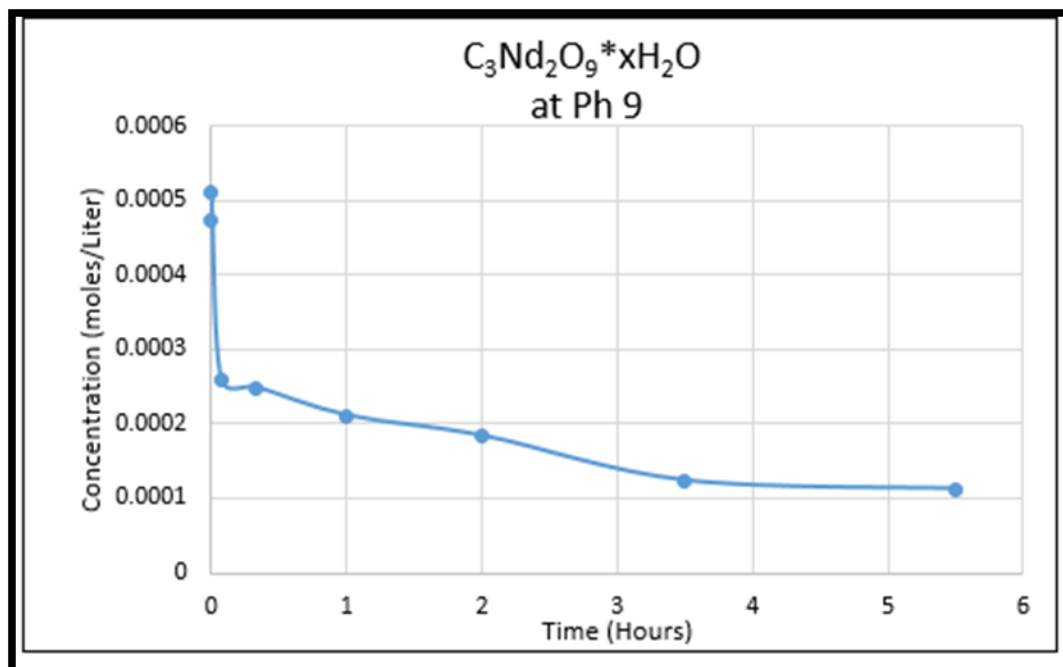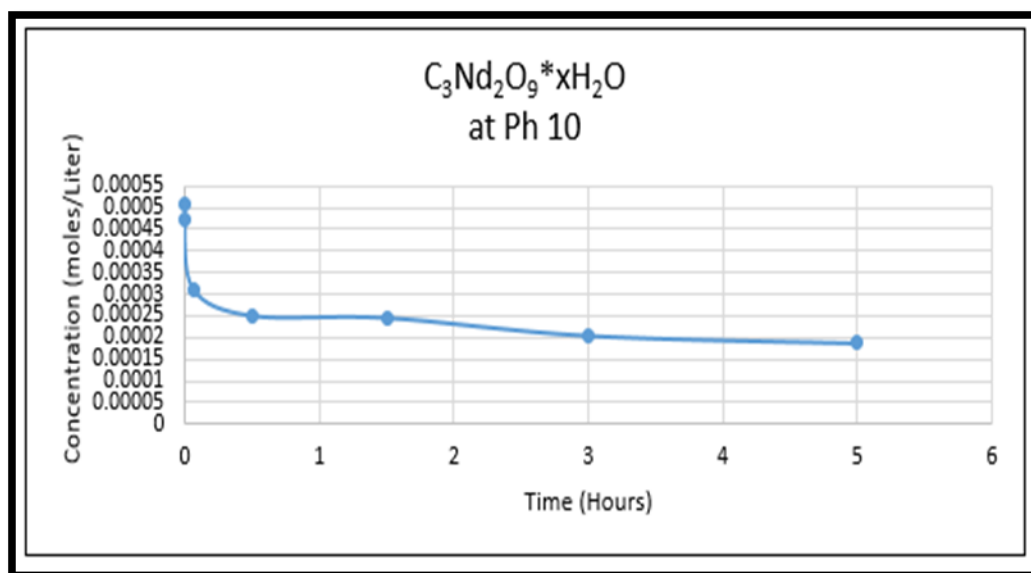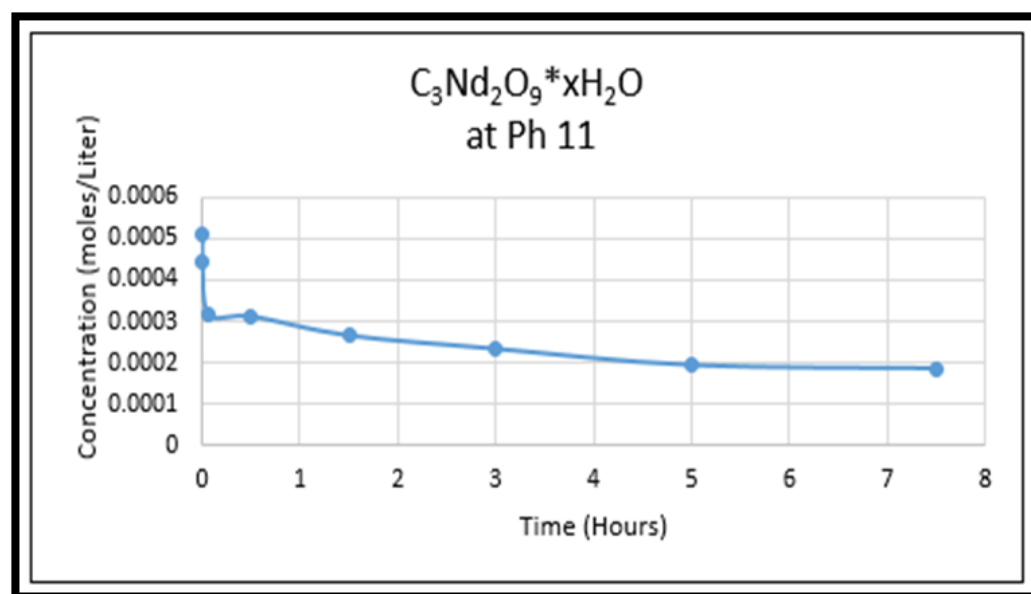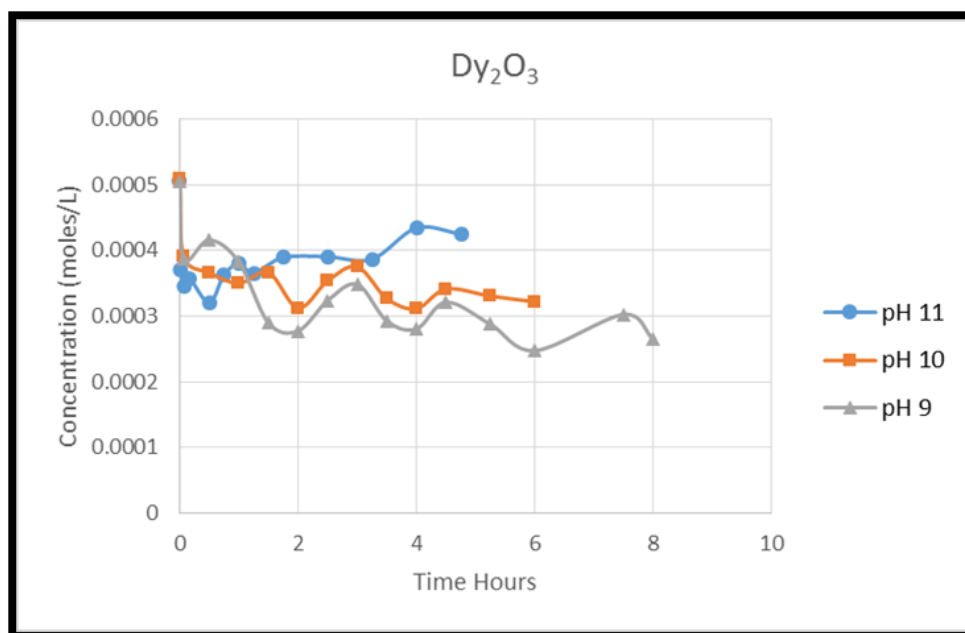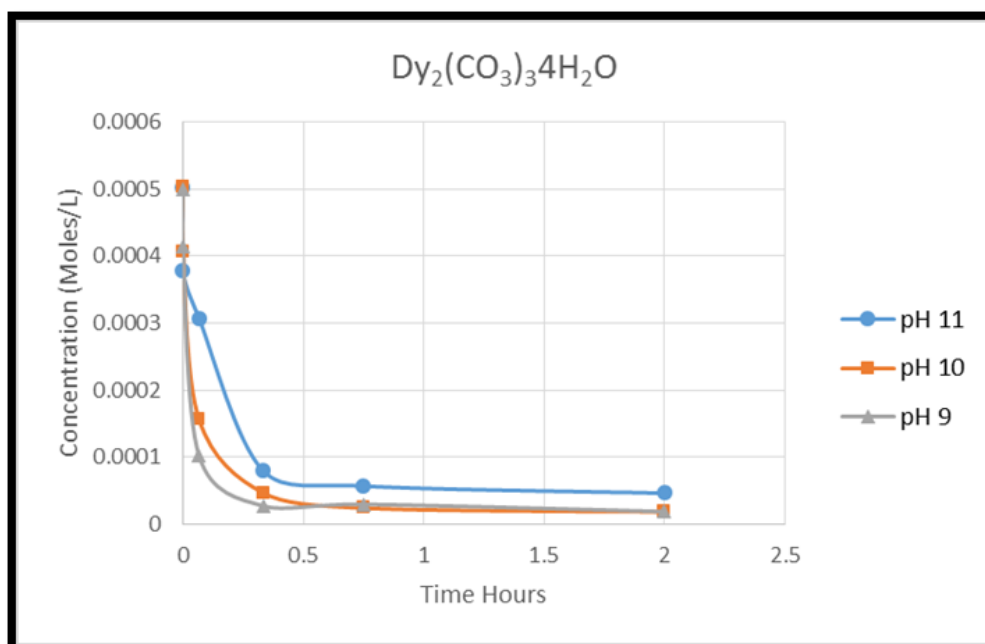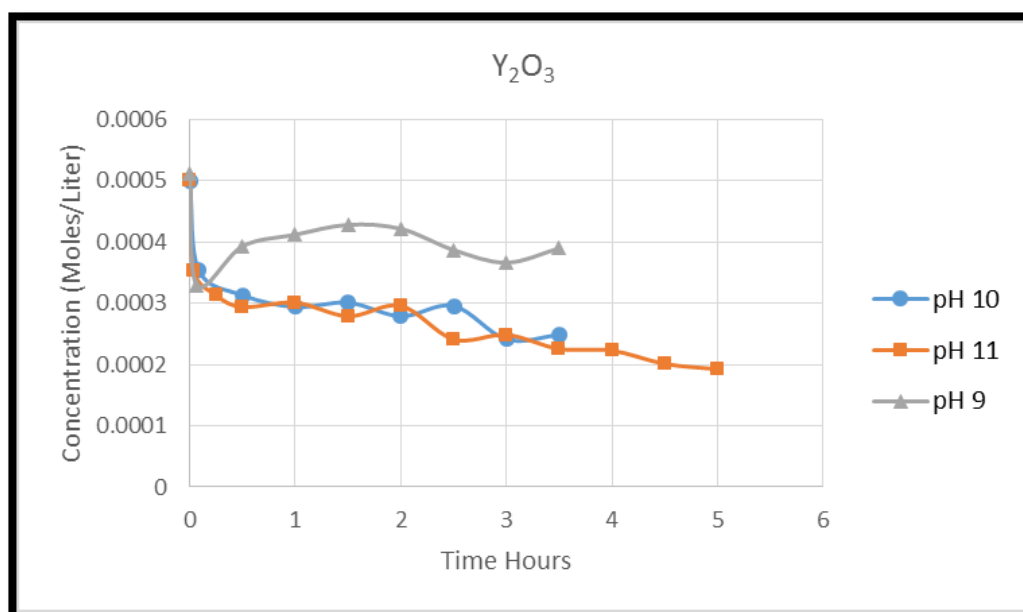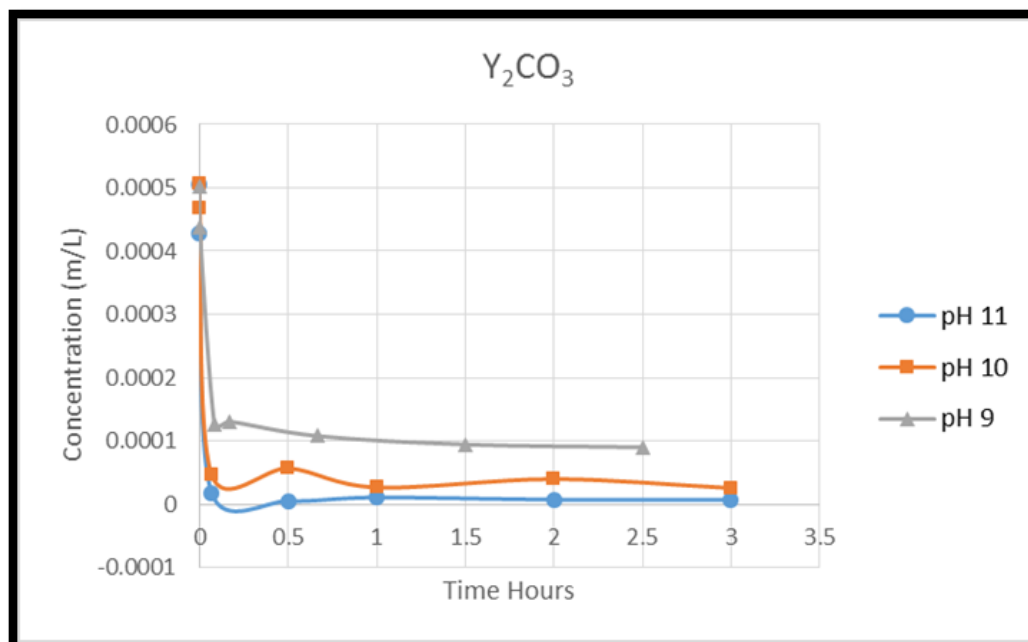**Figure 68: Equilibrium Concentration of SHA in Nd Oxide for pH 10 at 20°C**
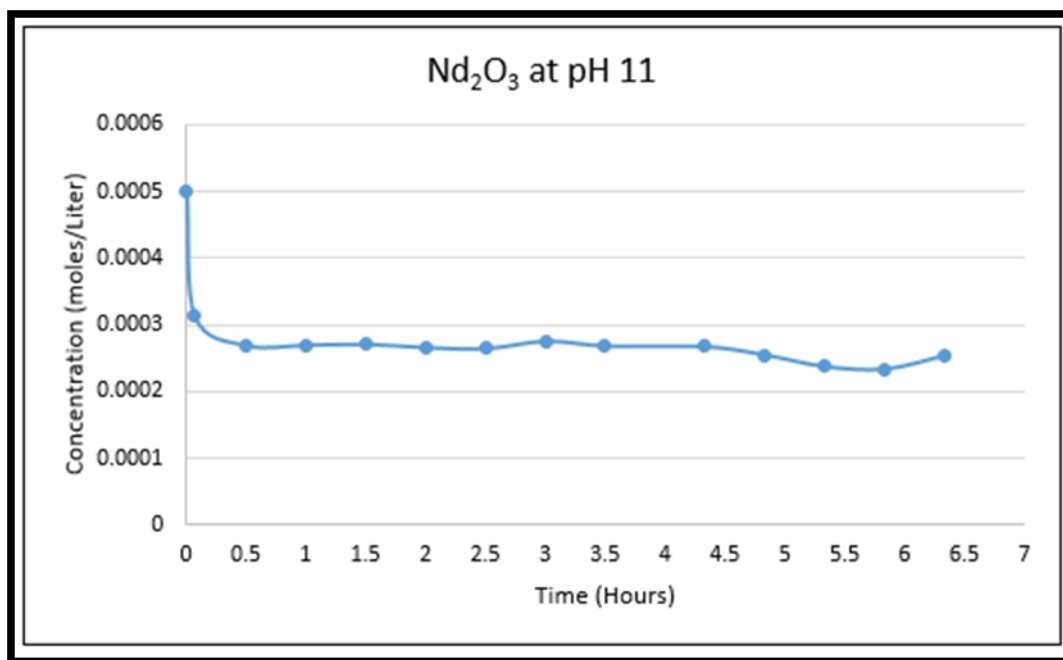
**Figure 69: Equilibrium Concentration of SHA in Nd Oxide for pH 11 at 20°C**



**Figure 70: Equilibrium Concentration of SHA in Nd Carbonate for pH 9 at 20°C**

**Figure 71: Equilibrium Concentration of SHA in Nd Carbonate for pH 10 at 20°C**



**Figure 72: Equilibrium Concentration of SHA in Nd Carbonate for pH 11 at 20°C**

## Dysprosium (Dy)



**Figure 73: Equilibrium Concentrations of SHA in Dy Oxide for pHs 9,10, and 11 at 20°C**



**Figure 74: Equilibrium Concentrations of SHA in Dy Carbonate for pHs 9, 10, and 11 at 20°C**

# Yttrium (Y)



**Figure 75: Equilibrium Concentrations of SHA in Y Oxide for pHs 9, 10, and 11 at 20°C**



**Figure 76: Equilibrium Concentrations of SHA in Y Carbonate for pHs 9, 10, and 11 at 20°C**

# APPENDIX B: REE Adsorption Density Studies

## Cerium (Ce)

**Table X: Concentration and Adsorption Density Values for SHA in Ce Oxide**

| | Cerium Oxide, 20°C | | | | | |
|---|---|---|---|---|---|---|
| | pH 9 | | pH 10 | | pH 11 | |
| Time (hrs) | Conc. (M) | $\Gamma$ (mol/cm$^2$) | Conc. (M) | $\Gamma$ (mol/cm$^2$) | Conc. (M) | $\Gamma$ (mol/cm$^2$) |
| 0.00 | 0.000387277 | 1.87871E-10 | 0.000348430 | 2.52617E-10 | 0.000372707 | 2.12155E-10 |
| 0.05 | 0.000156544 | 5.72426E-10 | 0.000163777 | 5.60372E-10 | 0.000264881 | 3.91864E-10 |
| 0.25 | 0.000111437 | 6.47605E-10 | 8.06117E-05 | 6.98981E-10 | 9.64698E-05 | 6.72550E-10 |
| 0.50 | 9.64301E-05 | 6.72616E-10 | 4.65779E-05 | 7.55704E-10 | 7.53285E-05 | 7.07786E-10 |
| 1.00 | 8.18773E-05 | 6.96871E-10 | 2.50485E-05 | 7.91586E-10 | 3.65210E-05 | 7.72465E-10 |
| 2.00 | 6.81447E-05 | 7.19759E-10 | | | | |
| 3.00 | 5.49347E-05 | 7.41775E-10 | | | | |

**Table XI: Concentration and Adsorption Density Values for SHA in Ce Carbonate**

| | Cerium Carbonate, 20°C | | | | | |
|---|---|---|---|---|---|---|
| | pH 9 | | pH 10 | | pH 11 | |
| Time (hrs) | Conc. (M) | $\Gamma$ (mol/cm$^2$) | Conc. (M) | $\Gamma$ (mol/cm$^2$) | Conc. (M) | $\Gamma$ (mol/cm$^2$) |
| 0.0 | 0.000383474 | 1.80941E-10 | 0.000307263 | 2.99281E-10 | 0.000469907 | 4.67278E-11 |
| 0.5 | 0.000344006 | 2.42227E-10 | 0.000292124 | 3.22789E-10 | 0.000450052 | 7.75584E-11 |
| 1.0 | 0.000363343 | 2.12200E-10 | 0.000291308 | 3.24056E-10 | 0.000475824 | 3.75401E-11 |
| 1.5 | 0.000349103 | 2.34312E-10 | 0.000292867 | 3.21635E-10 | 0.000459451 | 6.29647E-11 |
| 2.0 | 0.000323986 | 2.73313E-10 | 0.000289282 | 3.27202E-10 | 0.000442739 | 8.89145E-11 |
| 2.5 | 0.000328937 | 2.65626E-10 | 0.000289584 | 3.26733E-10 | 0.000452918 | 7.31090E-11 |
| 3.0 | 0.000321667 | 2.76915E-10 | 0.000294807 | 3.18622E-10 | 0.000446697 | 8.27694E-11 |
| 3.5 | 0.000319403 | 2.80430E-10 | 0.000297846 | 3.13904E-10 | 0.000446385 | 8.32534E-11 |
| 4.0 | 0.000336342 | 2.54127E-10 | | | 0.000422444 | 1.20428E-10 |
| 4.5 | 0.000314718 | 2.87704E-10 | | | 0.000435909 | 9.95203E-11 |
| 5.0 | 0.000327262 | 2.68226E-10 | | | 0.000446752 | 8.26831E-11 |
| 5.5 | 0.000315047 | 2.87194E-10 | | | 0.000421807 | 1.21418E-10 |
| 6.0 | 0.000322319 | 2.75902E-10 | | | 0.000414802 | 1.32294E-10 |
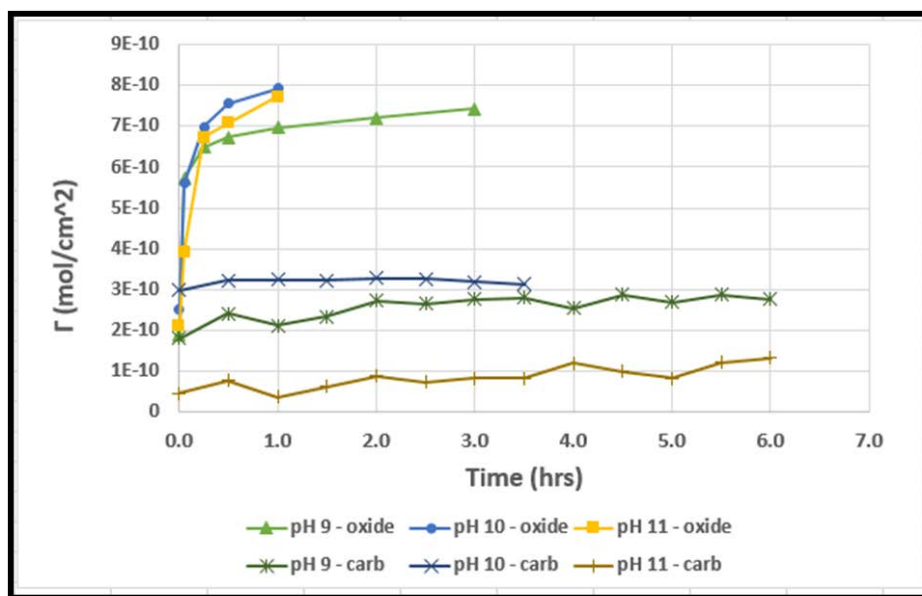
**Figure 77: Adsorption Densities of SHA in Ce Oxide and Carbonate for pHs 9, 10, and 11 at 20°C**

## Praseodymium (Pr)

**Table XII: Concentration and Adsorption Density Values for SHA in Pr Oxide**

| | Praseodymium Oxide, 20°C | | | | | |
|---|---|---|---|---|---|---|
| | pH 9 | | pH 10 | | pH 11 | |
| Time (hrs) | Conc. (M) | Γ (mol/cm²) | Conc. (M) | Γ (mol/cm²) | Conc. (M) | Γ (mol/cm²) |
| 0.00 | 5.00E-04 | 0.00000000 | 5.57E-04 | 1.8911E-10 | 0.00053662 | 5.4885E-12 |
| 0.05 | 0.000479167 | 2.9762E-10 | 0.000481611 | 1.2627E-09 | 0.00047987 | 8.1613E-10 |
| 0.25 | 0.000244815 | 3.6455E-09 | 0.000373995 | 2.8001E-09 | 0.00039344 | 2.0509E-09 |
| 0.50 | 0.00010003 | 5.7139E-09 | 0.000285744 | 4.0608E-09 | 0.00030567 | 3.3047E-09 |
| 0.75 | 4.62027E-05 | 6.4828E-09 | 0.00021835 | 5.0236E-09 | 0.0002577 | 3.9901E-09 |
| 1.00 | | | 0.000187324 | 5.4668E-09 | 0.00020287 | 4.7733E-09 |
| 1.25 | | | 0.000134698 | 6.2186E-09 | 0.00018637 | 5.009E-09 |
| 1.50 | | | 0.000150968 | 5.9862E-09 | 0.00016999 | 5.2429E-09 |

**Table XIII: Concentration and Adsorption Density Values for SHA in Pr Carbonate**

| | pH 9 | | pH 10 | | pH 11 | |
|---|---|---|---|---|---|---|
| **Praseodymium Carbonate, 20°C** | | | | | | |
| Time (hrs) | Conc. (M) | $\Gamma$ (mol/cm$^2$) | Conc. (M) | $\Gamma$ (mol/cm$^2$) | Conc. (M) | $\Gamma$ (mol/cm$^2$) |
| 0.00 | 0.000520439 | 5.3714E-11 | 5.00E-04 | 0 | 5.00E-04 | 0 |
| 0.25 | 0.000162199 | 2.0663E-09 | 0.000227404 | 1.5314E-09 | 0.00042176 | 4.3955E-10 |
| 0.50 | 0.000173815 | 2.001E-09 | 0.000184299 | 1.7736E-09 | 0.00040105 | 5.559E-10 |
| 0.75 | 0.000156332 | 2.0993E-09 | 0.000200909 | 1.6803E-09 | 0.00035505 | 8.1433E-10 |
| 1.00 | | | | | 0.0003632 | 7.6853E-10 |
| 1.25 | | | | | 0.00038418 | 6.5065E-10 |
| 1.50 | | | | | 0.00037625 | 6.9524E-10 |
| 1.75 | | | | | 0.00034185 | 8.8847E-10 |
| 2.00 | | | | | 0.00034397 | 8.7659E-10 |
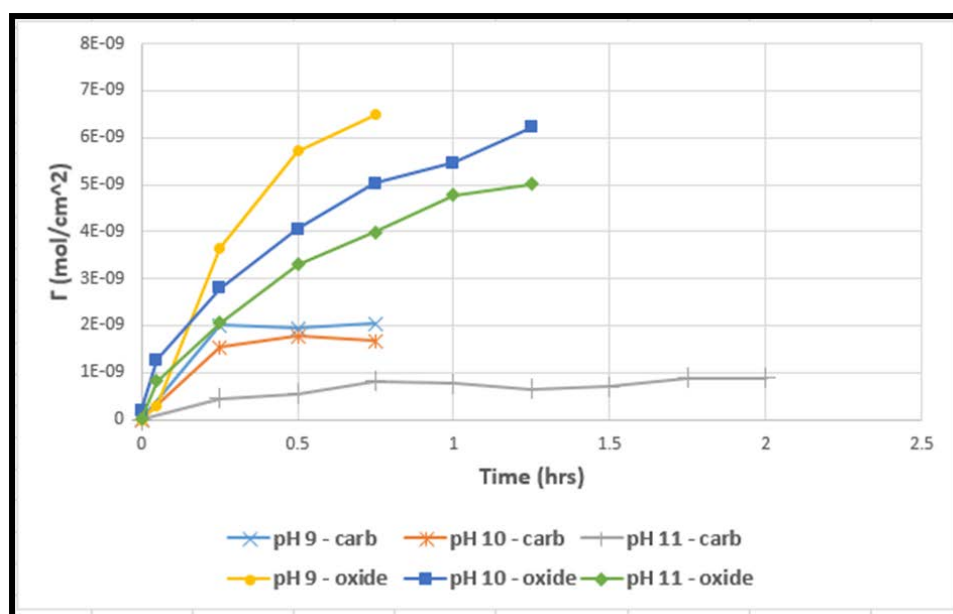


**Figure 78: Adsorption Densities of SHA in Pr Oxide and Carbonate for pHs 9, 10, and 11 at 20°C**

# Europium (Eu)

**Table XIV: Concentration and Adsorption Density Values for SHA in Eu Oxide**

| | pH 9 | | pH 10 | | pH 11 | |
|---|---|---|---|---|---|---|
| Time (hrs) | Conc. (M) | $\Gamma$ (mol/cm$^2$) | Conc. (M) | $\Gamma$ (mol/cm$^2$) | Conc. (M) | $\Gamma$ (mol/cm$^2$) |
| 0.00 | 0.00048966 | 4.79947E-11 | 0.00049916 | 8.74378E-11 | 0.000465925 | 1.58120E-10 |
| 0.05 | 0.00049173 | 3.83706E-11 | 0.00049138 | 1.23532E-10 | 0.000463075 | 1.71348E-10 |
| 0.25 | 0.00043813 | 2.87102E-10 | 0.00049687 | 9.80396E-11 | 0.000426531 | 3.40922E-10 |
| 0.50 | 0.00039304 | 4.96346E-10 | 0.00047504 | 1.99337E-10 | 0.000432175 | 3.14731E-10 |
| 1.00 | 0.00039541 | 4.85339E-10 | 0.00051775 | 1.15629E-12 | 0.000430451 | 3.22735E-10 |
| 1.50 | 0.00038655 | 5.26447E-10 | 0.00048431 | 1.56357E-10 | 0.000442798 | 2.65437E-10 |
| 2.00 | 0.00036564 | 6.23498E-10 | 0.00043949 | 3.64315E-10 | 0.000409843 | 4.18361E-10 |
| 2.50 | 0.00035221 | 6.85796E-10 | 0.00045344 | 2.99573E-10 | 0.000410277 | 4.16350E-10 |
| 3.00 | 0.00038302 | 5.42846E-10 | 0.00043949 | 3.64315E-10 | 0.000434939 | 3.01908E-10 |
| 3.50 | 0.00035900 | 6.54312E-10 | 0.00045122 | 3.09867E-10 | 0.000452897 | 2.18574E-10 |
| 4.00 | 0.00031736 | 8.47534E-10 | 0.00046202 | 2.59749E-10 | 0.000387219 | 5.23346E-10 |
| 4.50 | 0.00033142 | 7.82260E-10 | 0.00043907 | 3.66257E-10 | 0.000365820 | 6.22646E-10 |
| 5.00 | 0.00025893 | 1.11867E-09 | 0.00039548 | 5.68530E-10 | 0.000365371 | 6.24727E-10 |
| 5.50 | 0.00024786 | 1.17002E-09 | 0.00037103 | 6.82008E-10 | 0.000337883 | 7.52285E-10 |
| 6.00 | 0.00024502 | 1.18320E-09 | 0.00035488 | 7.56933E-10 | 0.000359008 | 6.54256E-10 |

**Table XV: Concentration and Adsorption Density Values for SHA in Pr Carbonate**

| | pH 9 | | pH 10 | | pH 11 | |
|---|---|---|---|---|---|---|
| Time (hrs) | Conc. (M) | $\Gamma$ (mol/cm$^2$) | Conc. (M) | $\Gamma$ (mol/cm$^2$) | Conc. (M) | $\Gamma$ (mol/cm$^2$) |
| 0.00 | 0.00033812 | 3.54617E-10 | 0.00033712 | 3.56805E-10 | 0.000375472 | 2.72789E-10 |
| 0.05 | 0.00025275 | 5.41632E-10 | 0.00026085 | 5.23871E-10 | 0.000308606 | 4.19264E-10 |
| 0.50 | 0.00011363 | 8.46372E-10 | 0.00012119 | 8.29824E-10 | 0.000202758 | 6.51132E-10 |
| 1.00 | 0.00011618 | 8.40788E-10 | 0.00011580 | 8.41619E-10 | 0.000186686 | 6.86339E-10 |
| 1.50 | 0.00013171 | 8.06774E-10 | 0.00013439 | 8.00896E-10 | 0.000196536 | 6.64762E-10 |
| 2.00 | 0.00013837 | 7.92178E-10 | 0.00013386 | 8.02060E-10 | 0.000200498 | 6.56083E-10 |
| 2.50 | 0.00012265 | 8.26617E-10 | 0.00012324 | 8.25322E-10 | 0.000200505 | 6.56068E-10 |
| 3.00 | | | | | 0.000191797 | 6.75142E-10 |
| 3.50 | | | | | 0.000235859 | 5.78621E-10 |
| 4.00 | | | | | 0.000185039 | 6.89947E-10 |
| 4.50 | | | | | 0.000200569 | 6.55928E-10 |
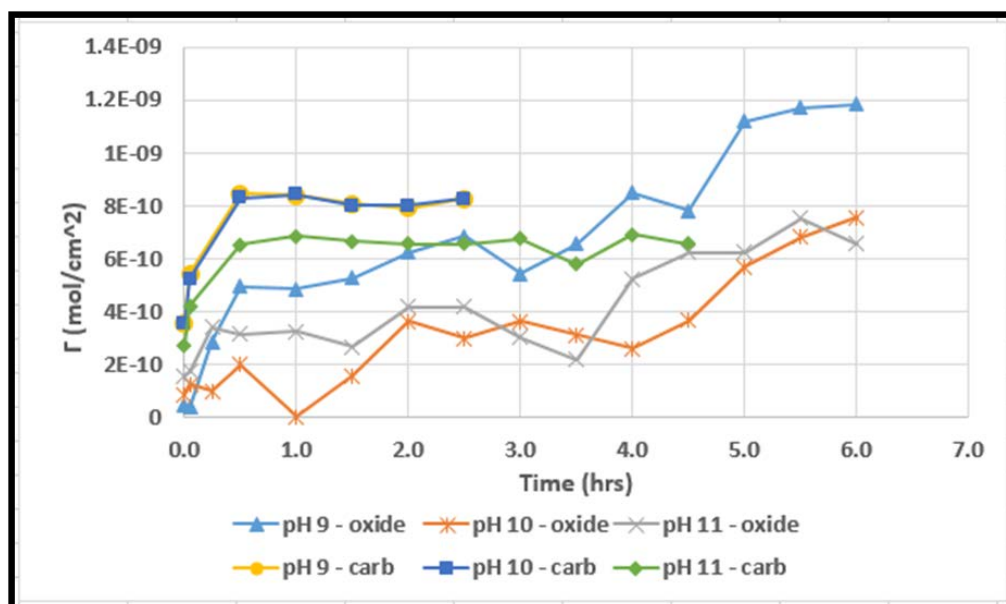
**Figure 79: Adsorption Densities of SHA in Eu Oxide and Carbonate for pHs 9, 10, and 11 at 20°C**

## Terbium (Tb)

**Table XVI: Concentration and Adsorption Density Values for SHA in Tb Oxide**

| Terbium Oxide, 20°C | | | | | | |
|---|---|---|---|---|---|---|
| | pH 9 | | pH 10 | | pH 11 | |
| Time (hrs) | Conc. (M) | $\Gamma$ (mol/cm$^2$) | Conc. (M) | $\Gamma$ (mol/cm$^2$) | Conc. (M) | $\Gamma$ (mol/cm$^2$) |
| 0.0 | 0.00056912 | 9.3983E-08 | 0.00055358 | 3.56578E-13 | 0.0006381 | 3.47630E-11 |
| 0.5 | 0.00052821 | 9.4734E-08 | 0.00055071 | 5.29927E-11 | 0.0005678 | 1.32476E-09 |
| 1.0 | 0.00052952 | 9.4710E-08 | 0.00051996 | 6.17188E-10 | 0.0006224 | 3.23185E-10 |
| 1.5 | 0.00048054 | 9.5608E-08 | 0.00053331 | 3.72289E-10 | 0.0005992 | 7.48250E-10 |
| 2.0 | 0.00050412 | 9.5176E-08 | 0.00053218 | 3.93001E-10 | 0.0005952 | 8.22592E-10 |
| 2.5 | 0.00050956 | 9.5076E-08 | 0.00049314 | 1.10930E-09 | 0.0006080 | 5.87967E-10 |
| 3.0 | 0.00049620 | 9.5321E-08 | 0.00047540 | 1.43479E-09 | 0.0006071 | 6.03929E-10 |
| 3.5 | 0.00042324 | 9.6660E-08 | 0.00043642 | 2.15015E-09 | 0.0005863 | 9.85913E-10 |
| 4.0 | 0.00040410 | 9.7011E-08 | 0.00036814 | 3.40287E-09 | 0.0005746 | 1.20032E-09 |
| 4.5 | 0.00040184 | 9.7053E-08 | 0.00038024 | 3.18095E-09 | 0.0005707 | 1.27168E-09 |
| 5.0 | 0.00033625 | 9.8256E-08 | 0.00034694 | 3.79198E-09 | | |

**Table XVII: Concentration and Adsorption Density Values for SHA in Tb Carbonate**

| Terbium Carbonate, 20°C | | | | | | |
|---|---|---|---|---|---|---|
| | pH 9 | | pH 10 | | pH 11 | |
| Time (hrs) | Conc. (M) | $\Gamma$ (mol/cm$^2$) | Conc. (M) | $\Gamma$ (mol/cm$^2$) | Conc. (M) | $\Gamma$ (mol/cm$^2$) |
| 0.00 | 0.00054906 | 6.5054E-15 | 0.00051757 | 2.88231E-14 | 0.0006405 | 4.40139E-13 |
| 0.05 | 0.00013248 | 4.0445E-09 | 0.00036380 | 1.49295E-09 | 0.0003733 | 2.59454E-09 |
| 0.25 | 1.9995E-05 | 5.1366E-09 | 0.00020254 | 3.05856E-09 | 3.814E-05 | 5.84820E-09 |
| 0.50 | 2.3307E-05 | 5.1044E-09 | 0.00017842 | 3.29272E-09 | 3.282E-05 | 5.89977E-09 |
| 0.75 | 2.0392E-05 | 5.1327E-09 | 0.00014570 | 3.61036E-09 | 3.581E-05 | 5.87077E-09 |
| 1.00 | | | 0.00014955 | 3.57305E-09 | 4.292E-05 | 5.80177E-09 |
| 1.25 | | | 0.00014637 | 3.60390E-09 | | |
| 1.50 | | | | | | |
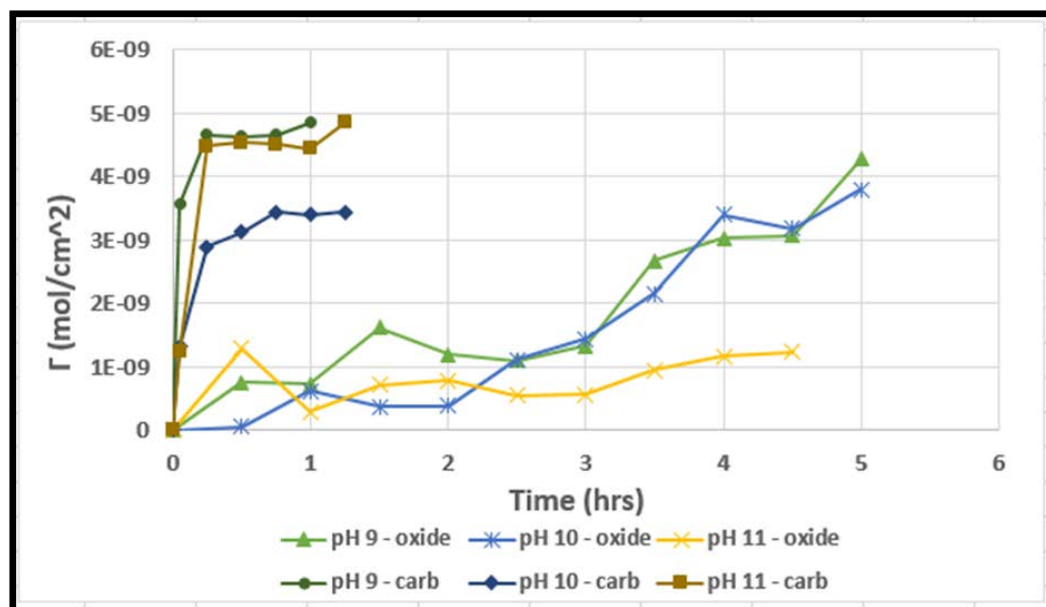


**Figure 80: Adsorption Densities of SHA in Tb Oxide and Carbonate for pHs 9, 10, and 11 at 20°C**
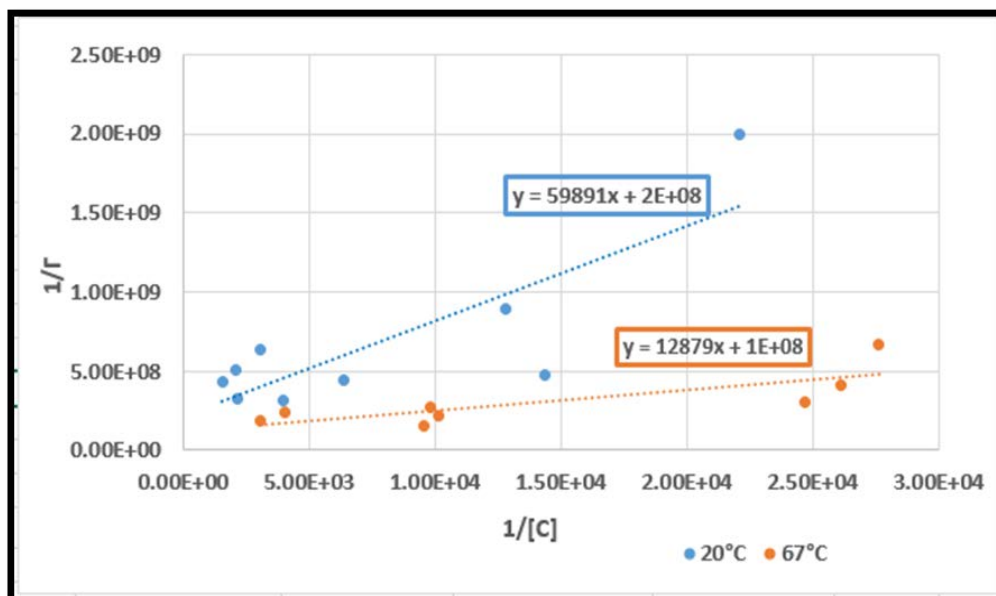
**Figure 81: Inverse Adsorption Density vs. Inverse Concentration of SHA in Tb Oxide at pH 10**
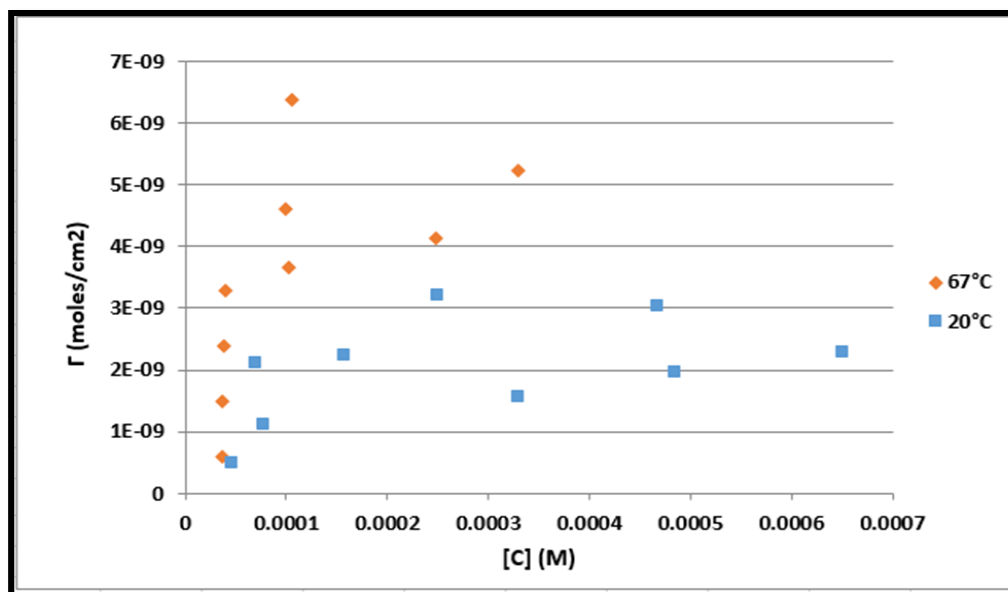


**Figure 82: Adsorption Density vs. Concentration of SHA in Tb Oxide at pH 10**
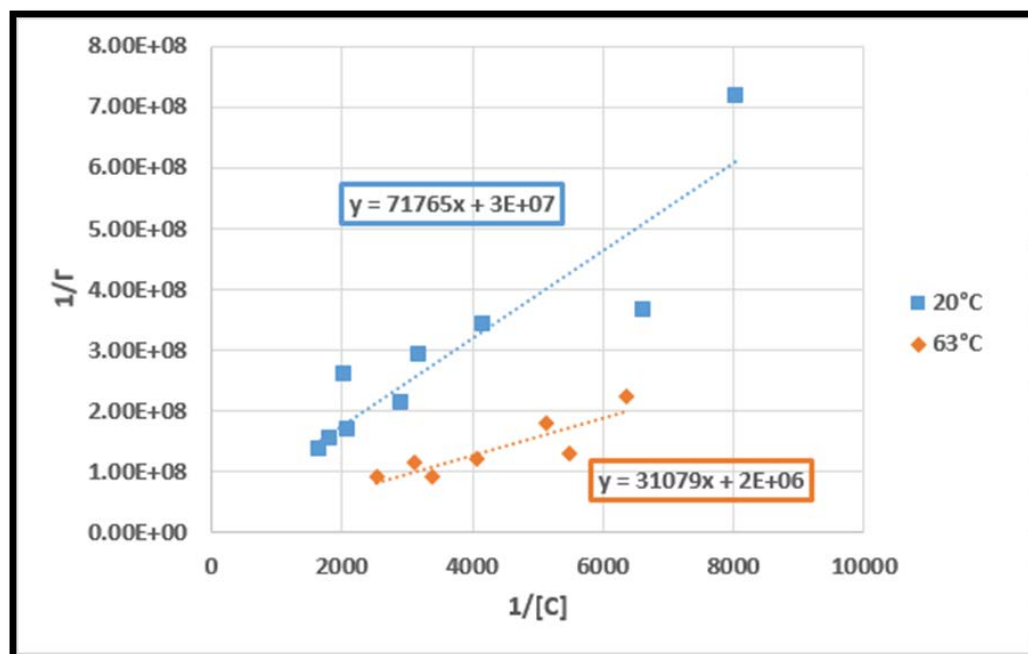
**Figure 83: Inverse Adsorption Density vs. Inverse Concentration of SHA in Tb Oxide at pH 11**
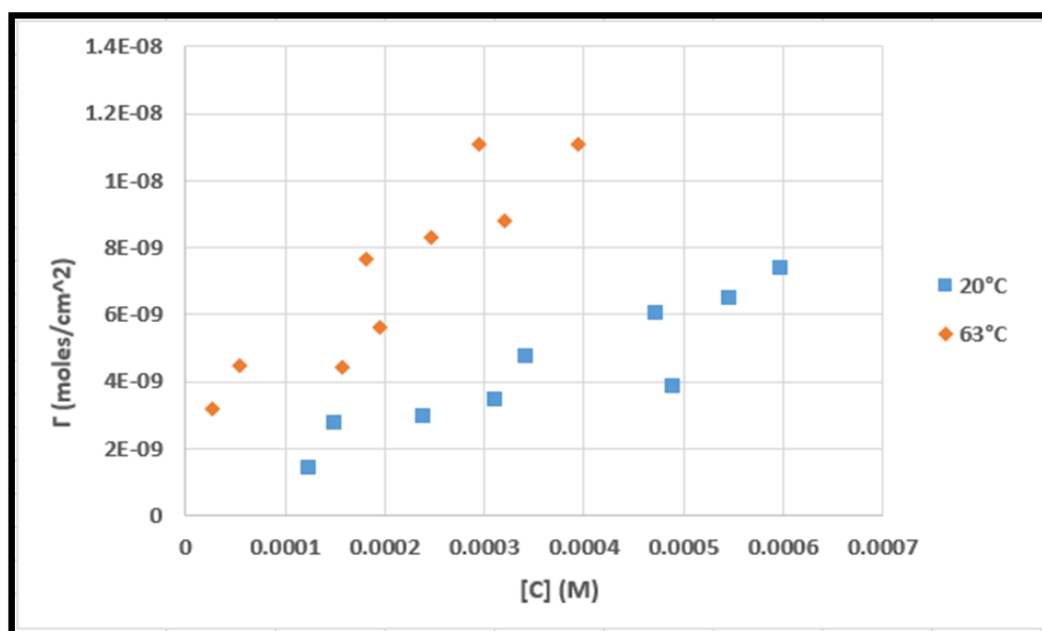


**Figure 84: Adsorption Density vs. Concentration of SHA in Tb Oxide at pH 11**

## APPENDIX C: REE StabCal Models with SHA

### Lanthanum (La)
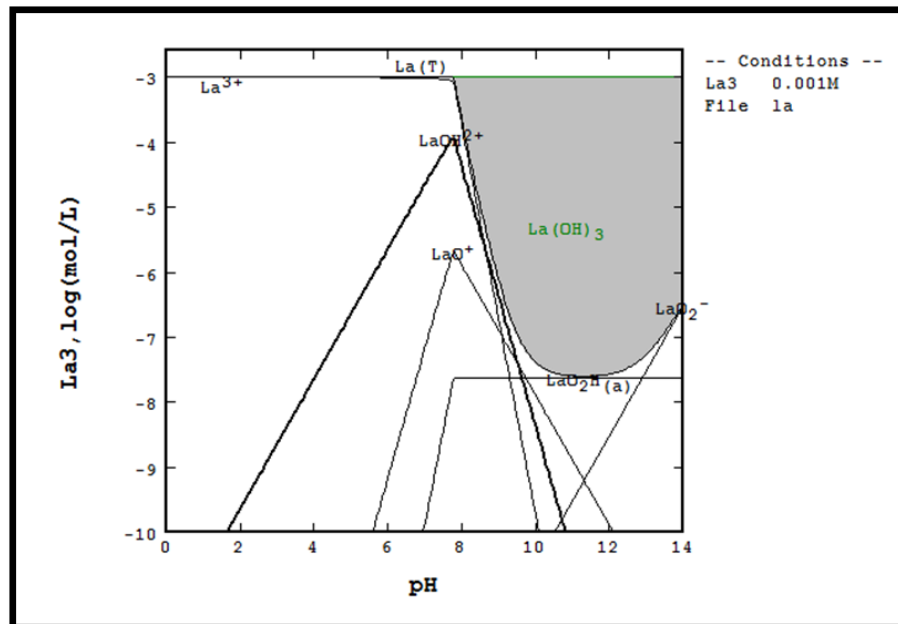


**Figure 85: Speciation Diagram of the La Hydroxide System without Collector**
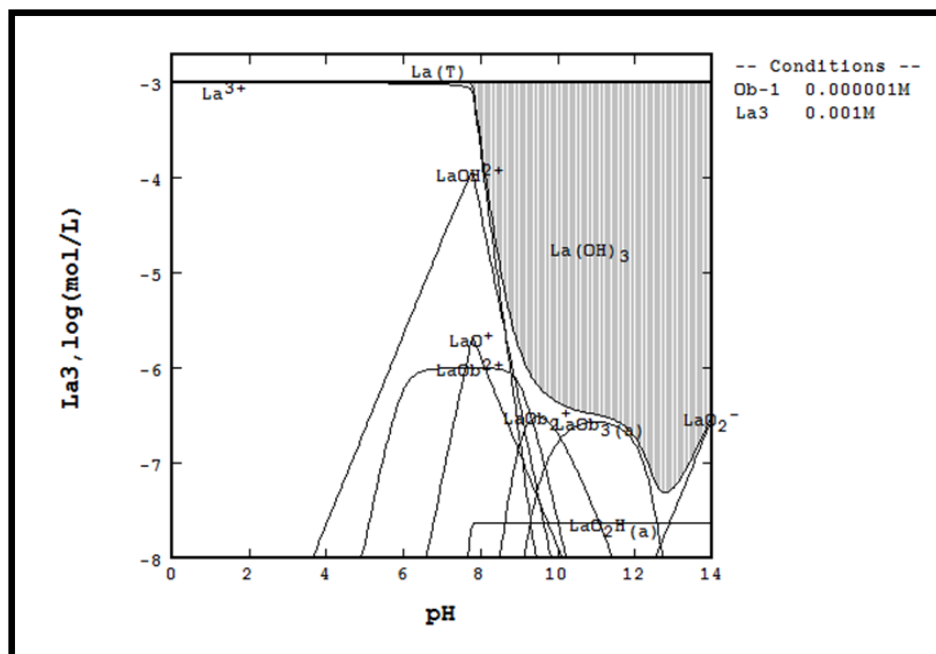


**Figure 86: Speciation Diagram of the La Hydroxide System with 1E-6M SHA**
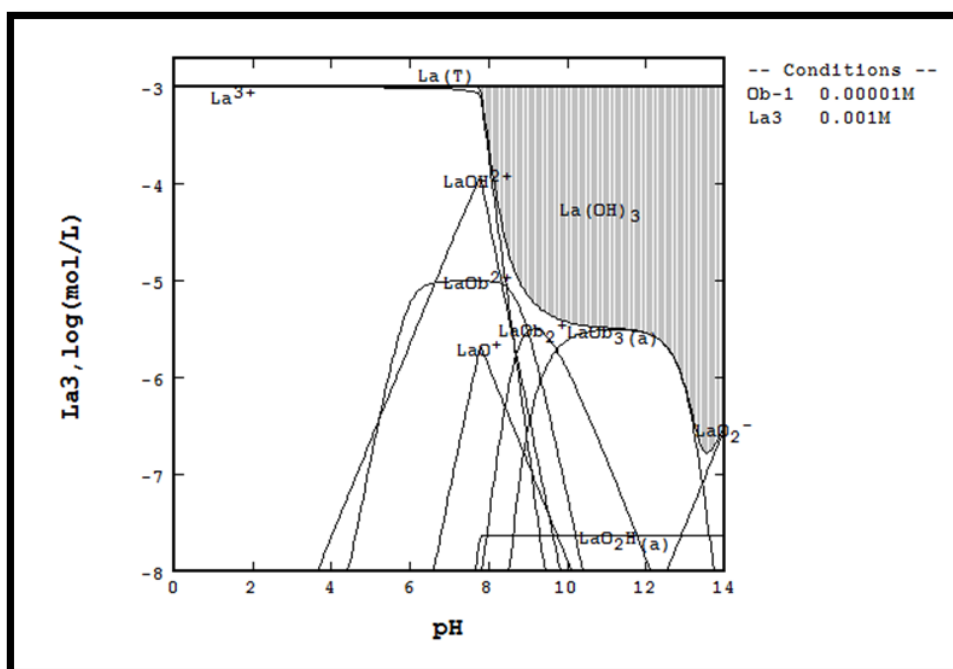
**Figure 87: Speciation Diagram for the La Hydroxide System with 1E-5M SHA**
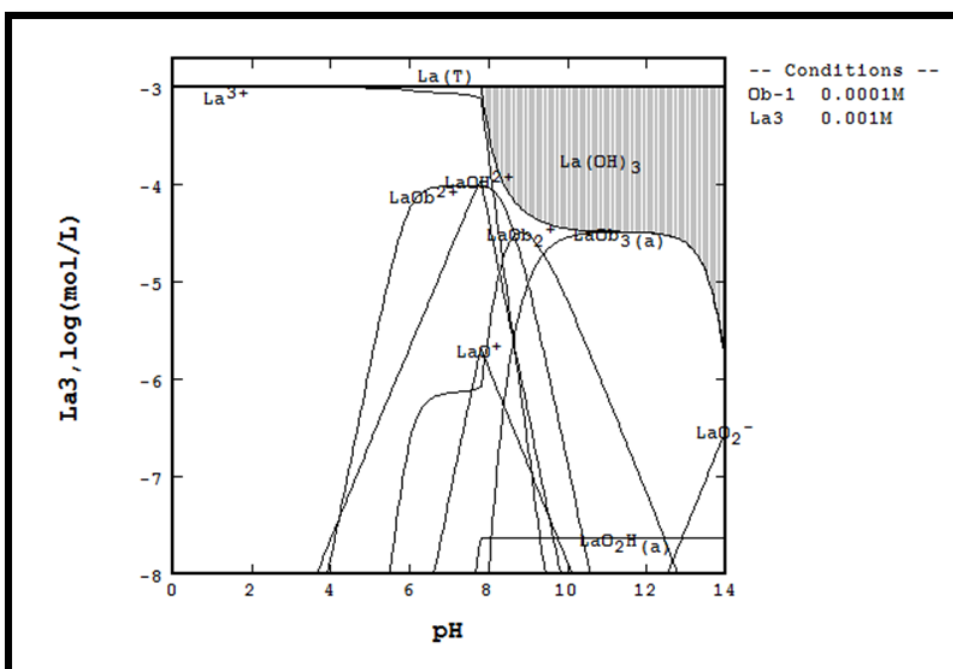


**Figure 88: Speciation Diagram for the La Hydroxide System with 1E-4M SHA**
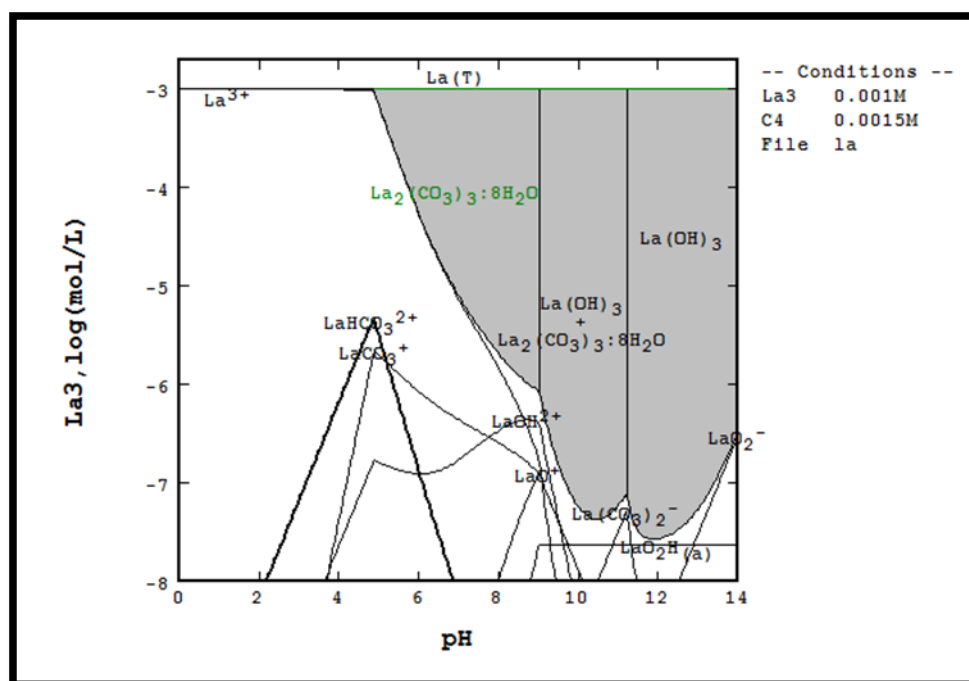
**Figure 89: Speciation Diagram for the La Carbonate System without Collector**
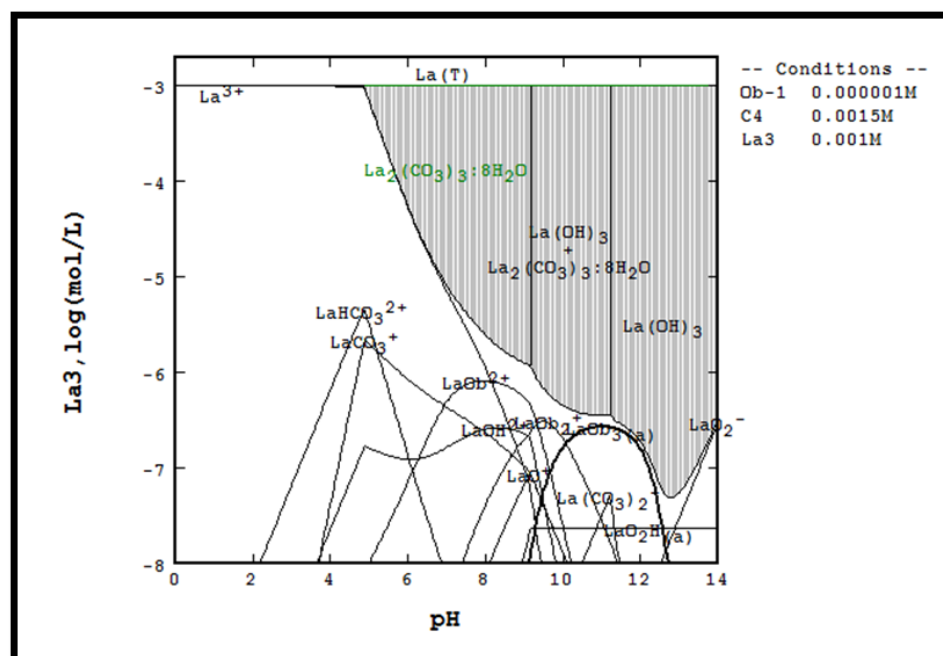


**Figure 90: Speciation Diagram for the La Carbonate System with 1E-6M SHA**

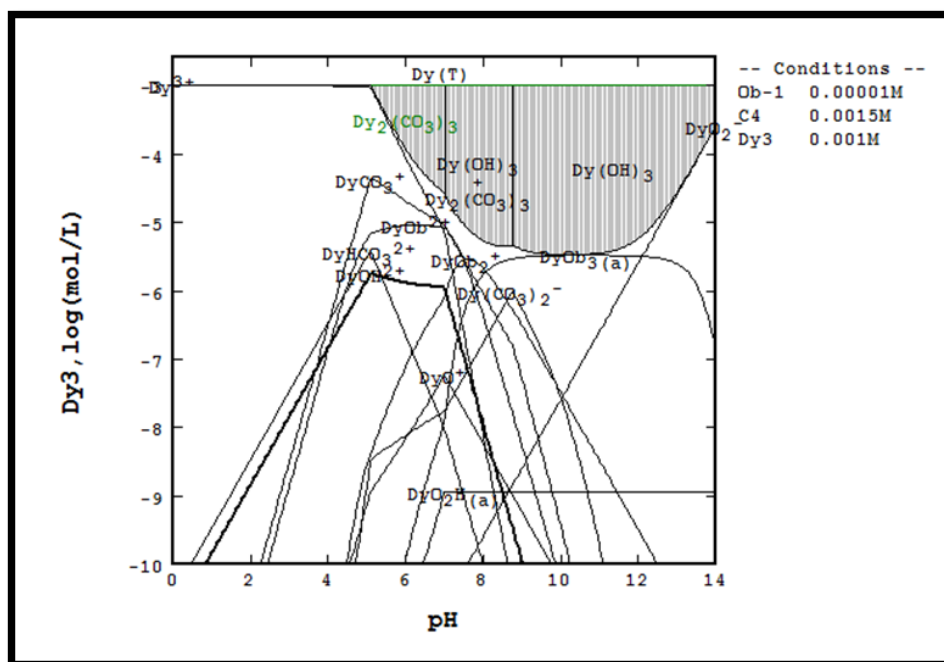**Figure 91: Speciation Diagram for the La Carbonate System with 1E-5M SHA**



**Figure 92: Speciation Diagram for the La Carbonate System with 1E-4M SHA**
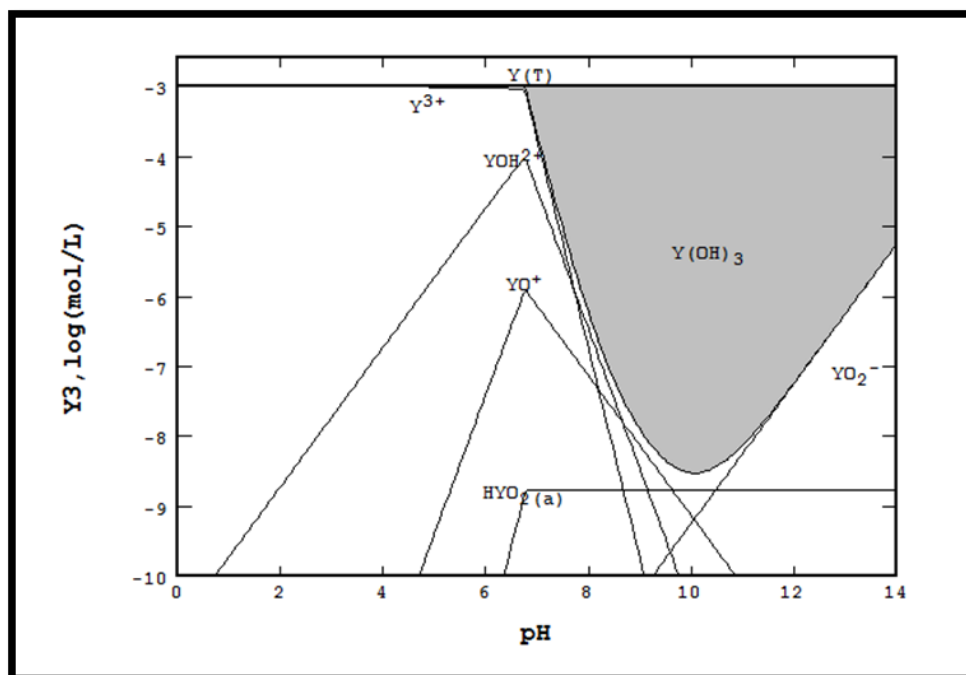
# Neodymium (Nd)
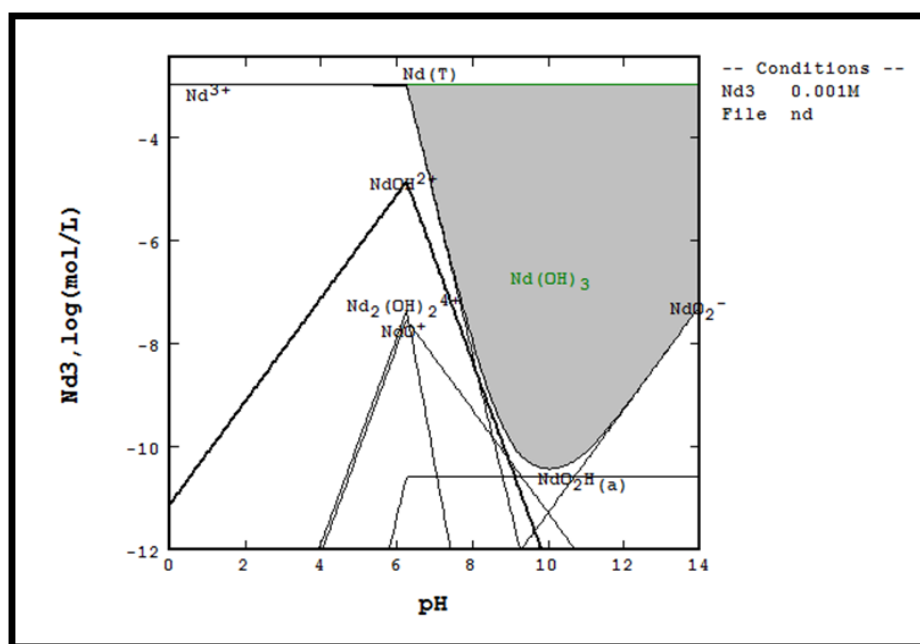


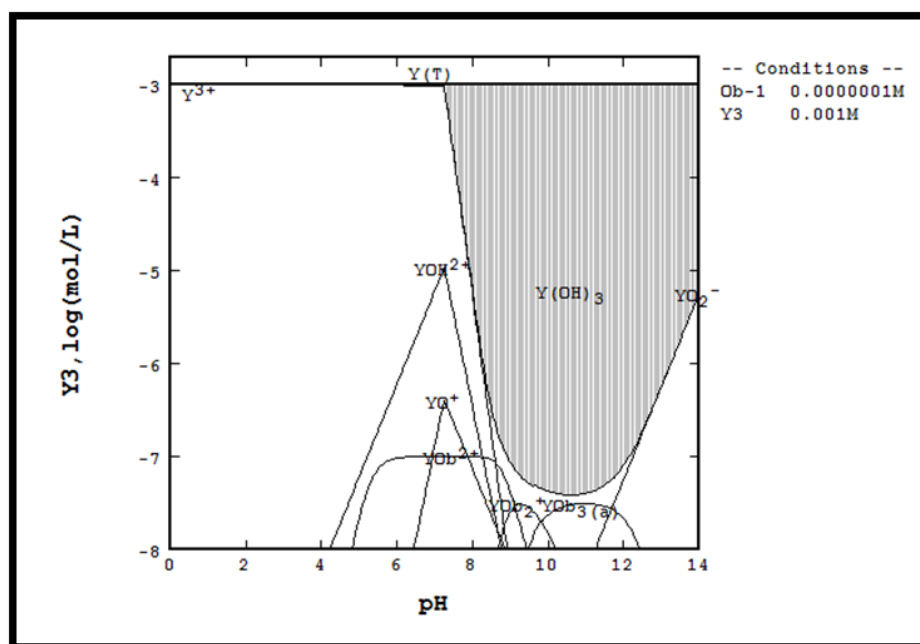**Figure 93: Speciation Diagram for the Nd Hydroxide System without Collector**
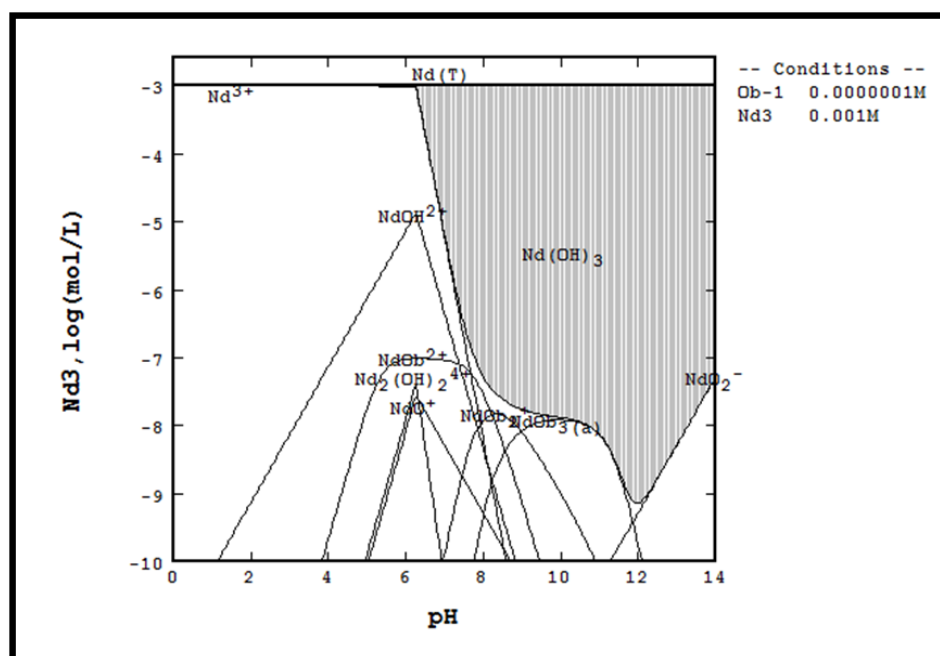


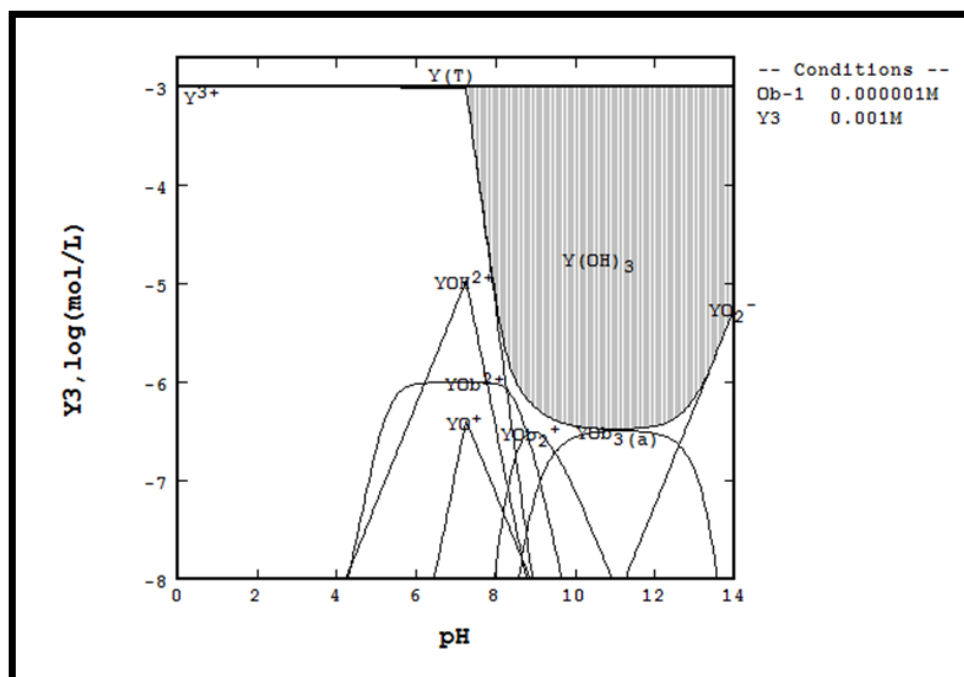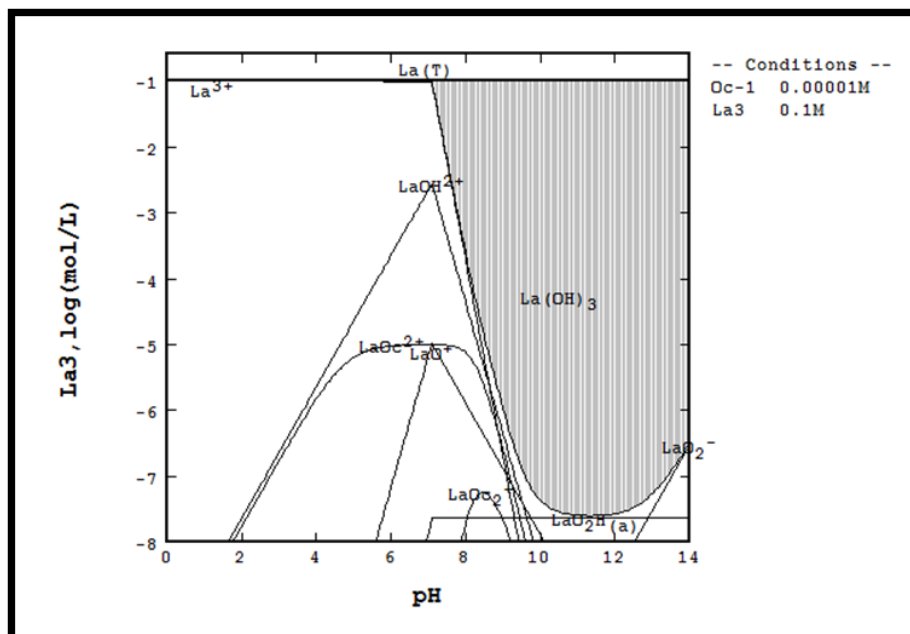**Figure 94: Speciation Diagram for the Nd Hydroxide System with 1E-7M SHA**
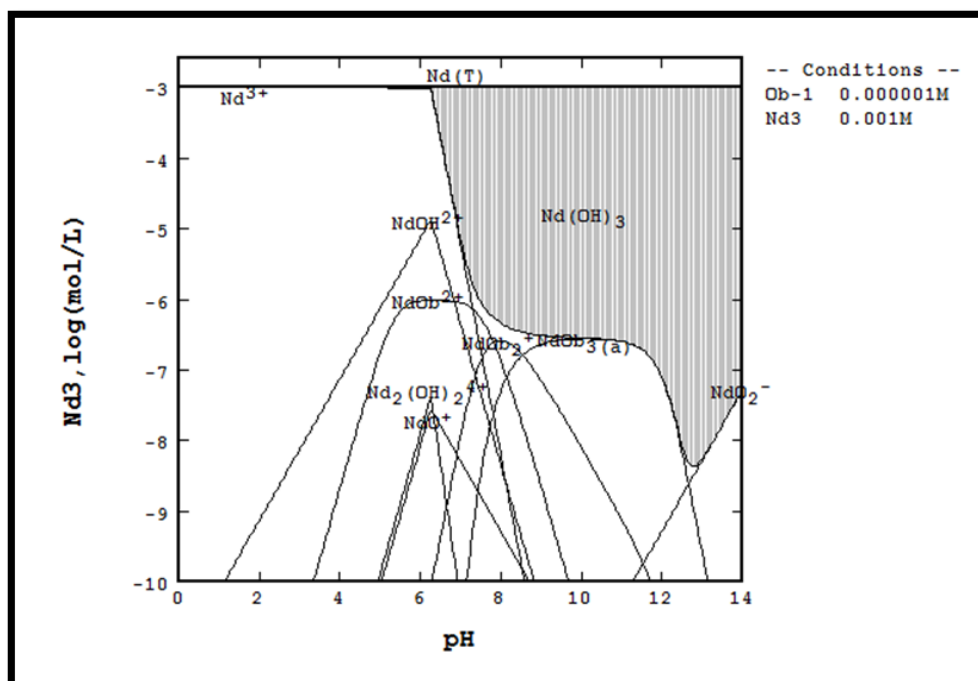
**Figure 95: Speciation Diagram for the Nd Hydroxide System with 1E-6M SHA**
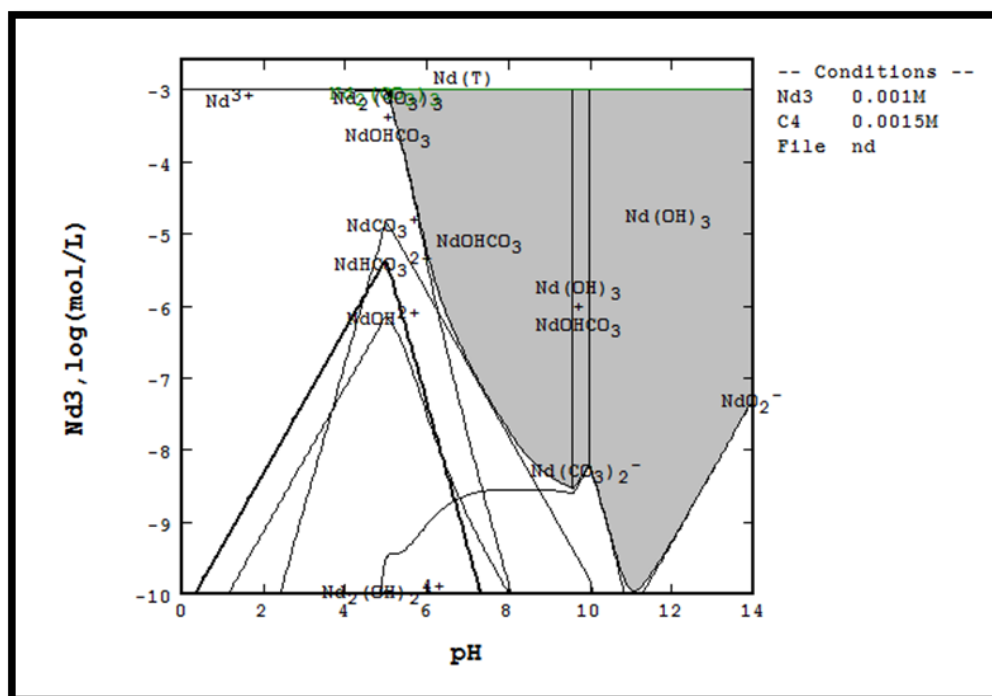


**Figure 96: Speciation Diagram for the Nd Carbonate System without Collector**
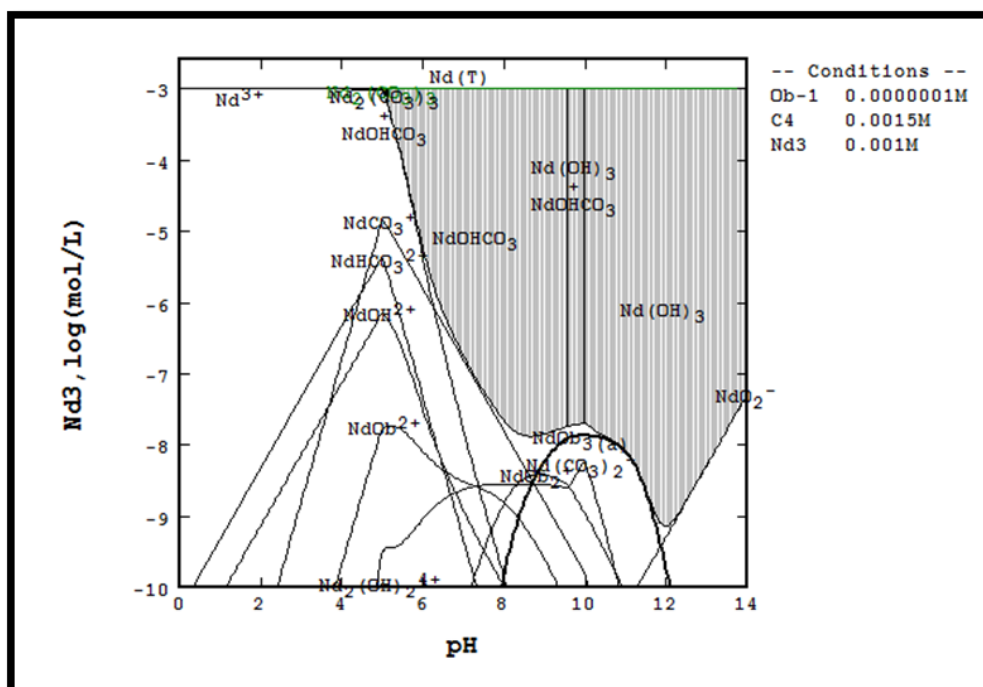
**Figure 97: Speciation Diagram for the Nd Carbonate System with 1E-7M SHA**
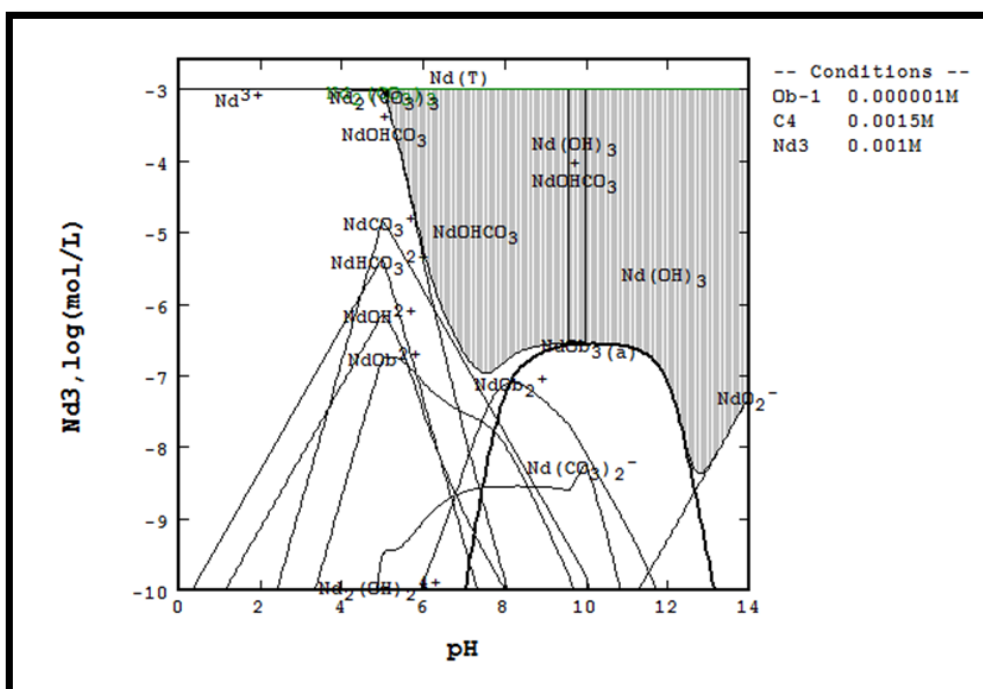


**Figure 98: Speciation Diagram for the Nd Carbonate System with 1E-6M SHA**
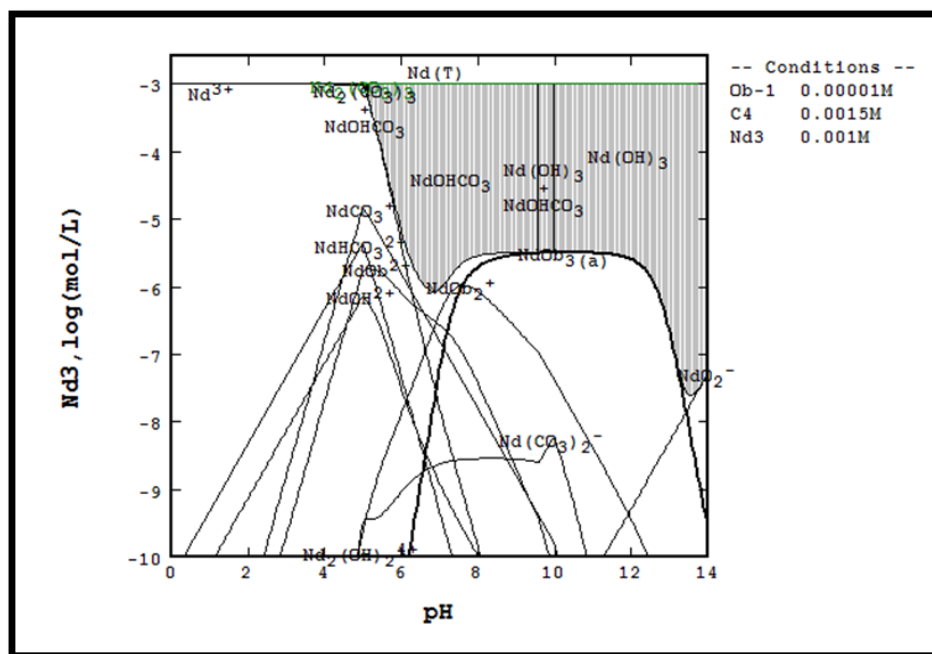
**Figure 99: Speciation Diagram for the Nd Carbonate System with 1E-5M SHA**

# Dysprosium (Dy)
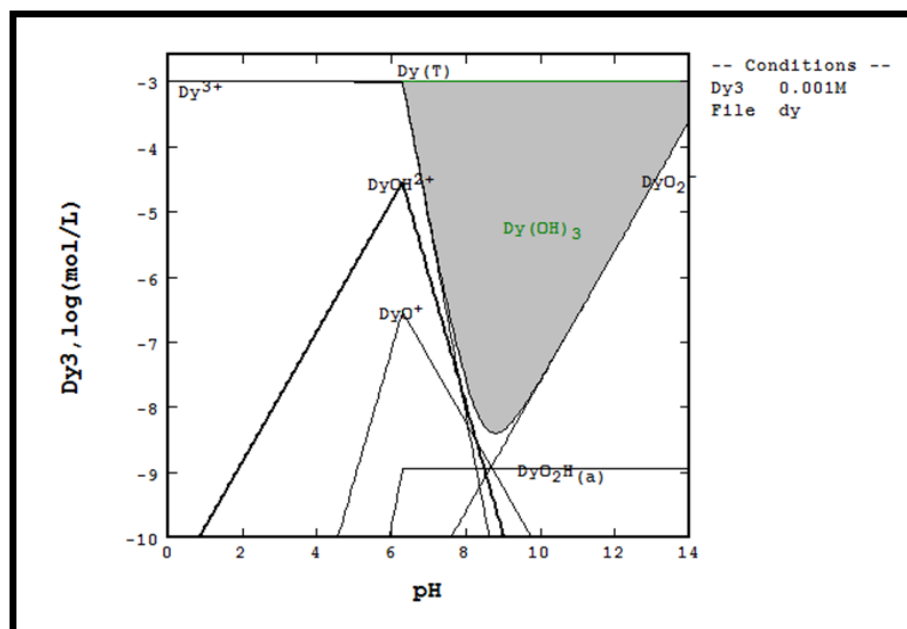


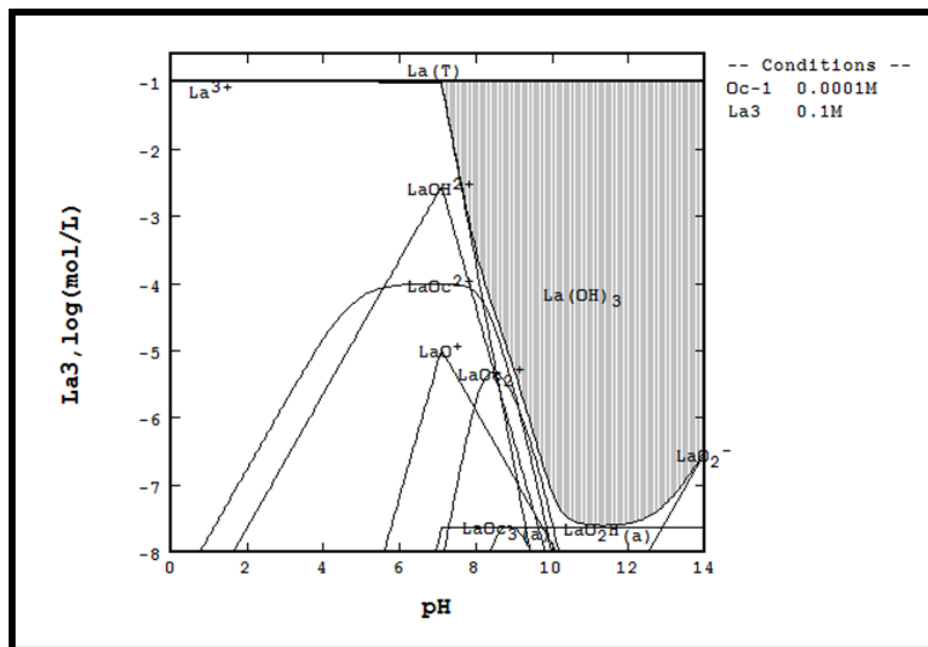**Figure 100: Speciation Diagram for the Dy Hydroxide System without Collector**
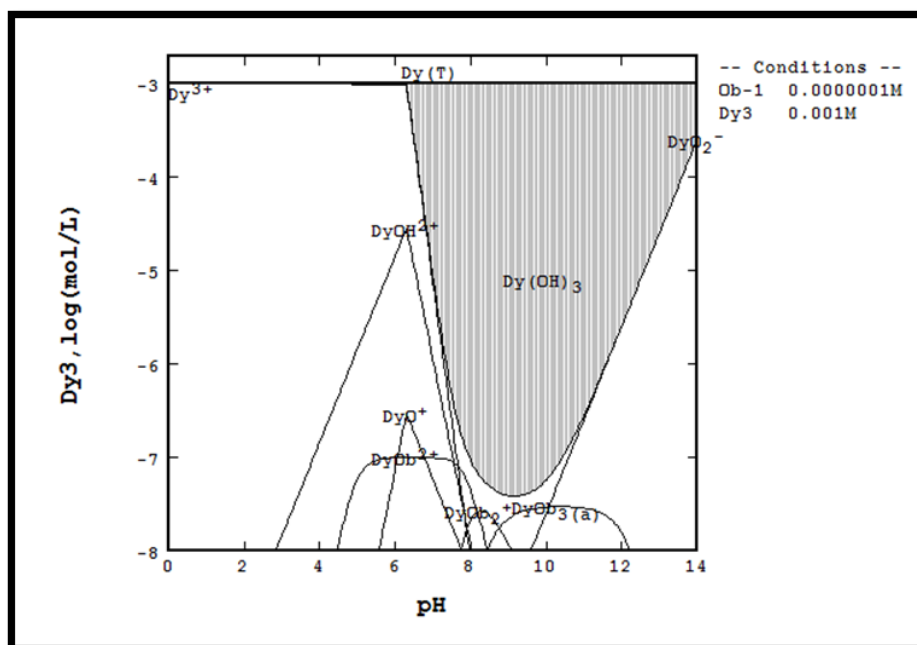
**Figure 101: Speciation Diagram for the Dy Hydroxide System with 1E-7M SHA**
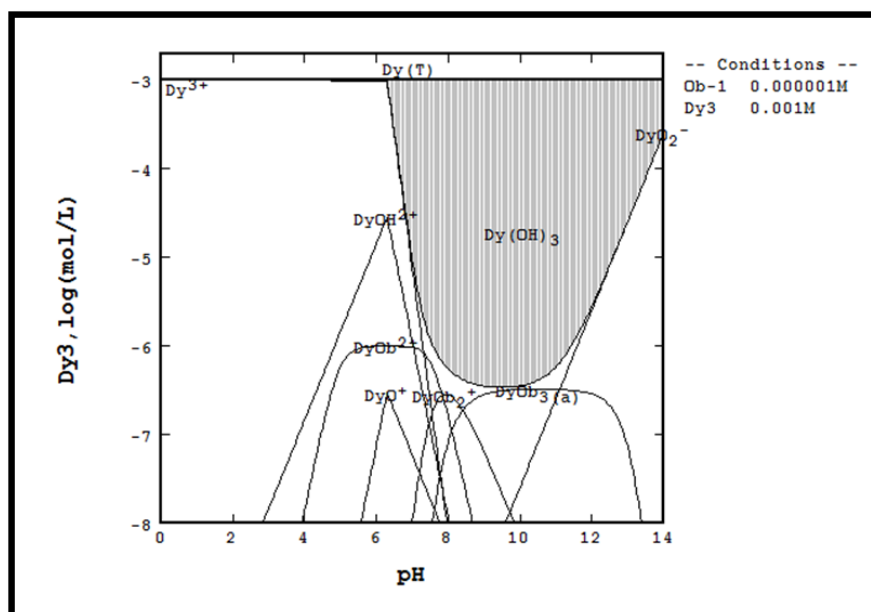


**Figure 102: Speciation Diagram for the Dy Hydroxide system with 1E-6M SHA**
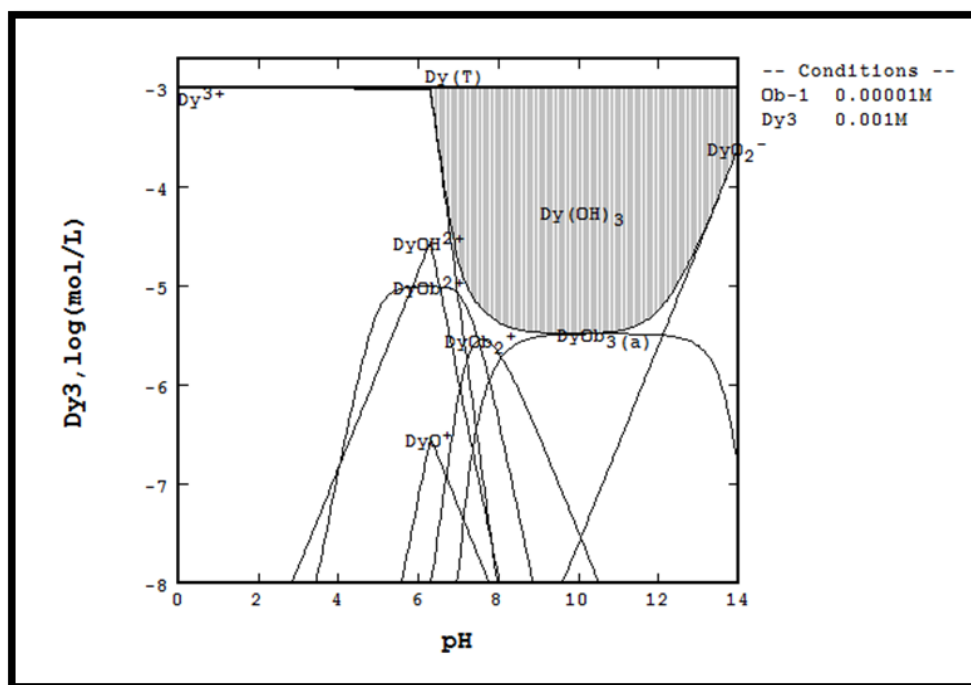
**Figure 103: Speciation Diagram for the Dy Hydroxide System with 1E-5M SHA**
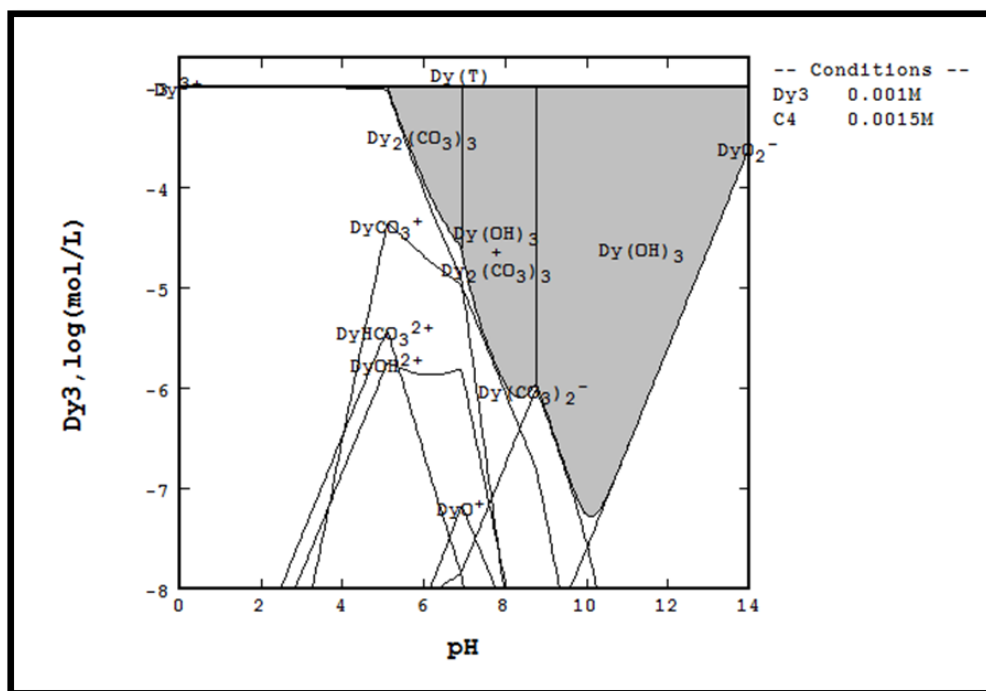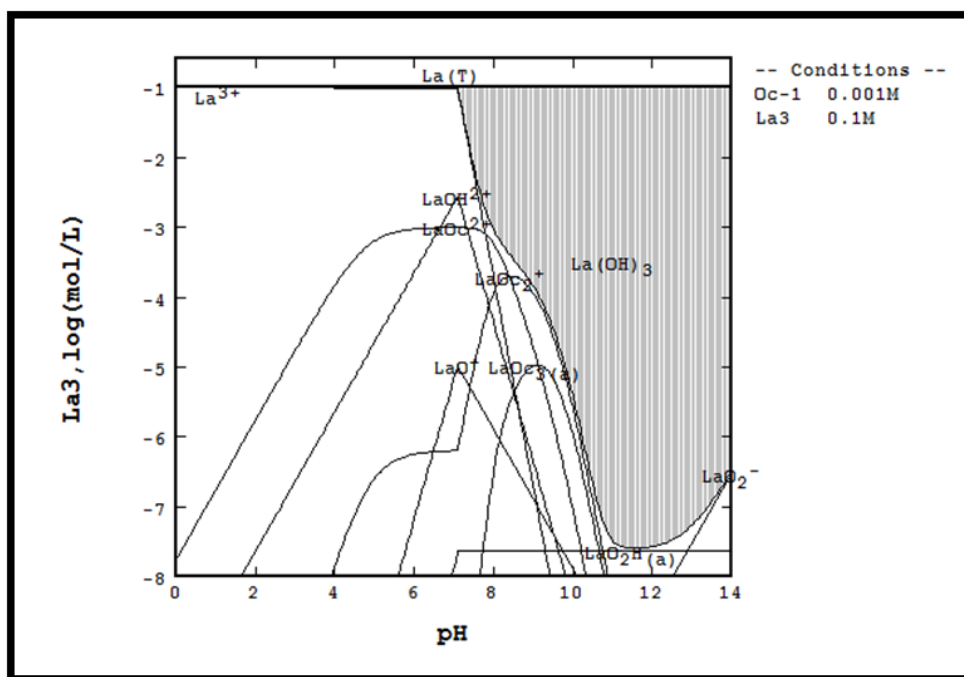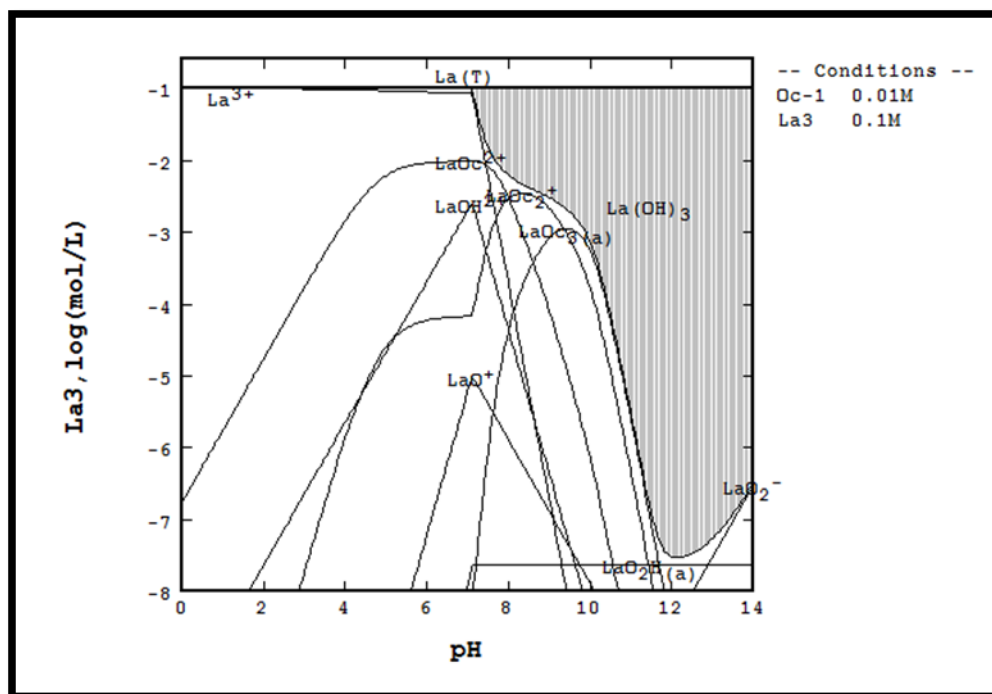


**Figure 104: Speciation Diagram for the Dy Carbonate System without Collector**
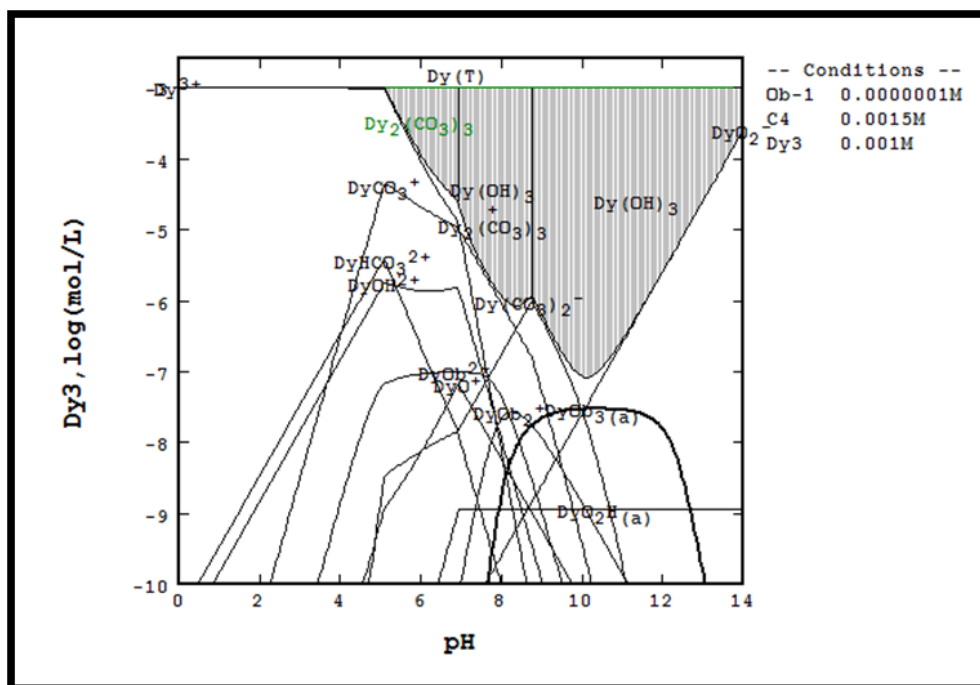
**Figure 105: Speciation Diagram for the Dy Carbonate System with 1E-7M SHA**
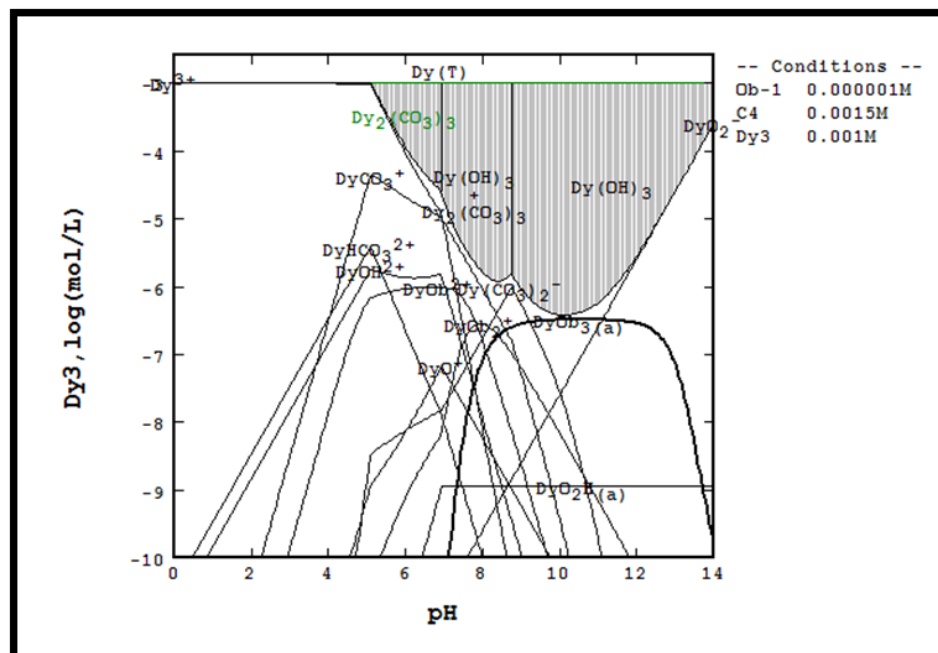


**Figure 106: Speciation Diagram for the Dy Carbonate System with 1E-6M SHA**

**Figure 107: Speciation Diagram for the Dy Carbonate System with 1E-5M SHA**

# Yttrium (Y)



**Figure 108: Speciation Diagram for the Y Hydroxide System without Collector**

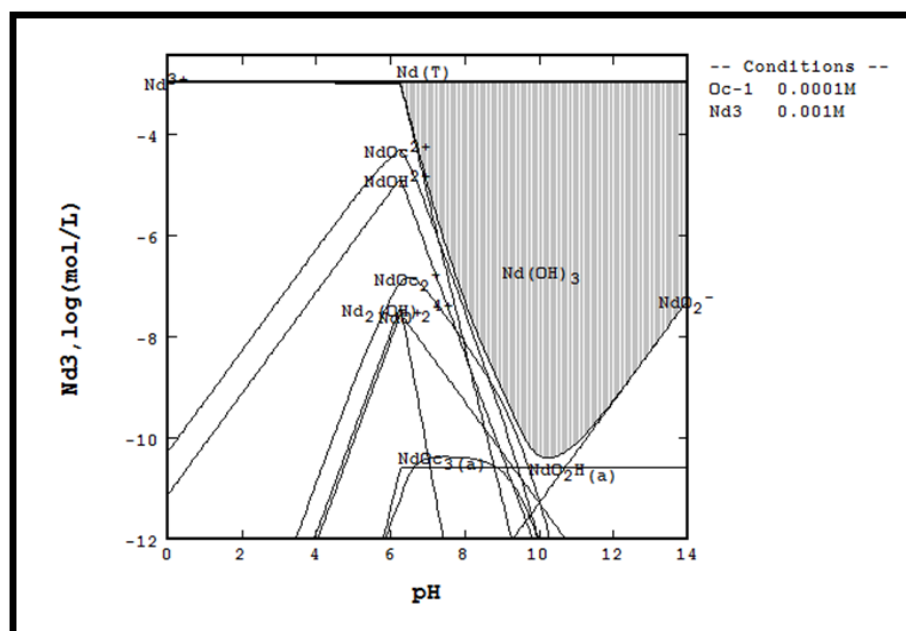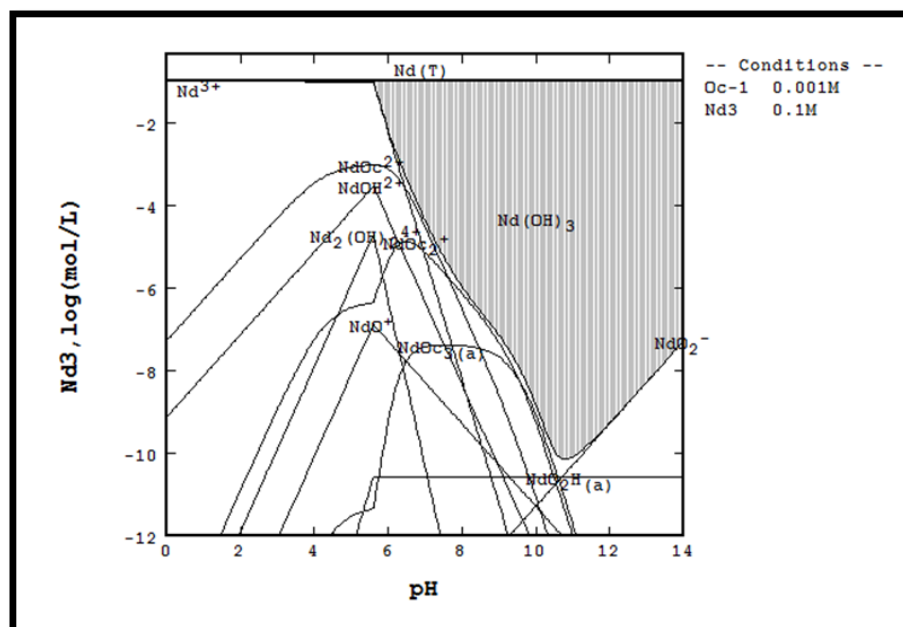**Figure 109: Speciation Diagram for the Y Hydroxide System with 1E-7M SHA**



**Figure 110: Speciation Diagram for the Y Hydroxide System with 1E-6M SHA**

**Figure 111: Speciation Diagram for the Y Hydroxide System with 1E-5M SHA**

# APPENDIX D: REE StabCal Models with OHA

## Lanthanum (La)



**Figure 112: Speciation Diagram for the La Hydroxide System with 1E-5M OHA**



**Figure 113: Speciation Diagram for the La Hydroxide System with 1E-4M OHA**

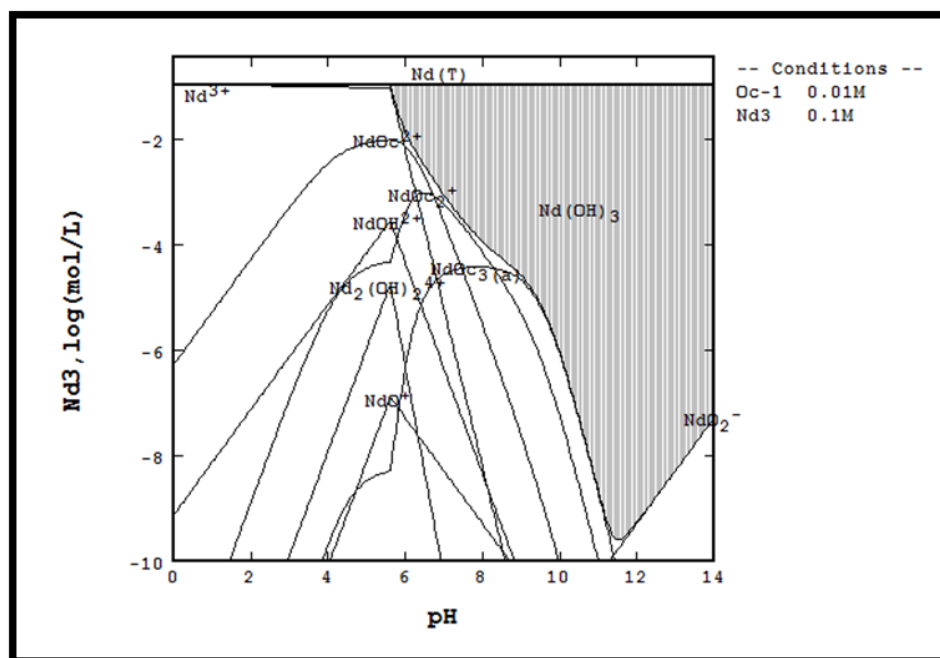**Figure 114: Speciation Diagram for the La Hydroxide System with 0.001M OHA**



**Figure 115: Speciation Diagram for the La Hydroxide System with 0.01M OHA**

# Neodymium (Nd)



**Figure 116: Speciation Diagram for the Nd Hydroxide System with 1E-4M OHA**



**Figure 117: Speciation Diagram for the Nd Hydroxide System with 0.001M OHA**

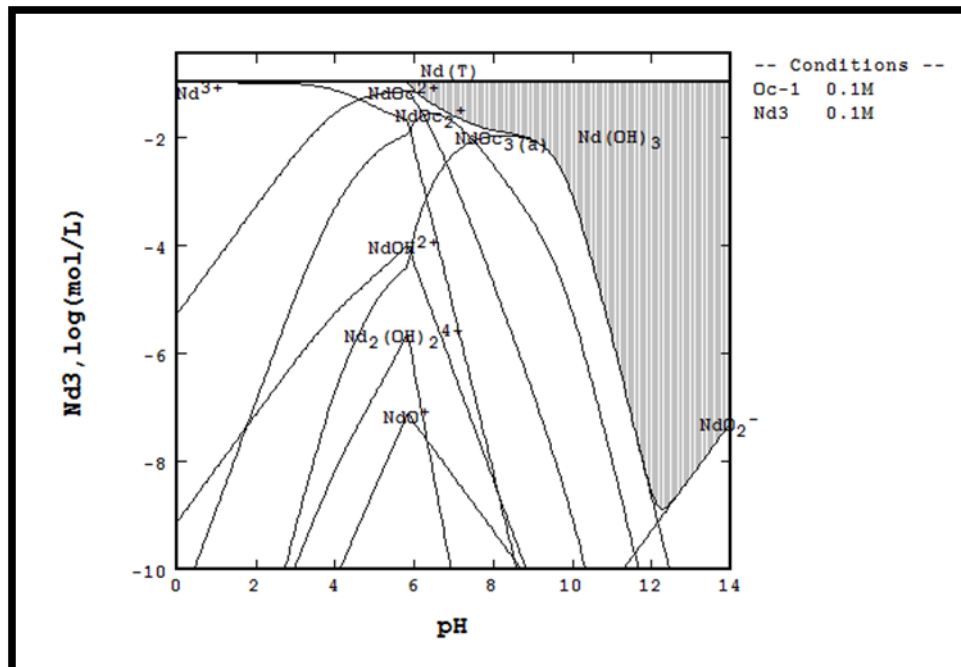**Figure 118: Speciation Diagram for the Nd Hydroxide System with 0.01M OHA**



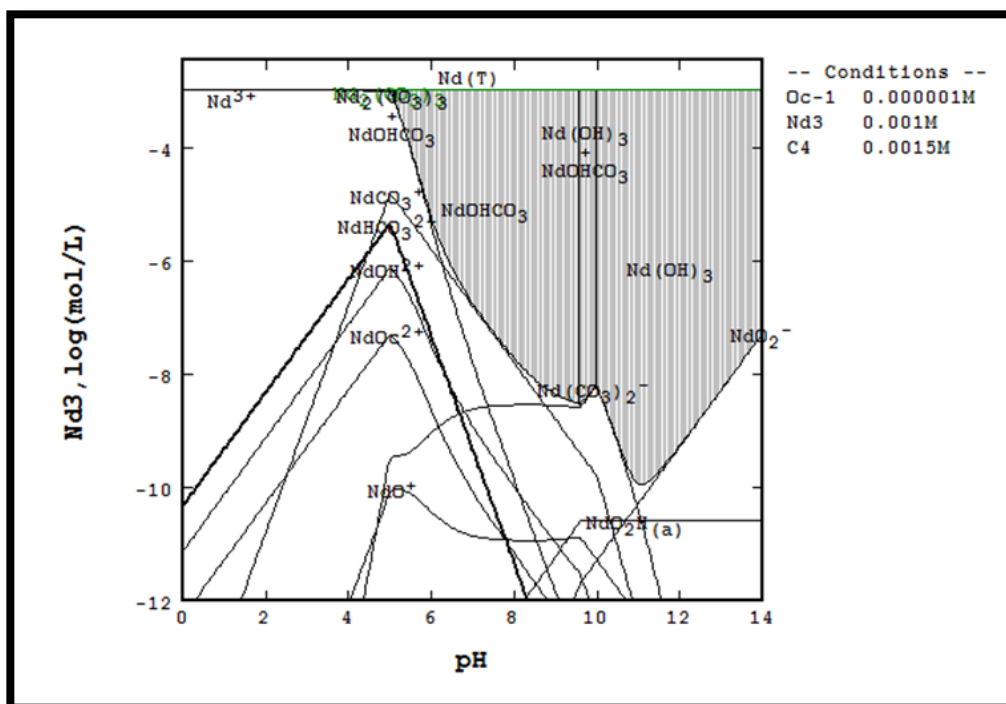**Figure 119: Speciation Diagram for the Nd Hydroxide System with 0.1M OHA**

**Figure 120: Speciation Diagram for the Nd Carbonate System with 1E-6M OHA**
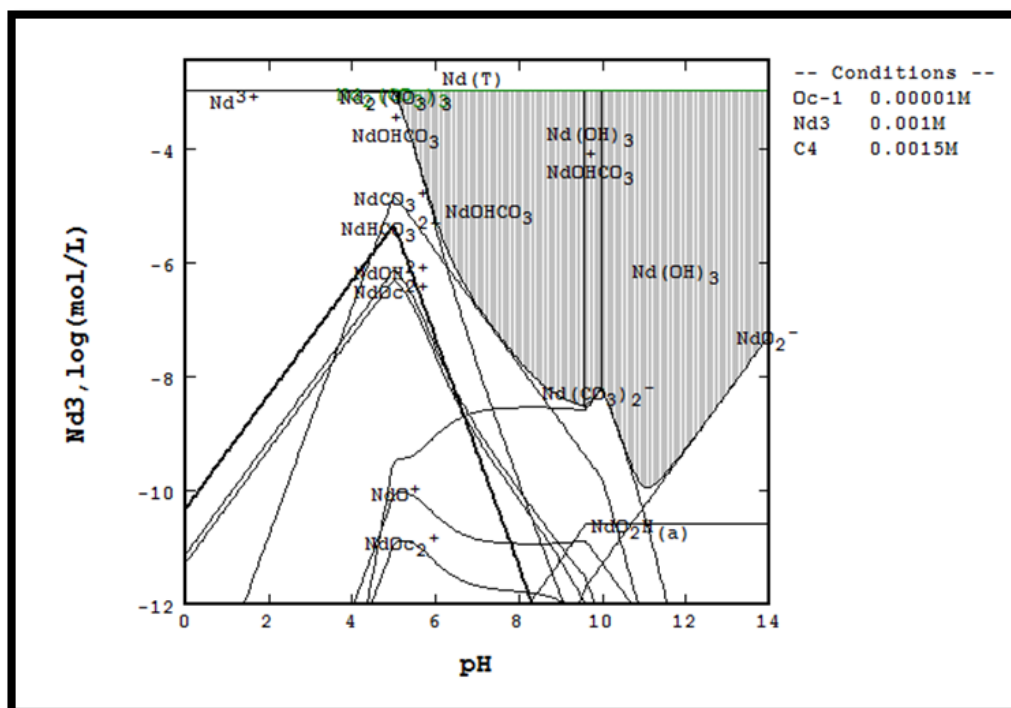


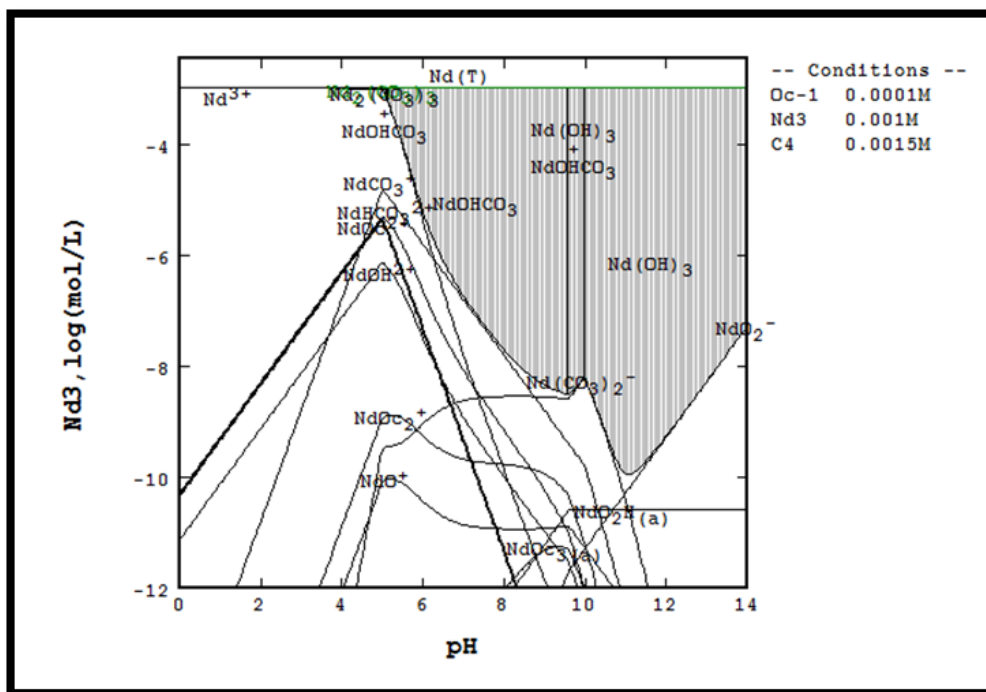**Figure 121: Speciation Diagram for the Nd Carbonate System with 1E-5M OHA**

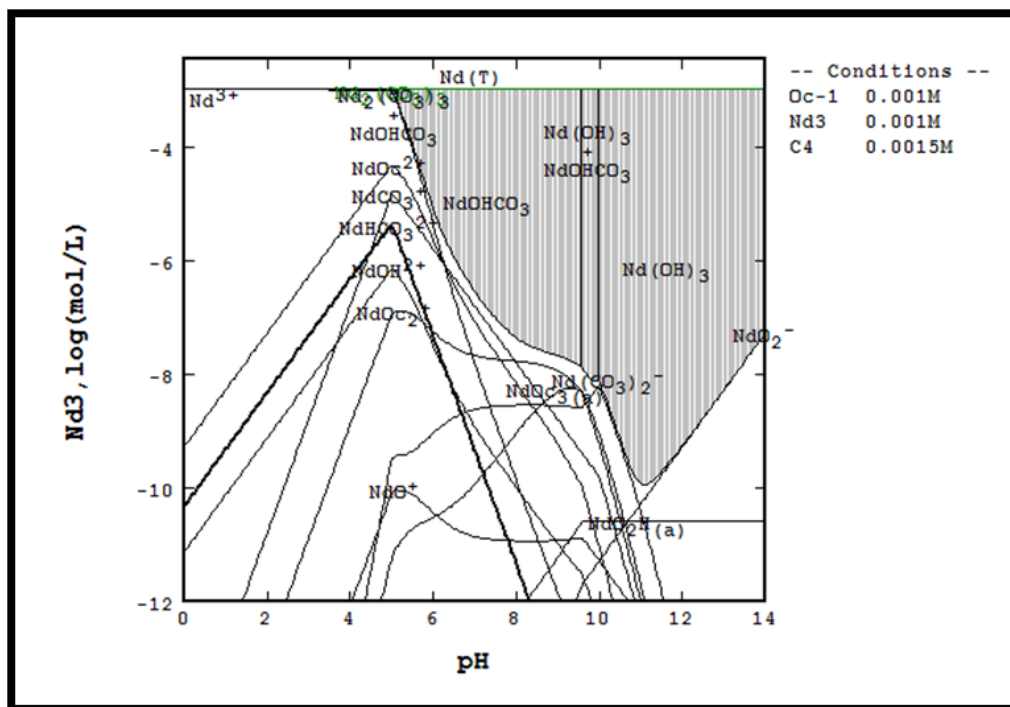**Figure 122: Speciation Diagram for the Nd Carbonate System with 1E-4M OHA**



**Figure 123: Speciation Diagram for the Nd Carbonate System with 0.001M OHA**

**Figure 124: Speciation Diagram for the Nd Carbonate System with 0.01M OHA**

# Dysprosium (Dy)



**Figure 125: Speciation Diagram for the Dy Hydroxide System with 1E-5M OHA**
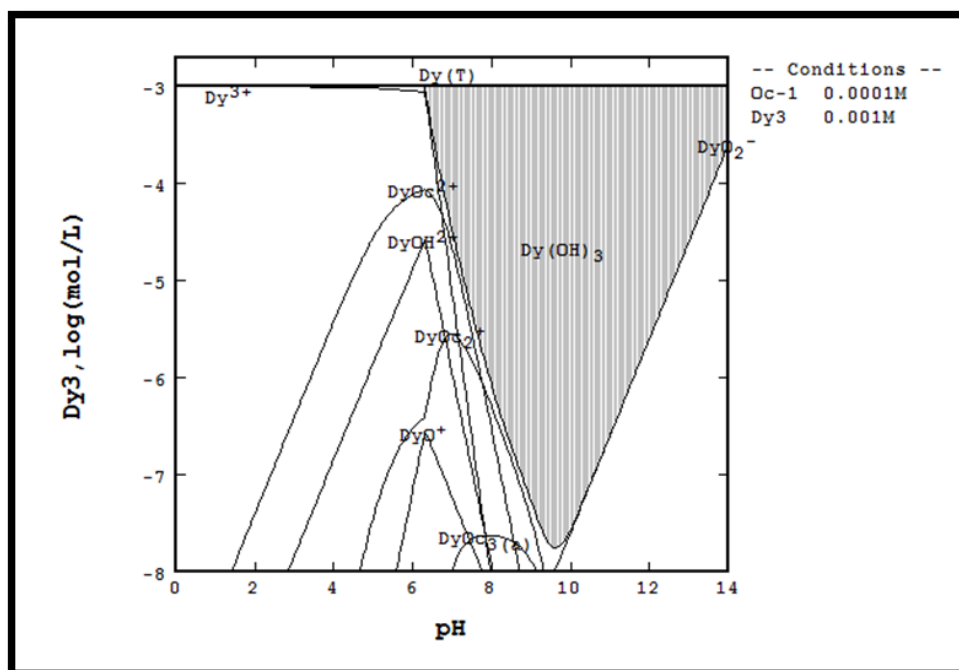
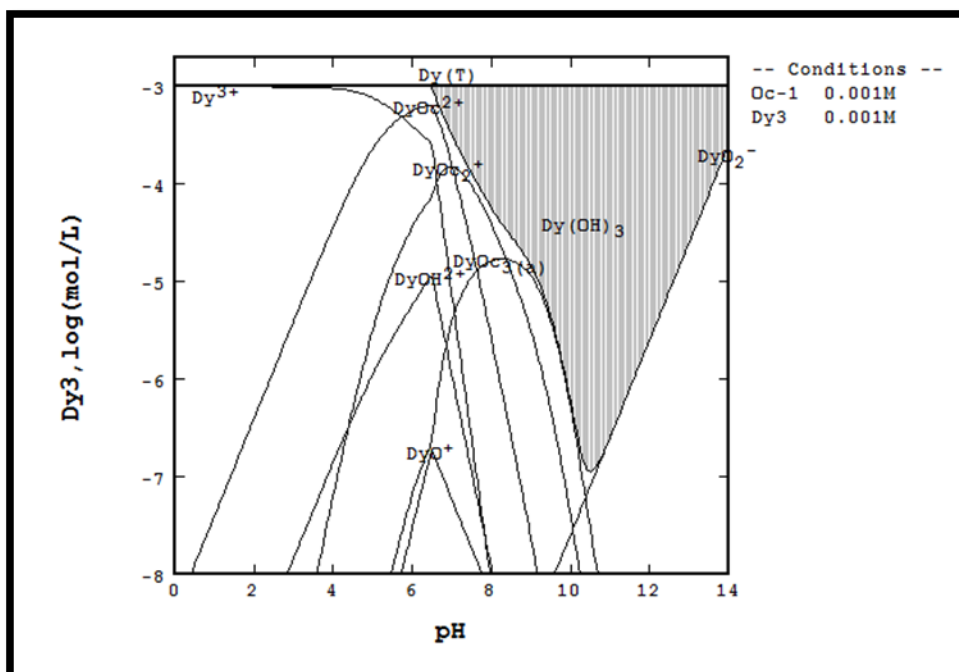**Figure 126: Speciation Diagram for the Dy Hydroxide System with 1E-4M OHA**



**Figure 127: Speciation Diagram for the Dy Hydroxide System with 0.001M OHA**
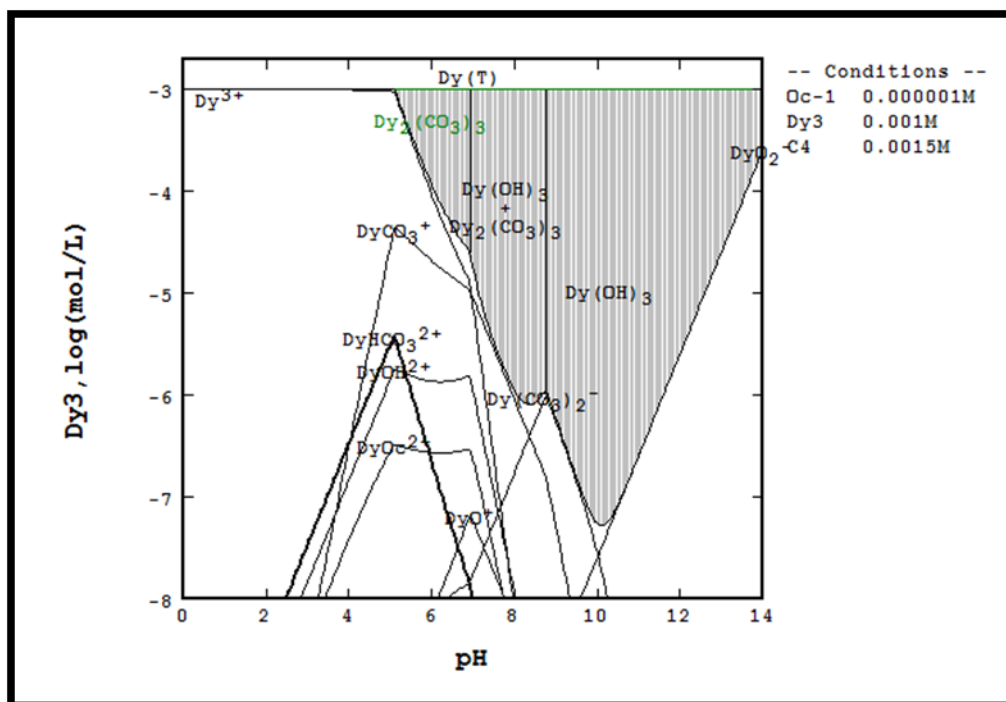
**Figure 128: Speciation Diagram for the Dy Carbonate System with 1E-6M OHA**
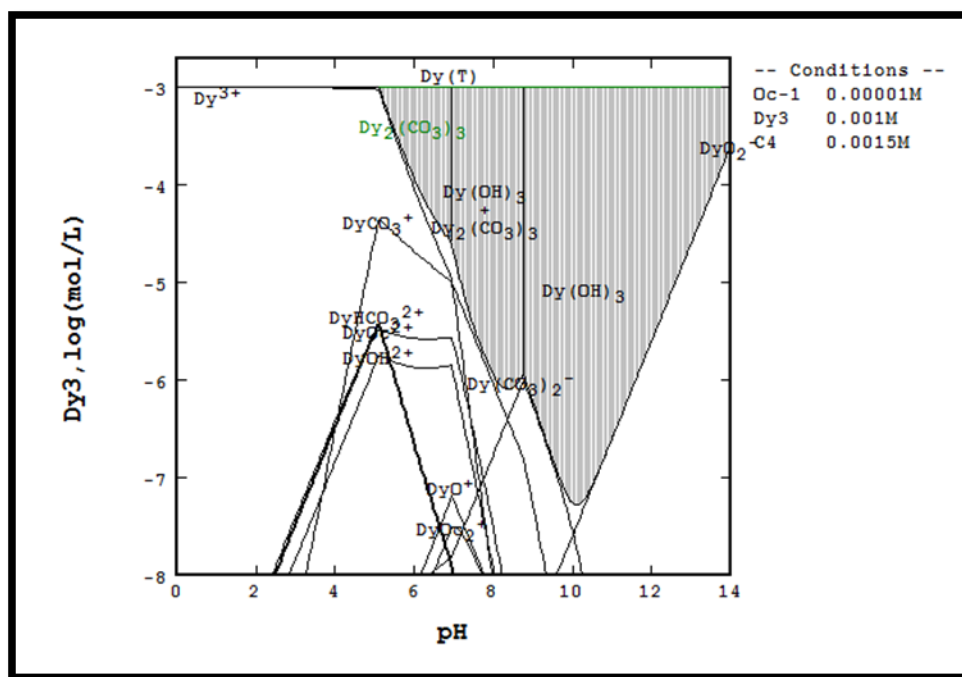


**Figure 129: Speciation Diagram for the Dy Carbonate System with 1E-5M OHA**
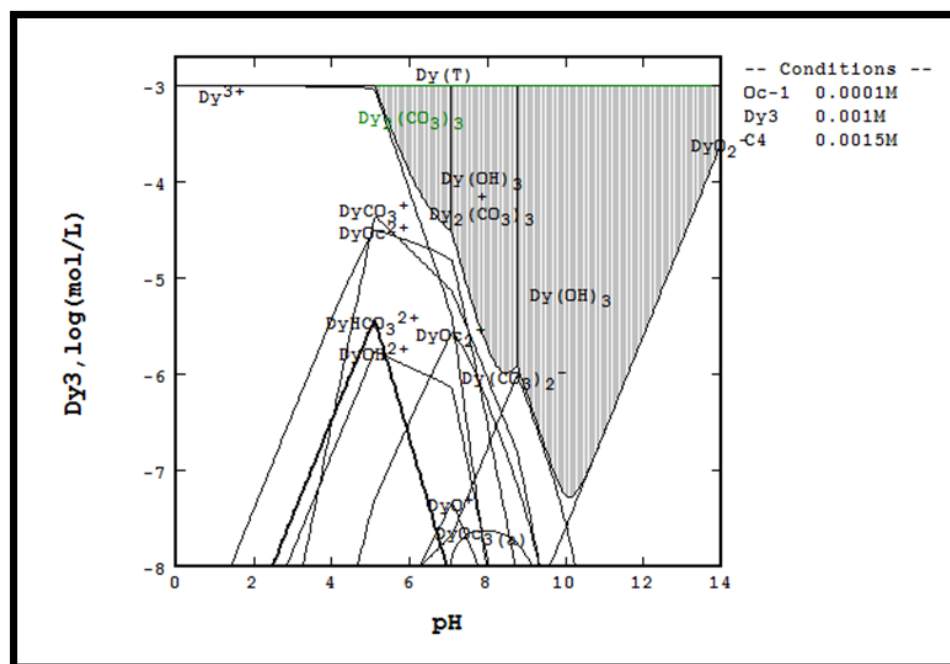
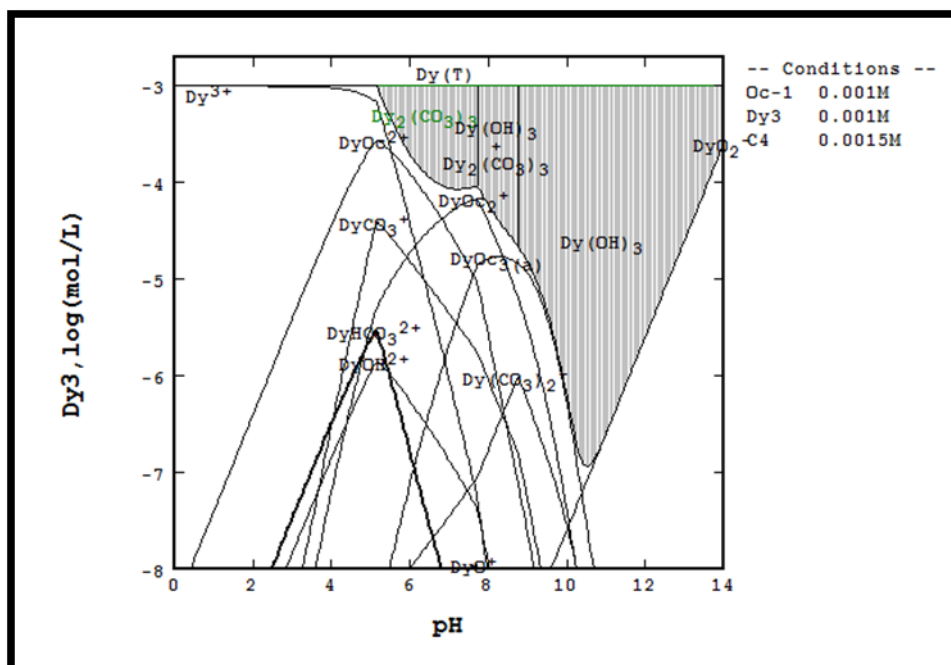**Figure 130: Speciation Diagram for the Dy Carbonate System with 1E-4M OHA**



**Figure 131: Speciation Diagram for the Dy Carbonate System with 0.001M OHA**
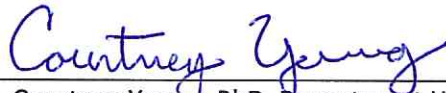
## APPENDIX E: StabCal Thermodynamic Data

| Species | ΔG (kcal) | logK, logβ₂, logβ₃ |
|---|---|---|
| H + A | 0 | -- |
| Ob - A | 0 | -- |
| Oc - A | 0 | -- |
| La 3+ A | -163.408 | -- |
| Ce 3+ A | -160.612 | -- |
| Pr 3+ A | -162.309 | -- |
| Nd 3+ A | -160.516 | -- |
| Eu 3+ A | -137.213 | -- |
| Tb 3+ A | -155.808 | -- |
| Tm 3+ A | -158.222 | -- |
| Y 3+ A | -165.822 | -- |
| HOb 0 A | -15.2315 | 10.95 |
| H2Ob + A | -26.2955 | 19.06 |
| LaOb 2+ A | -177.643 | 9.79 |
| LaOb2 + A | -190.275 | 18.62 |
| LaOb3 0 A | -201.537 | 26.66 |
| CeOb 2+ A | -175.324 | 10.14 |
| CeOb2 + A | -188.311 | 19.23 |
| CeOb3 0 A | -200.146 | 27.69 |
| PrOb 2+ A | -177.485 | 10.48 |
| PrOb2 + A | -191.032 | 19.98 |
| PrOb3 0 A | -203.671 | 29.03 |
| NdOb 2+ A | -176.333 | 10.95 |
| NdOb2 + A | -190.698 | 21.05 |
| NdOb3 0 A | -203.706 | 30.37 |
| EuOb 2+ A | -153.34 | 11.18 |
| EuOb2 + A | -167.968 | 21.47 |
| EuOb3 0 A | -181.467 | 31.15 |
| TbOb 2+ A | -172.362 | 11.49 |
| TbOb2 + A | -187.409 | 22.09 |
| TbOb3 0 A | -201.372 | 32.11 |
| DyOb 2+ A | -175.875 | 11.77 |
| DyOb2 + A | -191.345 | 22.68 |
| DyOb3 0 A | -205.758 | 33.03 |
| TmOb 2+ A | -175.472 | 12.00 |
| TmOb2 + A | -191.133 | 23.05 |
| TmOb3 0 A | -205.505 | 33.37 |

| | | |
|---|---|---|
| **YOb 2+ A** | -181.803 | 11.07 |
| **YOb2 + A** | -196.304 | 21.27 |
| **YOb3 0 A** | -209.490 | 30.72 |
| **HOc 0 A** | -13.049 | 9.35 |
| **LaOc 2+ A** | -171.326 | 5.16 |
| **LaOc2 + A** | -177.601 | 9.33 |
| **LaOc3 0 A** | -181.373 | 11.88 |
| **CeOc 2+ A** | -168.331 | 5.45 |
| **CeOc2 + A** | -175.433 | 9.79 |
| **CeOc3 0 A** | -179.819 | 12.79 |
| **PrOc 2+ A** | -170.732 | 5.53 |
| **PrOc2 + A** | -177.348 | 9.95 |
| **PrOc3 0 A** | -181.693 | 12.92 |
| **NdOc 2+ A** | -169.089 | 5.64 |
| **NdOc2 + A** | -175.855 | 10.17 |
| **NdOc3 0 A** | -180.364 | 13.26 |
| **EuOc 2+ A** | -146.264 | 5.99 |
| **EuOc2 + A** | -153.466 | 10.84 |
| **EuOc3 0 A** | -158.480 | 14.30 |
| **TbOc 2+ A** | -165.159 | 6.21 |
| **TbOc2 + A** | -172.675 | 11.29 |
| **TbOc3 0 A** | -178.016 | 14.99 |
| **DyOc 2+ A** | -168.713 | 6.52 |
| **DyOc2 + A** | -176.652 | 11.91 |
| **DyOc3 0 A** | -182.457 | 15.95 |
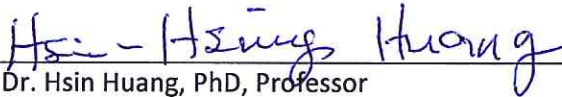
# SIGNATURE PAGE

This is to certify that the thesis prepared by Greer Elaine Galt entitled "Adsorption of Salicylhydroxamic Acid on Selected Rare Earth Oxides and Carbonates" has been examined and approved for acceptance by the Department of Metallurgical and Materials Engineering, Montana Tech of The University of Montana, on this 26th day of April, 2017.
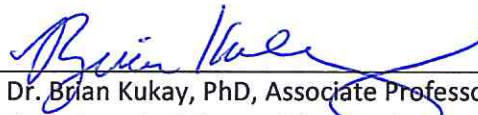
Dr. Courtney Young, PhD, Department Head and Professor
Department of Metallurgical and Materials Engineering
Chair, Examination Committee

Dr. Hsin Huang, PhD, Professor
Department of Metallurgical and Materials Engineering
Member, Examination Committee

Dr. Rod James, PhD, Professor
Department of Environmental Engineering
Member, Examination Committee

Dr. Brian Kukay, PhD, Associate Professor
Department of General Engineering
Member, Examination Committee